Second Harmonic Generation at Plasmonic Interfaces and Its Interactions with

Quantum Emitters Under Strong Coupling Conditions

by

Elena Drobnyh

A Dissertation Presented in Partial Fulfillment
of the Requirements for the Degree
Doctor of Philosophy

Approved November 2022 by the
Graduate Supervisory Committee:

Maxim Sukharev, Chair
Kevin Schmidt
Stephen Goodnick
Vladimiro Mujica

ARIZONA STATE UNIVERSITY

December 2022

ABSTRACT

In the developing field of nonlinear plasmonics, it is important to understand the nonlinear responses of the metallic nanostructures. In the present thesis, rigorous electrodynamical simulations based on the fully vectorial three-dimensional nonlinear hydrodynamic Drude model describing metal coupled to Maxwell's equations are performed to investigate linear and nonlinear responses of the plasmonic materials and their coupling with quantum emitters.

The first part of this thesis is devoted to analyzing properties of the localized surface plasmon resonances of metallic nanostructures and their nonlinear optical responses. The behavior of the second harmonic is investigated as a function of various physical parameters at different plasmonic interfaces, revealing highly complex dynamics. By collaborating with several research teams, simulations are proven to be in close agreement with experiments, both quantitative and qualitative.

The second part of the thesis explores the strong coupling regime and its influence on the second harmonic generation. Considering plasmonic systems of molecules and periodic nanohole arrays on equal footing in the nonlinear regime is done for the first time. The results obtained are supported by a simple analytical model.

DEDICATION

To the special ones who reignite my lust for life.

ACKNOWLEDGMENTS

TABLE OF CONTENTS

LIST OF TABLES

LIST OF FIGURES

Chapter 1

INTRODUCTION

1.1   Motivation

Plasmonics is a subfield of nanophotonics. It studies the interaction of light and matter through Surface Plasmon Resonances (SPRs), either localized or propagating. Those resonances correspond to collective oscillations of the conduction electrons in metal. Collectively oscillating free electrons result in highly localized electromagnetic energy build-up on a surface of the interface. The size of localization is comparable to or smaller than the wavelength of the excited optical pulse. It is a very powerful tool to study fundamental properties of light and its interaction with matter well below the diffraction limit (Martin-Moreno 2009).

Nanoscale structures are studied by nanoplasmonics. There are a lot of various fascinating applications as an optical data storage (Black et al. 2000; Mansuripur et al. 2009; Sato, Oike, and Hanashima 2009; Zou et al. 2012), biosensing and imaging (Alagiri, Rameshkumar, and Pandikumar 2017; Bengali and Giri 2018; Rodrigues et al. 2018; Jain et al. 2008; Lee and El-Sayed 2006), photoinduced and heat-assisted drug delivery (Medici et al. 2015; Jain, El-Sayed, and El-Sayed 2007; Zhang 2015; Tran et al. 2017).

Moreover, SPRs are very sensitive to tuning the shape, roughness of the edges, incident pulse, etc. bringing a great difference to the response (Sarychev and Shalaev 2007). That provides flexibility in the desired resonant frequency. The resulting resonance can range from the visible part of the spectrum to the deep infrared (Taliercio and Biagioni 2019).

The interaction between matter and light can result in strong coupling when the coupling strength becomes larger than at the highest energy damping rate. The emitted photon from the

matter excites optical modes in the environment, which in turn excites again the matter, initiating a coherent and reversible exchange of energy between the two systems (Törmä and Barnes 2015). When this is the case, it opens a wide range of optical phenomena to study. But the strong coupling regime remained a theoretical topic for a long time. It required cryogenic temperatures to have an energy exchange faster than any other relaxations or loss mechanisms in matter. Eventually it was experimentally observed (Goy et al. 1983; Kaluzny et al. 1983; Haroche and Kleppner 1989; Thompson, Rempe, and Kimble 1992; Rempe, Walther, and Klein 1987). But still, there are a lot of possibilities for the applications that are not investigated yet because of the complexity of the experimental setup.

The scope of this work is twofold:

1. To investigate properties of the Second Harmonic (SH) generation at various metal interfaces;
2. To study the strong coupling between quantum emitters and plasmons in the nonlinear regime.

In this thesis, optical properties of structures with experimentally realizable parameters are considered, both qualitative and quantitative comparisons of the numerical simulations and experimentally obtained results are presented, the sensitivity of the second harmonic generation to the shapes of the nanostructures, to the incident polarization is discussed, the interaction of the plasmonic interfaces with quantum emitters under strong coupling conditions is shown and supported by the analytical model. Also, a detailed overview of the theoretical aspects and numerical approaches is provided.

1.2 Optical Constants

The optical response of a material to the incident light is expressed as the complex refractive index N since some part of the light will be absorbed:

$$N = n + ik, \tag{1.1}$$

where n is the refractive index that indicates the phase velocity, k is the extinction or absorption coefficient that shows the amount of attenuation when the light propagates through the material.

Another form to describe this response is through the complex dielectric function ϵ:

$$\epsilon = \epsilon' + i\epsilon'', \tag{1.2}$$

where ϵ' is the real part of the permittivity and ϵ'' is the imaginary part of the permittivity that shows absorption losses if it is positive and gains if it is negative.

Equations (1.1) and (1.2) are totally equivalent. Recalling that $\epsilon = N^2$, one can obtain the relation between the real and imaginary parts of N and ϵ. In other words:

$$\epsilon' + i\epsilon'' = n^2 - k^2 + 2ink. \tag{1.3}$$

Equating the real and imaginary parts, one can obtain the following relationships:

$$\epsilon' = n^2 - k^2,$$
$$\epsilon'' = 2nk. \tag{1.4}$$

Expressing n and k through ϵ' and ϵ'', one can get these formulas (Bohren and Huffman 1983; Jackson 2012):

$$n = \sqrt{\frac{\sqrt{\epsilon'^2 + \epsilon''^2} + \epsilon'}{2}},$$
$$k = \sqrt{\frac{\sqrt{\epsilon'^2 + \epsilon''^2} - \epsilon'}{2}}. \tag{1.5}$$

The material is assumed to be not magnetic so that the permeability $\mu = \mu_0$. The dielectric constant can be determined by observing the optical power reflected and transmitted from the matter.

Different classes of materials have been explored for plasmonics applications, including ceramics, semiconductors, and metals, depending on the desired wavelength range of operation (Naik et al. 2014). The optical properties of metals are not the same as for the standard dielectrics. The presence of free conduction electrons results in large electrical conductivity. Especially noble metals such as Ag (silver) and Au (gold) have been extensively explored. Their real part ϵ' is negative (Palik 1998), which is the origin of their plasmon-related effects. That is why their localized SPRs and surface plasmon-polariton waveguiding properties throughout the visible range are still of great interest in plasmonics (Maier 2007).

1.3   Theory of Plasmonic Materials

Looking into the original definition of the term 'plasmon', one can find (Pines 1956):

> The valence electron collective oscillations resemble closely the electronic plasma oscillations observed in gaseous discharges. We introduce the term 'plasmon' to describe the quantum of elementary excitation associated with this high-frequency collective motion.

Thus, a plasmon is a quantum quasi-particle representing the elementary excitations, or modes, of the charge density oscillations in a plasma. From an electromagnetic point of view, metals are plasmas, comprising fixed, positive ion cores and mobile conduction electrons. It was predicted (Ritchie 1957) that bulk plasmas can sustain longitudinal plasma oscillations – plasmons, oscillations whose resonant frequency arises from the restoring force that the altered charge distribution exerts on the mobile charges when they are displaced from equilibrium (Powell and Swan 1959; Yamamoto, Araya, and García de Abajo 2001). For a bulk plasma, this plasmon frequency,

ω_p, is given by (Kittel 1956):

$$\omega_p^2 = \frac{ne^2}{\epsilon_0 m},\tag{1.6}$$

where n is the number density of mobile charge carriers, e is their charge, m is their mass, and ϵ_0 is the relative permittivity of free space.

Electromagnetic radiation (light) incident on the plasma at a frequency below the plasma frequency induces motion in the charge carriers that acts to screen out the incident field – incident waves are reflected; above the plasma frequency the charges are unable to respond quickly enough to screen out the incident field and the waves are instead transmitted.

To include dissipation, one can introduce a damping term in addition to the plasma frequency. This results in the Drude model, where the frequency-dependent relative permittivity of the metal, $\epsilon_m(\omega)$, is given by (Kreibig and Vollmer 1995):

$$\epsilon_m(\omega) = 1 - \frac{\omega_p}{\omega^2 + i\gamma\omega},\tag{1.7}$$

where γ is the relaxation frequency associated with the metal (it is the inverse of the characteristic time interval between scattering events that dampen the motion of the conduction electrons).

Surface Plasmon-Polaritons (SPPs) are oscillations of charge on a metal-dielectric boundary that are able to produce intense, highly localized evanescent fields. A quantum of surface charge oscillation (a plasmon) couples to a quantum of light (a photon), leading to a system that is a hybrid of the two independent entities.

SPPs allow going beyond the diffraction limit because as can be seen from the dispersion curve, the wavelength corresponding to the SPP can be made much smaller than that of light for a given frequency of excitation (Barnes, Dereux, and Ebbesen 2003).

Chapter 2

THEORETICAL BACKGROUND

The interaction between light and matter is very complicated. In order to be able to simulate it numerically, one should understand the theoretical aspects of this phenomenon. The following chapter covers the needed background that is considered later in the numerical simulations.

2.1 Electromagnetic Radiation: Maxwell's Equations

The electromagnetic radiation is described classically in accordance with Maxwell's equations (Griffiths 2017):

$$
\begin{aligned}
\nabla \cdot \mathbf{E} &= \frac{\rho}{\epsilon_0}, \\
\nabla \cdot \mathbf{B} &= 0, \\
\mu_0 \frac{\partial \mathbf{H}}{\partial t} &= -\nabla \times \mathbf{E}, \\
\epsilon_0 \frac{\partial \mathbf{E}}{\partial t} &= \nabla \times \mathbf{H} - \mathbf{J},
\end{aligned}
\tag{2.1}
$$

where ρ and $\mathbf{J}$ are the total charge and current densities, respectively, ϵ_0 and μ_0 are the permittivity and permeability of free space. $\mathbf{J} = \frac{\partial \mathbf{P}}{\partial t}$ is the current density in spatial regions occupied by metal.

The fundamental law of conservation of charge (the net charge of an isolated system will always remain constant) could be derived from (2.1). The corresponding equation is called 'continuity equation':

$$
\frac{\partial \rho}{\partial t} + \nabla \cdot \mathbf{J} = 0.
\tag{2.2}
$$

This equation implies that the change in some particular volume will be equal to the amount coming into this volume minus outgoing flux of charge.

It is also useful to introduce the definition of dipole moment and polarization since Section 4.1 highly relies on them. An electric dipole moment represents the separation of the positive and negative charges in the media. To characterize dipoles, electric dipole moment is used. It is a vector quantity that points from the negative charge towards the positive one. In a toy model, there are two point charges with the same value q of the charge but with different signs. Those charges are separated by a distance d. Then the electric dipole moment can be calculated as:

$$p = qd. \tag{2.3}$$

Under an external electric field, applied to a media, the internal charges obtain electric dipole moments. Their presence leads to a macroscopic polarization density $\mathbf{P}$ (dipole moment per unit volume). Together they are connected by the following equation:

$$\rho_b = -\nabla \cdot \mathbf{P}, \tag{2.4}$$

where ρ_b is the bound charges.

In the present thesis, both linear and nonlinear polarizations will be under the scope. If the media is homogeneous and isotropic, the polarization is aligned with and proportional to the electric field $\mathbf{E}$:

$$\mathbf{P} = \chi \epsilon_0 \mathbf{E}, \tag{2.5}$$

where χ is the electric susceptibility of the media.

Going into a more complicated case, where the media is no longer isotropic, χ becomes a tensor χ_{ij} and the expression for polarization is:

$$P_i = \sum_j \epsilon_0 \chi_{ij} E_j. \tag{2.6}$$

So one can see that polarization is no longer linearly proportional to the electric field $\mathbf{E}$. For a better understanding of equation (2.6), it is broken down using a Taylor series:

$$\frac{P_i}{\epsilon_0} = \sum_j \chi_{ij}^{(1)} E_j + \sum_{jk} \chi_{ijk}^{(2)} E_j E_k + \sum_{jkl} \chi_{ijkl}^{(3)} E_j E_k E_l + \dots, \tag{2.7}$$

where $\chi^{(1)}$ is the linear susceptibility, $\chi^{(2)}$ is the second-order susceptibility, and $\chi^{(3)}$ is the third-order susceptibility.

2.2   Metal: Drude Model

Once a strong platform is established for how to characterize radiation around, the next question that should be addressed is how to describe the interactions inside the medium. The Drude model can be used. There, it is assumed that metal is an electron gas, with electrons moving in straight lines until they collide with each other, or with the positive background particles that must be there to compensate for charge neutrality. Here is the list of basic assumptions:

- Electron-electron interaction between collisions is ignored;
- Electron-ion interaction is also neglected;
- Collisions happen instantaneously and mostly with ions;
- Electrons move along a straight line between the collisions;
- Electrons achieve thermal equilibrium with their environment only through collisions.

To derive the Drude dielectric function, the equation of motion for the momentum **p** per electron can be used:

$$\frac{d\mathbf{p}}{dt} = -\frac{\mathbf{p}}{\tau} - e\mathbf{E}, \tag{2.8}$$

where τ is the relaxation time.

The equation for the current density is:

$$\mathbf{J} = -ne\mathbf{v} = -\frac{ne\mathbf{p}}{m_e}, \tag{2.9}$$

where m_e is the electron mass, n is the electron density, and **v** is the electron velocity.

Combining (2.8) with (2.9) and assuming that there is a steady-state solution of the form $\mathbf{p}(t) = Re\left[\mathbf{p}(\omega)exp(-i\omega t)\right]$, one can get:

$$\mathbf{J}(\omega) = \frac{ne^2}{m_e(1/\tau - i\omega)}\mathbf{E}(\omega). \tag{2.10}$$

Recalling Ohm's law:

$$\mathbf{J}(\omega) = \sigma(\omega)\mathbf{E}(\omega), \tag{2.11}$$

where Drude conductivity is:

$$\sigma(\omega) = \frac{ne^2\tau}{m_e(1 - i\omega\tau)}. \tag{2.12}$$

Introducing the current density into Maxwell's equations, the wave equation is:

$$\nabla^2\mathbf{E}(\mathbf{r}) + \frac{\omega^2}{c^2}\epsilon(\omega)\mu\mathbf{E}(\mathbf{r}) = 0, \tag{2.13}$$

where $\epsilon(\omega)$ is:

$$\epsilon(\omega) = 1 + \frac{i\sigma(\omega)}{\epsilon_0\omega}. \tag{2.14}$$

Combining this equation of $\epsilon(\omega)$ with Drude conductivity, one can obtain the following result:

$$\epsilon(\omega) = 1 - \frac{\omega_p^2}{\omega(\omega + i\gamma)}, \tag{2.15}$$

where $\gamma = \frac{1}{\tau}$ is the Drude damping rate, $\omega_p = \sqrt{\frac{e^2 n}{m_e\epsilon_0}}$ is the plasma frequency. This dielectric expression only considers free electrons. If the response of both bound and free electrons in a metal is combined in one dielectric dependence, one can get the following:

$$\epsilon(\omega) = \epsilon_\infty(\omega) - \frac{\omega_p^2}{\omega(\omega + i\gamma)}, \tag{2.16}$$

where $\epsilon_\infty(\omega)$ is the contribution of the bound electrons.

2.3 Metal: Drude-Lorentz Model

One simple way to introduce the Drude model is by using the Lorentz model for the atomic polarizability (Jackson 2012; Dressel, Gruner, and Grüner 2002). It treats the interaction of an electromagnetic wave with a specific electronic state as a classical harmonic oscillator. The equation of motion for the coordinate $\mathbf{r}$ representing a small perturbation of the electrons from the ground state in an external electric field $\mathbf{E}$ is (Landau and Lifshitz 1982):

$$m\left(\frac{d^2\mathbf{r}}{dt^2} + \omega_0^2\mathbf{r} + \gamma\frac{d\mathbf{r}}{dt}\right) = -e\mathbf{E}, \tag{2.17}$$

where γ is the dissipation coefficient and ω_0 is the resonance frequency.

Equation (2.17) is similar to a classical forced harmonic oscillator with damping. This can be solved easily using complex notations for harmonic fields. In a first approximation, it can be assumed that the conduction electrons in a metal are not bound and can be described by the Lorentz model without restoring force. Since the free electrons are distributed uniformly in the metal, their contributions to the total optical susceptibility are the sum of their individual polarizabilities, without any local field correction:

$$-\omega^2\mathbf{r} = -\omega_0^2\mathbf{r} + i\gamma\omega\mathbf{r} + \frac{e\mathbf{E}}{m}. \tag{2.18}$$

Assuming that the displacement is along x-axis, it can be solved as:

$$x = \frac{e}{m}\frac{1}{\omega_0^2 - \omega^2 - i\omega\gamma}E_0. \tag{2.19}$$

Using the dipole moment definition as $p = ex$, the polarization density becomes:

$$P = nex = \frac{ne^2}{m}\frac{1}{\omega_0^2 - \omega^2 - i\omega\gamma}E_0, \tag{2.20}$$

where n is the density of oscillators.

So the Drude-Lorentz permittivity can be obtained as:

$$\epsilon(\omega) = 1 + \frac{ne^2}{\epsilon_0 m} \frac{1}{\omega_0^2 - \omega^2 - i\omega\gamma} \tag{2.21}$$

And the plasma frequency ω_p is defined as:

$$\omega_p = \sqrt{\frac{ne^2}{m\epsilon_0}}. \tag{2.22}$$

A factor ϵ_∞ can substitute the constant in (2.21) to account for other contributions. The damping term, γ, corresponds to the collision rate of free electrons with the crystal or impurities. It is usually small compared to ω in the regions of interest. The optical response of the positive ions in the crystal has so far been ignored. In a first approximation (which is at least correct at long wavelengths), this contributes to a constant background real dielectric function $\epsilon_\infty \geq 1$. It affects the optical response of the crystal and the dynamics of the free electrons.

To describe real and imaginary parts of the dielectric function better, one can adopt another model: the Drude function with the more general Lorentz function (Rakić et al. 1998):

$$\epsilon(\omega) = \epsilon_{r,\infty} - \frac{\omega_p^2}{\omega^2 - i\gamma_0\omega} - \sum_{n=1}^{N} \frac{\Delta\epsilon_{r,n}\omega_n^2}{\omega^2 - i\gamma_n\omega - \omega_n^2}, \tag{2.23}$$

where the third term is the sum over contributions arising from the nth Lorentz oscillator. It can include interband transitions and motions of the ionic cores.

2.4   Metal: Hydrodynamic Drude Model

The hydrodynamic model extends the Drude description by introducing some kind of interactions in the electron gas. To describe this motion, the Euler equation is used:

$$\frac{\partial \mathbf{v}}{\partial t} + (\mathbf{v} \cdot \nabla)\mathbf{v} + \gamma\mathbf{v} = -\frac{e}{m_e}(\mathbf{E} + \mathbf{v} \times \mathbf{B}) - \frac{\nabla p}{nm_e}, \tag{2.24}$$

where n is the electron density, $\mathbf{v}$ is their velocity, and p is the electron gas pressure. Defining the current density as $\mathbf{J} = ne\mathbf{v}$, the equation of motion for free electrons (2.24) becomes:

$$\dot{\mathbf{J}} - \frac{\dot{n}}{n}\mathbf{J} + (\mathbf{J} \cdot \nabla)\frac{\mathbf{J}}{n} + \gamma\mathbf{J} = \frac{ne^2}{m_e}\mathbf{E} + \frac{e}{m_e}\mathbf{J} \times \mathbf{B} - \frac{e\nabla p}{m_e}. \tag{2.25}$$

For free electrons, the continuity equation is:

$$\frac{\partial n}{\partial t} + \nabla \cdot (n\mathbf{v}) = 0. \tag{2.26}$$

Substituting the current density there, it becomes:

$$\frac{\partial n}{\partial t} + \frac{1}{e}\nabla \cdot \mathbf{J} = 0. \tag{2.27}$$

Integration by time gives:

$$n = n_0 - \frac{1}{e}\nabla \cdot \int \mathbf{J}dt, \tag{2.28}$$

where n_0 is the background equilibrium charge density in the absence of any applied field. Introducing macroscopic polarization density as $\dot{\mathbf{P}} = \mathbf{J}$, equation (2.28) becomes:

$$n = n_0 - \frac{1}{e}\nabla \cdot \mathbf{P}. \tag{2.29}$$

Assuming $\dot{n} \ll n$, the ratio $\frac{\dot{n}}{n}$ may be expanded in powers of $\frac{1}{n_0 e}$:

$$\frac{\dot{n}}{n} = -\frac{1}{n_0 e}\nabla \cdot \dot{\mathbf{P}}\left(1 - \frac{1}{n_0 e}\nabla \cdot \mathbf{P}\right)^{-1} = -\frac{\nabla \cdot \dot{\mathbf{P}}}{en_0} - \frac{1}{n_0^2 e^2}\left(\nabla \cdot \dot{\mathbf{P}}\right)\left(\nabla \cdot \mathbf{P}\right) + \mathcal{O}\left(\frac{1}{n_0^3 e^3}\right). \tag{2.30}$$

Substituting equation (2.30) into (2.25) and neglecting quadratic and higher order terms, one can get (Scalora et al. 2010):

$$\ddot{\mathbf{P}} + \gamma\dot{\mathbf{P}} = \frac{n_0 e^2}{m_e}\mathbf{E} - \frac{e}{m_e}\mathbf{E}\left(\nabla \cdot \mathbf{P}\right) + \frac{e}{m_e}\dot{\mathbf{P}} \times \mathbf{B} - \frac{1}{n_0 e}\left[\left(\nabla \cdot \dot{\mathbf{P}}\right)\dot{\mathbf{P}} + \left(\dot{\mathbf{P}} \cdot \nabla\right)\dot{\mathbf{P}}\right] - \frac{e\nabla p}{m_e}. \tag{2.31}$$

The specific impact of pressure is seldom considered in the dynamics (Sipe et al. 1980; Agranovich 2012). But in order to archive a higher precision of the numerical calculations, the pressure term should be considered. Pressure might be defined as $p = nk_B T$, where k_B is the Boltzmann constant and T is the temperature.

Using the continuity equation (2.30), one can obtain:

$$-\frac{e\nabla p}{m_e} = -\frac{e}{m_e}k_B T \nabla\left(n_0 - \frac{1}{e}\nabla\cdot\mathbf{P}\right) = \frac{k_B T}{m_e}\nabla\left(\nabla\cdot\mathbf{P}\right). \tag{2.32}$$

The quantum pressure is usually described as:

$$p = p_0\left(\frac{n}{n_0}\right)^{\gamma_p}, \tag{2.33}$$

where $\gamma_p = \frac{D+2}{D}$ and D is the dimensionality of the problem.

2.4.1 Two Dimensional Case

Here $D = 2$ and $\gamma_p = 2$. The quantum pressure becomes:

$$p = \frac{p_0 n^2}{n_0^2} \tag{2.34}$$

and its gradient is:

$$\nabla p = \frac{p_0}{n_0^2} 2n\nabla n. \tag{2.35}$$

The pressure terms could be transformed as:

$$-\frac{e\nabla p}{m} = -\frac{2ep_0}{m_e n_0^2}n\nabla n = -\frac{ep_0}{m_e n_0^2}\nabla\left(n^2\right) = -\frac{ep_0}{m_e n_0^2}\nabla\left(n_0 - \frac{\nabla\cdot\mathbf{P}}{e}\right)^2 =$$

$$-\frac{ep_0}{m_e}\nabla\left(1 - 2\frac{\nabla\cdot\mathbf{P}}{en_0} + 2\cdot 1\cdot\frac{1}{2!}\left(\frac{\nabla\cdot\mathbf{P}}{en_0}\right)^2 + ...\right) \simeq$$

$$-\frac{ep_0}{m_e}\left(-\frac{2}{en_0}\nabla\left(\nabla\cdot\mathbf{P}\right) + \frac{1}{(en_0)^2}2\left(\nabla\cdot\mathbf{P}\right)\nabla\left(\nabla\cdot\mathbf{P}\right)\right) = \tag{2.36}$$

$$\frac{2E_F}{m_e}\nabla\left(\nabla\cdot\mathbf{P}\right) - \frac{2E_F}{m_e n_0 e}\left(\nabla\cdot\mathbf{P}\right)\nabla\left(\nabla\cdot\mathbf{P}\right).$$

2.4.2 Three Dimensional Case

Here $D = 3$ and $\gamma_p = 5/3$. The quantum pressure equals:

$$p = p_0\left(\frac{n}{n_0}\right)^{5/3} \tag{2.37}$$

and its gradient is:

$$\nabla p = \frac{5}{3} \frac{p_0}{n_0^{5/3}} n^{2/3} \nabla n. \tag{2.38}$$

Substituting everything into the pressure term, one can obtain:

$$-\frac{e\nabla p}{m} = -\frac{e}{m_e} \frac{5}{3} \frac{p_0 n^{2/3}}{n_0^{5/3}} \nabla n = -\frac{e}{m_e} \frac{5}{3} \left(\frac{n}{n_0}\right)^{2/3} E_F \nabla n = -\frac{e}{m_e} \frac{5}{3} n_0^{-2/3} E_F \left(n^{2/3} \nabla n\right) =$$

$$-\frac{e}{m_e} n_0^{-2/3} E_F \left(\nabla n^{5/3}\right) = -\frac{e}{m_e} n_0^{-2/3} E_F \nabla \left(n_0 - \frac{\nabla \cdot \mathbf{P}}{e}\right)^{5/3} = -\frac{e}{m_e} n_0 E_F \nabla \left(1 - \frac{\nabla \cdot \mathbf{P}}{en_0}\right)^{5/3} =$$

$$-\frac{e}{m_e} n_0 E_F \nabla \left[1 + \frac{5}{3}\left(-\frac{\nabla \cdot \mathbf{P}}{en_0}\right) + \frac{5}{3}\frac{2}{3}\frac{1}{2!}\left(-\frac{\nabla \cdot \mathbf{P}}{en_0}\right)^2 + \frac{5}{3}\frac{2}{3}\left(-\frac{1}{3}\right)\frac{1}{3!}\left(-\frac{\nabla \cdot \mathbf{P}}{en_0}\right)^3 + \right.$$

$$\left. \mathcal{O}\left(\left(-\frac{\nabla \cdot \mathbf{P}}{en_0}\right)^4\right)\right] = -\frac{e}{m_e} n_0 E_F \left[-\frac{5}{3}\frac{1}{en_0}\nabla\left(\nabla \cdot \mathbf{P}\right) + \frac{5}{9}\frac{1}{(en_0)^2}2\left(\nabla \cdot \mathbf{P}\right)\nabla\left(\nabla \cdot \mathbf{P}\right) + \right. \tag{2.39}$$

$$\left. \frac{5}{81}3\left(\nabla \cdot \mathbf{P}\right)^2\nabla\left(\nabla \cdot \mathbf{P}\right)\frac{1}{(en_0)^3} + \mathcal{O}\left(\left(-\frac{\nabla \cdot \mathbf{P}}{en_0}\right)^4\right)\right] = \frac{5}{3}\frac{E_F}{m_e}\nabla(\nabla \cdot \mathbf{P}) -$$

$$\frac{10}{9}\frac{E_F}{m_e}\frac{1}{n_0 e}(\nabla \cdot \mathbf{P})\nabla(\nabla \cdot \mathbf{P}) - \frac{5}{27}\frac{E_F}{m_e}\frac{1}{(n_0 e)^2}(\nabla \cdot \mathbf{P})^2\nabla(\nabla \cdot \mathbf{P}) - \mathcal{O}\left(\left(-\frac{\nabla \cdot \mathbf{P}}{en_0}\right)^4\right).$$

Retaining all the terms up to the third-order (Minh Ngo et al. 2022), equation (2.31) becomes:

$$\ddot{\mathbf{P}} + \gamma\dot{\mathbf{P}} = \frac{n_0 e^2}{m_e}\mathbf{E} - \frac{e}{m_e}\mathbf{E}\left(\nabla \cdot \mathbf{P}\right) + \frac{e}{m_e}\dot{\mathbf{P}} \times \mathbf{B} - \frac{1}{n_0 e}\left[\left(\nabla\dot{\mathbf{P}}\right)\dot{\mathbf{P}} + \left(\dot{\mathbf{P}}\nabla\right)\dot{\mathbf{P}}\right] -$$

$$\frac{5}{3}\frac{E_F}{m_e}\nabla\left(\nabla \cdot \mathbf{P}\right) - \frac{10}{9}\frac{E_F}{m_e}\frac{1}{n_0 e}\left(\nabla \cdot \mathbf{P}\right)\nabla\left(\nabla \cdot \mathbf{P}\right) - \frac{5}{27}\frac{E_F}{m_e}\frac{1}{(n_0 e)^2}\left(\nabla \cdot \mathbf{P}\right)^2\nabla\left(\nabla \cdot \mathbf{P}\right) \tag{2.40}$$

The quantum model intrinsically contains a first-order classical ideal electron gas contribution and nonlinear quantum corrections. It is easy to see the impact of pressure if the equations are scaled in response to dimensionless time and longitudinal and transverse coordinates:

$$\tau = \frac{ct}{\lambda_0},$$
$$\xi = \frac{z}{\lambda_0}, \tag{2.41}$$
$$\tilde{y} = \frac{y}{\lambda_0},$$

where $\lambda_0 = 1\ \mu$m is arbitrarily chosen as the reference wavelength.

As a result of this scaling, the following equation is obtained:

$$\ddot{\mathbf{P}} + \widetilde{\gamma}\dot{\mathbf{P}} = \frac{n_0 e}{m_e} \frac{\lambda_0^2}{c^2} \mathbf{E} - \frac{e}{m_e} \frac{\lambda_0}{c^2} \mathbf{E} \left(\nabla \cdot \mathbf{P}\right) + \frac{e}{m_e} \frac{\lambda_0}{c} \dot{\mathbf{P}} \times \mathbf{B} -$$

$$\frac{1}{n_0 e} \frac{1}{\lambda_0} \left[\left(\nabla \cdot \dot{\mathbf{P}}\right) \dot{\mathbf{P}} + \dot{\mathbf{P}} \left(\nabla \cdot \dot{\mathbf{P}}\right)\right] + \frac{5}{3} \frac{E_F}{m_e} \frac{1}{c^2} \nabla \left(\nabla \cdot \mathbf{P}\right) - \qquad (2.42)$$

$$\frac{10}{9} \frac{E_F}{m_e} \frac{1}{n_0 e} \frac{1}{c^2 \lambda_0} \left(\nabla \cdot \mathbf{P}\right) \nabla \left(\nabla \cdot \mathbf{P}\right) - \frac{5}{27} \frac{E_F}{m_e} \frac{1}{n_0^2 e^2} \frac{1}{c^2 \lambda_0^2} \left(\nabla \cdot \mathbf{P}\right)^2 \nabla \left(\nabla \cdot \mathbf{P}\right),$$

where $\widetilde{\gamma} = \frac{\lambda_0}{c}\gamma$.

Equation (2.42) shows explicitly the impact of each phenomenon, such as:

- $\frac{e}{m_e} \frac{\lambda_0}{c} \dot{\mathbf{P}} \times \mathbf{B}$ represents the magnetic Lorentz force;
- $-\frac{e}{m_e} \frac{\lambda_0}{c^2} \mathbf{E} \left(\nabla \cdot \mathbf{P}\right)$ is the quadrupole-like Columb term;
- $-\frac{1}{n_0 e \lambda_0} \left[\left(\nabla \cdot \dot{\mathbf{P}}\right) \dot{\mathbf{P}} + \dot{\mathbf{P}} \left(\nabla \cdot \dot{\mathbf{P}}\right)\right]$ indicates the convective term;
- $\frac{5}{3} \frac{E_F}{m_e c^2} \left(\nabla \left(\nabla \cdot \mathbf{P}\right) - \frac{2}{3} \frac{1}{n_0 e \lambda_0} \left(\nabla \cdot \mathbf{P}\right) \nabla \left(\nabla \cdot \mathbf{P}\right) - \frac{1}{9} \frac{1}{n_0^2 e^2 \lambda_0^2} \left(\nabla \cdot \mathbf{P}\right)^2 \nabla \left(\nabla \cdot \mathbf{P}\right)\right)$ is electron pressure.

If all the nonlinear terms are neglected, (2.42) becomes:

$$\ddot{\mathbf{P}} + \widetilde{\gamma}\dot{\mathbf{P}} = \frac{n_0 e}{m_e} \left(\frac{\lambda_0}{c}\right)^2 \mathbf{E} + \left(\frac{\lambda_0}{c}\right)^2 \frac{5}{3} \frac{E_F}{m_e} \left(\frac{1}{\lambda_0}\right)^2 \nabla \left(\nabla \cdot \mathbf{P}\right). \qquad (2.43)$$

Even in the linear case, there is still a pressure term. It could directly impact the linear dielectric function of the metal near its walls if the fields are strong enough (i.e., on sharp edges, corners, etc.).

2.5 Molecular System: Rate Equations

Another system that should be considered before going into simulations details is molecular emitters. They can be described as a collection of quantum mechanical entities (in a mean-field approximation). To describe this system, one can start with the Hamiltonian (Sukharev and

Nitzan 2017):

$$\widehat{H} = \widehat{H}_M + \widehat{H}_R + \widehat{H}_{MR}, \tag{2.44}$$

where $\widehat{H}_M = \sum_m \hat{h}_m$ is a sum of molecular part, $\widehat{H}_R$ is the radiation part, and $\widehat{H}_{MR} = \sum_m \hat{h}_{mR}$ represents their interaction.

The molecular density matrix is denoted according to the Liouville equation:

$$\frac{d\hat{\rho}}{dt} = -\frac{i}{\hbar} \left[\widehat{H}, \hat{\rho} \right]. \tag{2.45}$$

Assuming $\hat{\rho} = \prod_m \hat{\rho}_m$ with $Tr_m \hat{\rho}_m = 1$ and $\widehat{H}_{mR} = -\mathbf{E}(\mathbf{r_m}) \cdot \hat{\mu}_m$, one can take a trace over all molecules except m^{th}:

$$\frac{d\rho_m}{dt} = -\frac{i}{\hbar} \left[\hat{h}_m - \langle \mathbf{E}(\mathbf{r}_m) \rangle \cdot \hat{\mu}_m, \hat{\rho}_m \right], \tag{2.46}$$

where $\langle \mathbf{E}(\mathbf{r}_m) \rangle = Tr' \left(\mathbf{E} \prod_{m' \neq m} \hat{\rho}_{m'} \right)$. Tr' represents trace over the states of all molecules except m^{th}. Equation (2.46) represents the dynamics of a single molecular dipole under the influence of the local average electric field at the position of this dipole. The latter includes the incident field and the average field of all other molecules. For a single molecule within an ensemble of two-level molecules, equation (2.46) yields:

$$
\begin{aligned}
\frac{d\rho_{11}}{dt} &= -i\frac{\mathbf{E}\mu_{12}}{\hbar} \left(\rho_{12} - \rho_{12}^* \right), \\
\frac{d\rho_{12}}{dt} &= -i\left[\frac{\mathbf{E}\mu_{12}}{\hbar} (\rho_{22} - \rho_{11}) + \Omega_{12}\rho_{12} \right], \\
\frac{d\rho_{22}}{dt} &= -i\frac{\mathbf{E}\mu_{12}}{\hbar} (\rho_{12} - \rho_{12}^*),
\end{aligned}
\tag{2.47}
$$

where indices 1 and 2 denote the ground and the excited state, respectively, μ_{12} is the corresponding transition dipole moment (assumed real), and $\Omega_{12} = (\epsilon_2 - \epsilon_1)/\hbar$ is the transition frequency.

Defining $X = \rho_{12} + \rho_{12}^*$, $Y = \rho_{12} - \rho_{12}^*$ and noting that $dX/dt = i\Omega_{12}Y$, equation (2.47)

changes to:

$$\frac{d\rho_{11}}{dt} = -\frac{1}{\Omega_{12}}\frac{dX}{dt}\frac{\mathbf{E}\mu_{12}}{\hbar},$$

$$\frac{d\rho_{22}}{dt} = \frac{1}{\Omega_{12}}\frac{dX}{dt}\frac{\mathbf{E}\mu_{12}}{\hbar}, \tag{2.48}$$

$$\frac{d^2X}{dt^2} = -\Omega_{12}^2 + 2\Omega_{12}\frac{\mathbf{E}\mu_{12}}{\hbar}\left(\rho_{11} - \rho_{22}\right).$$

The densities of molecules in state 1 and 2 can be denoted as $n_1 = n_M\rho_{11}$, $n_2 = n_M\rho_{22}$, where $n_1 + n_2 = n_M$. Then polarization is defined as $\mathbf{P} = Xn_M\mu_{12}$. After multiplying (2.48) by the molecular density n_M and only the last equation also by μ_{12}, assuming an isotropic system, and averaging over all orientations of the molecular dipole to get $\langle\mu_x\mu_y\rangle = \langle\mu_x\mu_z\rangle = \langle\mu_y\mu_z\rangle = 0$ and $\langle\mu_j^2\rangle = (1/3)\mu^2$ for $j = x, y, z$, one can get:

$$\frac{dn_1}{dt} = -\frac{1}{\hbar\Omega_{12}}\mathbf{E}\cdot\frac{d\mathbf{P}}{dt},$$

$$\frac{dn_2}{dt} = \frac{1}{\hbar\Omega_{12}}\mathbf{E}\cdot\frac{d\mathbf{P}}{dt}, \tag{2.49}$$

$$\frac{d^2\mathbf{P}}{dt^2} = -\Omega_{12}^2\mathbf{P} + \frac{2}{3\hbar}\Omega_{12}\mu_{12}^2\mathbf{E}(n_1 - n_2).$$

This form of the Liouville–von Neumann equations, written in terms of macroscopic polarization, is identical in the absence of relaxation processes to the kinetic equations. Sometimes it is referred to as rate equations. To account for population relaxation and dephasing, one typically introduces phenomenological decay constants (Tempel and Aspuru-Guzik 2011). Here, however, different practices have been used. For the two-level molecular model under discussion, the standard scheme uses Bloch-type equations, such as (Sukharev and Nitzan 2017):

$$\frac{d\rho_{11}}{dt} = -i\frac{\mathbf{E}\mu_{12}}{\hbar}(\rho_{12} - \rho_{12}^*) + \gamma_{21}\rho_{22},$$

$$\frac{d\rho_{12}}{dt} = -i\left[\frac{\mathbf{E}\mu_{12}}{\hbar}(\rho_{22} - \rho_{11}) + \Omega_{12}\rho_{12}\right] - \frac{\Gamma}{2}\rho_{12}, \tag{2.50}$$

$$\frac{d\rho_{22}}{dt} = -i\frac{\mathbf{E}\mu_{12}}{\hbar}(\rho_{12} - \rho_{12}^*) - \gamma_{21}\rho_{22},$$

where γ_{21} is the population relaxation rate. The coherence ρ_{12} decays with the rate $\frac{\Gamma}{2} = \frac{\gamma_{21}}{2} + \gamma_d$, which takes into account pure dephasing rate γ_d. These rates are related to the population

relaxation time T_1, decoherence time T_2, and the pure dephasing time T_2^*:

$$\frac{1}{T_2} = \frac{1}{2T_1} + \frac{1}{T_2^*}. \tag{2.51}$$

2.6 Interaction: Strong Coupling

Usually, the environment and matter interact through the spontaneous radiation. But the emission frequency doesn't change. If the interaction is strong enough, it brings changes in the resulting behavior. The energy levels of the emission change. They become inextricably linked with the levels of the environment. This case is called 'strong coupling'.
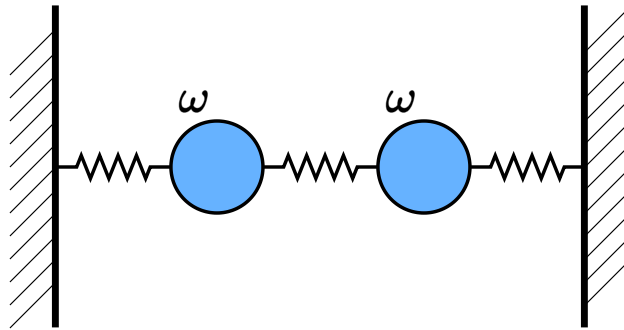
Figure 1. Two Coupled Oscillators

The paradigm model of coupling is two harmonic oscillators (see Fig. 1). The dynamics of the system is influenced by the original frequencies of the oscillators and by the exchange process. Thus, the energy levels of the system are modified. The difference between the original frequencies and the modified ones depends on the strength of the coupling.

There are two possible regimes (Hümmer et al. 2013):

- Weak coupling – the coupling is very small, so the modifications of the original frequencies are negligible;
- Strong coupling – the coupling is large, so the modifications become noticeable enough, and the energy spectrum of emission changes.

There are two coupled harmonic oscillators in Fig. 1. It is assumed that the resonant frequencies of the oscillators are the same and equal to ω. The dynamics of the system can be described as (Novotny 2010):

$$\frac{d^2 x_1}{dt^2} = \omega^2 x_1 + \Omega^2 (x_1 - x_2) = 0,$$
$$\frac{d^2 x_2}{dt^2} = \omega^2 x_2 + \Omega^2 (x_2 - x_1) = 0. \tag{2.52}$$

Here Ω characterizes the strength of the coupling between the two oscillators. Equations (2.52) can be solved in a general form as:

$$x_1(t) = A \sin(\omega_+ t + C) + B\sin(\omega_- t + D),$$
$$x_2(t) = -A\sin(\omega_+ t + C) + B\sin(\omega_- t + D), \tag{2.53}$$

where A, B, C, and D are the constants that could be found from the initial conditions. ω_+ and ω_- are the normal modes of the coupled oscillator system:

$$\omega_+^2 = \omega_c^2 + \Omega^2,$$
$$\omega_-^2 = \omega_c^2 - \Omega^2, \tag{2.54}$$
$$\omega_c^2 = \omega^2 + \Omega^2,$$

where ω_c^2 is the frequency that one of the oscillators would have if the other one was held fixed.

Combining equations in (2.53), one can get:

$$x_1(t) - x_2(t) = Asin(\omega_+ t + C) + Bsin(\omega_- t + D) + Asin(\omega_+ t + C) - Bsin(\omega_- t + D),$$
$$x_1(t) + x_2(t) = Asin(\omega_+ t + C) + Bsin(\omega_- t + D) - Asin(\omega_+ t + C) + Bsin(\omega_- t + D). \tag{2.55}$$

After some simplifications, the following set of equations is obtained:

$$\frac{1}{2A}(x_1(t) - x_2(t)) = Asin(\omega_+ t + C),$$
$$\frac{1}{2B}(x_1(t) + x_2(t)) = Bsin(\omega_- t + D). \tag{2.56}$$

The normal modes ω_+ and ω_- are not related to the motion of either of the oscillators. To find them, one needs to observe both oscillators at once.
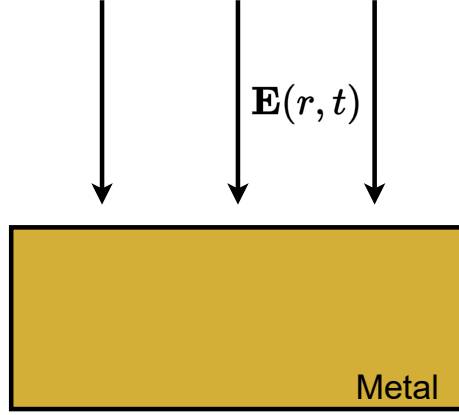
Figure 2. Metal Structure Under Electromagnetic Radiation

Going closer to the subject that is the focus of this thesis, the setup where the electromagnetic radiation is shining from the top of a metal is considered (see Fig. 2).

Electrons in the metal can be treated as a harmonic damped oscillator driven under the electromagnetic field $E(r, t)$. The equation of motion of the following system is:

$$m(\ddot{r} + \gamma \dot{r} + \omega_0^2 r) = -eE(r, t), \tag{2.57}$$

where e is the electron charge, m is the electron mass, ω_0 is the frequency of the harmonic oscillator, and γ is the damping coefficient.

Assuming that electromagnetic field is harmonic, i.e. $E(r, t) = E_0 e^{-i\omega t}$, one can obtain the steady-state solution as:

$$r = -\frac{e}{m} \frac{1}{\omega_0^2 - \omega^2 - i\gamma\omega} E_0 e^{i\omega t}. \tag{2.58}$$

The macroscopic polarization P is the average dipole moment per unit volume V. The average dipole moment is the product of the electron charge and its position. In other words, it is:

$$p = -er = -\frac{e^2}{m} \frac{1}{\omega_0^2 - \omega^2 - i\gamma\omega} E_0 e^{i\omega t}. \tag{2.59}$$

Then macroscopic polarization becomes:

$$P = \frac{Ne^2}{Vm} \frac{1}{\omega_0^2 - \omega^2 - i\gamma\omega} E_0 e^{i\omega t}. \tag{2.60}$$

20

The linear susceptibility is:

$$\chi(\omega) = \frac{P}{\epsilon_0 E} = \frac{Ne^2}{V\epsilon_0 m} \frac{1}{\omega_0^2 - \omega^2 - i\gamma\omega}. \tag{2.61}$$

One can set $\chi(\omega) = \chi'(\omega) + i\chi''(\omega)$, where $\chi'(\omega) = \frac{Ne^2}{V\epsilon_0 m} \frac{\omega_0^2 - \omega^2}{(\omega_0^2 - \omega^2)^2 + (\gamma\omega)^2}$ is the real part of the susceptibility and $\chi''(\omega) = \frac{Ne^2}{V\epsilon_0 m} \frac{\gamma\omega}{(\omega_0^2 - \omega^2)^2 + (\gamma\omega)^2}$ is the imaginary part of the susceptibility that describes dissipation.

Taking a limit that $\omega \gg \gamma$, the real and imaginary parts of the susceptibility become:

$$\chi'(\omega) \simeq -\frac{Ne^2}{2V\epsilon_0 m\omega_0} \frac{\omega - \omega_0}{(\omega - \omega_0)^2 + \frac{\gamma^2}{4}},$$

$$\chi''(\omega) \simeq -\frac{Ne^2\gamma}{4V\epsilon_0 m\omega_0} \frac{1}{(\omega - \omega_0)^2 + \frac{\gamma^2}{4}}. \tag{2.62}$$

The dispersion relation for SPP that propagates along the interface between a metal and a dielectric is (Raether 1988):

$$k_{SPP} = \frac{\omega}{c} \sqrt{\frac{\epsilon_1 \epsilon_2}{\epsilon_1 + \epsilon_2}}, \tag{2.63}$$

where ϵ_1 and ϵ_2 are the relative permittivities of a metal and a dielectric.

Then the momentum κ is:

$$\kappa^2 = \omega^2(1 + \chi(\omega)) = \omega^2 \left(1 + \frac{Ne^2}{V\epsilon_0 m} \frac{1}{\omega_0^2 - \omega^2 - i\gamma\omega}\right). \tag{2.64}$$

Equation (2.64) is called 'dispersion relation'. It can be rewritten as:

$$\frac{(\kappa + \omega)(\kappa - \omega)}{\omega^2} = \frac{Ne^2}{V\epsilon_0 m} \frac{1}{(\omega_0 + \omega)(\omega_0 - \omega)}. \tag{2.65}$$

Assuming $\omega \simeq \omega_0$, the following assumptions can be made: $(\kappa + \omega) \simeq 2\omega_0$, $(\omega_0 + \omega) \simeq 2\omega_0$, $\omega^2 \simeq \omega_0^2$. Then the dispersion relation becomes:

$$(\kappa - \omega)(\omega_0 - \omega) = \frac{Ne^2}{4V\epsilon_0 m}. \tag{2.66}$$

The solution to this equation is:

$$\omega_{\pm} = \frac{\kappa}{2} + \frac{\omega_0}{2} \pm \frac{1}{2}\sqrt{\frac{Ne^2}{V\varepsilon_0 m} + (\kappa - \omega_0)^2}. \tag{2.67}$$

When $\kappa = \omega_0$, the difference in the energies ω_- and ω_+ is $\sqrt{\frac{Ne^2}{V\varepsilon_0 m}}$. It is called 'normal mode splitting' and denoted as Ω. The analogy for this splitting is Rabi splitting. The quantum theory gives exactly this dependence on the concentration of the emitters. Interesting to note, that it is not possible to distinguish between classical and quantum emitters by knowing just the size of the splitting. It is important to add that the splitting in frequencies implies the energy exchange between the SPP field and the emitters.

Chapter 3

NUMERICAL METHODS

Maxwell's equations (2.1) are used to describe the propagation of electromagnetic waves. Since they are partial differential equations, analytical solutions exist in only a few simple cases. Hence, many electromagnetic wave interaction problems are solved by numerical methods.

The Finite-Difference Time-Domain (FDTD) method (Yee 1966) was the first technique in this class. Since about 1990, when engineers in the general electromagnetic community became aware of the modeling capabilities afforded by FDTD and related techniques, the interest in this area has been rapidly expanded (Taflove 1998).

3.1   FDTD

The method employs finite differences as approximations of the spatial and temporal derivatives that contain in Maxwell's equations.

Taking the Taylor series expansions of the function $f(x)$ expanded about the point x_0 with an offset of $\pm \frac{\partial}{2}$:

$$f\left(x_0 - \frac{\partial}{2}\right) = f(x_0) - \frac{\partial}{2}f'(x_0) + \frac{1}{2!}\left(\frac{\partial}{2}\right)^2 f''(x_0) - \frac{1}{3!}\left(\frac{\partial}{2}\right)^3 f'''(x_0) + \dots , \quad (3.1a)$$

$$f\left(x_0 + \frac{\partial}{2}\right) = f(x_0) + \frac{\partial}{2}f'(x_0) + \frac{1}{2!}\left(\frac{\partial}{2}\right)^2 f''(x_0) + \frac{1}{3!}\left(\frac{\partial}{2}\right)^3 f'''(x_0) + \dots . \quad (3.1b)$$

Subtracting equation (3.1b) from (3.1a) and dividing by ∂, one can obtain:

$$\frac{f\left(x_0 + \frac{\partial}{2}\right) - f\left(x_0 - \frac{\partial}{2}\right)}{\partial} = f'(x_0) + \frac{1}{3!}\frac{\partial^2}{2^2}f'''(x_0) + \dots . \quad (3.2)$$

After some simple transformations, one can come up with the following expression:

$$\frac{df(x)}{dx}\bigg|_{x=x_0} = \frac{f\left(x_0 + \frac{\delta}{2}\right) - f\left(x_0 - \frac{\delta}{2}\right)}{\delta} + \mathcal{O}(\delta^2). \tag{3.3}$$

If δ is sufficiently small, then δ^2 is neglectfully small. Thus, the central-difference approximation is given by:

$$\frac{df(x)}{dx}\bigg|_{x=x_0} \simeq \frac{f\left(x_0 + \frac{\delta}{2}\right) - f\left(x_0 - \frac{\delta}{2}\right)}{\delta} \tag{3.4}$$

FDTD employs second-order central differences. It solves electric and magnetic fields together in time and space.
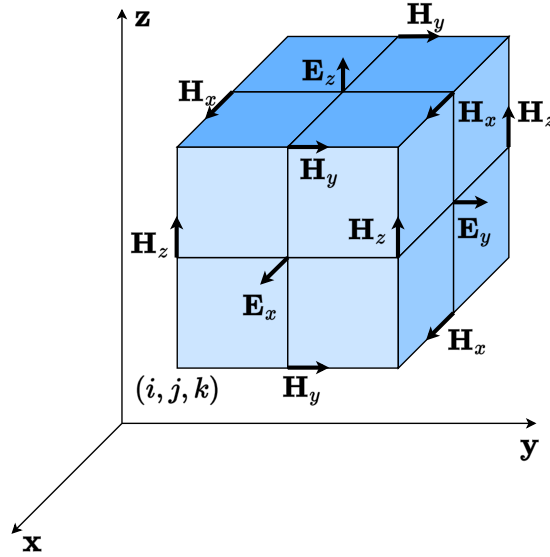
Figure 3. FDTD Cell Structure

As shown in Fig. 3, the Yee algorithm centers its **E** and **H** components in three-dimensional space, so that every **E** component is surrounded by four circulating **H** components, and every **H** component is surrounded by four circulating **E** components. Continuity of tangential **E** and **H** is naturally maintained across an interface of dissimilar materials if the interface is parallel to one of the coordinate axes.

Employing a leapfrog method, all the **E** values in the modeled space are computed and stored in memory for a particular time point using previously stored **H** values. Then **H** values are com-

puted and stored in memory using **E** values just computed. The cycle begins again with the re-computation of the **E** components based on the newly obtained **H**. This process continues until time-stepping is concluded.

Diving into more details of the following approach, it can be shown how the problem could be solved for the electromagnetic radiation.

Let Yee computational cell be defined by three indices (i, j, k):

- Evaluate three components of both **E** and **J** at the locations of $(i + \frac{1}{2}, j, k)$, $(i, j + \frac{1}{2}, k)$, $(i, j, k + \frac{1}{2})$, respectively;

- Evaluate three components of **H** at the locations of $(i, j + \frac{1}{2}, k + \frac{1}{2})$, $(i + \frac{1}{2}, j, k + \frac{1}{2})$, $(i + \frac{1}{2}, j + \frac{1}{2}, k)$, respectively;

- Discretize all the derivatives in Ampere's and Faraday's laws with finite differences;

- Solve the resulting difference equations to obtain 'update equations' that express the future fields in terms of past fields;

- Evaluate the magnetic fields one time-step into the future, so they are now known;

- Evaluate the electric fields one time-step into the future, so they are now known;

- Repeat the previous two steps until the fields have been obtained over the desired duration.

A similar approach is used once one includes equations for the hydrodynamic model to describe the motion of electrons in the metal.

Faraday's and Ampere's laws are:

$$
-\mu_0 \frac{\partial \mathbf{H}}{\partial t} = \nabla \times \mathbf{E} = \begin{vmatrix} \mathbf{x_0} & \mathbf{y_0} & \mathbf{z_0} \\ \frac{\partial}{\partial x} & \frac{\partial}{\partial y} & \frac{\partial}{\partial z} \\ E_x & E_y & E_z \end{vmatrix} \tag{3.5}
$$

25

$$J + \varepsilon_0 \frac{\partial \mathbf{E}}{\partial t} = \nabla \times \mathbf{H} = \begin{vmatrix} \mathbf{x_0} & \mathbf{y_0} & \mathbf{z_0} \\ \frac{\partial}{\partial x} & \frac{\partial}{\partial y} & \frac{\partial}{\partial z} \\ H_x & H_y & H_z \end{vmatrix} \tag{3.6}$$

The components of equations (3.5) and (3.6) can be rewritten as:

$$
\begin{aligned}
-\mu_0 \frac{\partial H_x}{\partial t} &= \frac{\partial E_z}{\partial y} - \frac{\partial E_y}{\partial z}, \\
-\mu_0 \frac{\partial H_y}{\partial t} &= \frac{\partial E_x}{\partial z} - \frac{\partial E_z}{\partial x}, \\
-\mu_0 \frac{\partial H_z}{\partial t} &= \frac{\partial E_y}{\partial x} - \frac{\partial E_x}{\partial y},
\end{aligned}
\tag{3.7}
$$

$$
\begin{aligned}
J_x + \varepsilon_0 \frac{\partial E_x}{\partial t} &= \frac{\partial H_z}{\partial y} - \frac{\partial H_y}{\partial z}, \\
J_y + \varepsilon_0 \frac{\partial E_y}{\partial t} &= \frac{\partial H_x}{\partial z} - \frac{\partial H_z}{\partial x}, \\
J_z + \varepsilon_0 \frac{\partial E_z}{\partial t} &= \frac{\partial H_y}{\partial x} - \frac{\partial H_x}{\partial y}.
\end{aligned}
\tag{3.8}
$$

Yee's scheme assumes that $\mathbf{E}$ and $\mathbf{H}$ are shifted in space by half a cell and in time by half a time step when considering a central difference approximation of the derivatives. In such case, equations (3.7) and (3.8) become:

$$
\begin{aligned}
-\mu_0 &\frac{H_x^{n+1}(i, j+1/2, k+1/2) - H_x^n(i, j+1/2, k+1/2)}{\varDelta t} = \\
&\frac{E_z^{n+1/2}(i, j+1, k) - E_z^{n+1/2}(i, j, k)}{\varDelta y} - \frac{E_y^{n+1/2}(i, j, k+1) - E_y^{n+1/2}(i, j, k)}{\varDelta z}, \\
-\mu_0 &\frac{H_y^{n+1}(i+1/2, j, k+1/2) - H_y^n(i+1/2, j, k+1/2)}{\varDelta t} = \\
&\frac{E_x^{n+1/2}(i, j, k+1) - E_x^{n+1/2}(i, j, k)}{\varDelta z} - \frac{E_z^{n+1/2}(i+1, j, k) - E_z^{n+1/2}(i, j, k)}{\varDelta x}, \\
-\mu_0 &\frac{H_z^{n+1}(i+1/2, j+1/2, k) - H_z^n(i+1/2, j+1/2, k)}{\varDelta t} = \\
&\frac{E_y^{n+1/2}(i+1, j, k) - E_y^{n+1/2}(i, j, k)}{\varDelta x} - \frac{E_x^{n+1/2}(i, j+1, k) - E_x^{n+1/2}(i, j, k)}{\varDelta y},
\end{aligned}
\tag{3.9}
$$

$$J_x + \epsilon_0 \frac{E_x^{n+1/2}(i+1/2,j,k) - E_x^{n-1/2}(i+1/2,j,k)}{\Delta t} =$$
$$\frac{H_z^n(i+1/2,j+1/2,k) - H_z^n(i+1/2,j-1/2,k)}{\Delta y} -$$
$$\frac{H_y^n(i+1/2,j,k+1/2) - H_y^n(i+1/2,j,k-1/2)}{\Delta z},$$

$$J_y + \epsilon_0 \frac{E_y^{n+1/2}(i,j+1/2,k) - E_y^{n-1/2}(i,j+1/2,k)}{\Delta t} =$$
$$\frac{H_x^n(i,j+1/2,k+1/2) - H_x^n(i,j+1/2,k-1/2)}{\Delta z} -$$
$$\frac{H_z^n(i+1/2,j+1/2,k) - H_z^n(i-1/2,j+1/2,k)}{\Delta x}, \qquad (3.10)$$

$$J_z + \epsilon_0 \frac{E_z^{n+1/2}(i,j,k+1/2) - E_z^{n-1/2}(i,j,k+1/2)}{\Delta t} =$$
$$\frac{H_y^n(i+1/2,j,k+1/2) - H_y^n(i-1/2,j,k+1/2)}{\Delta x} -$$
$$\frac{H_x^n(i,j+1/2,k+1/2) - H_x^n(i,j-1/2,k+1/2)}{\Delta y}.$$

Equations (3.9) and (3.10) show the usefulness of FDTD approach in finding a central difference approximation for the derivatives. In particular, the left term in (3.9) means that the derivative of **H** field at time $(n+\frac{1}{2})\Delta t$ can be expressed as a central difference using **H** field values at times $(n+1)\Delta t$ and $n\Delta t$. The right term in (3.9) approximates the derivative of **E** field at points $(i+\frac{1}{2})\Delta x$, $(j+\frac{1}{2})\Delta y$, and $(k+\frac{1}{2})\Delta z$ as a central difference using **E** field values at points $(i+1)\Delta x$ and $i\Delta x$, $(j+1)\Delta y$ and $j\Delta y$, $(k+1)\Delta z$ and $k\Delta z$, respectively. Similarly, the left term in (3.10) shows that the derivative of **E** field at time $n\Delta t$ can be expressed as a central difference using **E** field values at times $(n+\frac{1}{2})\Delta t$ and $(n-\frac{1}{2})\Delta t$. The right term in (3.10) approximates the derivative of **H** field at points $i\Delta x$, $j\Delta y$, and $k\Delta z$ as a central difference using **H** field values at points $(i+\frac{1}{2})\Delta x$ and $(i-\frac{1}{2})\Delta x$, $(j+\frac{1}{2})\Delta y$ and $(j-\frac{1}{2})\Delta y$, $(k+\frac{1}{2})\Delta z$ and $(k-\frac{1}{2})\Delta z$, respectively.

This scheme is known as 'leap-frog' algorithm. In order to approximate Maxwell's equations in space and time using this algorithm, one should calculate first all **H** field values, then all **E** field values, remembering always that **E** and **H** are shifted in space by half of the discretization Δx, Δy, Δz.

The explicit FDTD equations can be derived from equations (3.9) and (3.10):

$$H_x^{n+1}(i, j + 1/2, k + 1/2) = H_x^n(i, j + 1/2, k + 1/2)-$$

$$\frac{\Delta t}{\mu_0} \left(\frac{E_z^{n+1/2}(i, j + 1, k) - E_z^{n+1/2}(i, j, k)}{\Delta y} - \frac{E_y^{n+1/2}(i, j, k + 1) - E_y^{n+1/2}(i, j, k)}{\Delta z} \right),$$

$$H_y^{n+1}(i + 1/2, j, k + 1/2) = H_y^n(i + 1/2, j, k + 1/2)-$$

$$\frac{\Delta t}{\mu_0} \left(\frac{E_x^{n+1/2}(i, j, k + 1) - E_x^{n+1/2}(i, j, k)}{\Delta z} - \frac{E_z^{n+1/2}(i + 1, j, k) - E_z^{n+1/2}(i, j, k)}{\Delta x} \right),$$

(3.11)

$$H_z^{n+1}(i + 1/2, j + 1/2, k) = H_z^n(i + 1/2, j + 1/2, k)-$$

$$\frac{\Delta t}{\mu_0} \left(\frac{E_y^{n+1/2}(i + 1, j, k) - E_y^{n+1/2}(i, j, k)}{\Delta x} - \frac{E_x^{n+1/2}(i, j + 1, k) - E_x^{n+1/2}(i, j, k)}{\Delta y} \right),$$

$$E_x^{n+1/2}(i + 1/2, j, k) = E_x^{n-1/2}(i + 1/2, j, k)+$$

$$\frac{\Delta t}{\epsilon_0} \left(-J_x + \frac{H_z^n(i + 1/2, j + 1/2, k) - H_z^n(i + 1/2, j - 1/2, k)}{\Delta y} - \right.$$

$$\left. \frac{H_y^n(i + 1/2, j, k + 1/2) - H_y^n(i + 1/2, j, k - 1/2)}{\Delta z} \right),$$

$$E_y^{n+1/2}(i, j + 1/2, k) = E_y^{n-1/2}(i, j + 1/2, k)+$$

$$\frac{\Delta t}{\epsilon_0} \left(-J_y + \frac{H_x^n(i, j + 1/2, k + 1/2) - H_x^n(i, j + 1/2, k - 1/2)}{\Delta z} - \right.$$

(3.12)

$$\left. \frac{H_z^n(i + 1/2, j + 1/2, k) - H_z^n(i - 1/2, j + 1/2, k)}{\Delta x} \right),$$

$$E_z^{n+1/2}(i, j, k + 1/2) = E_z^{n-1/2}(i, j, k + 1/2)+$$

$$\frac{\Delta t}{\epsilon_0} \left(-J_z + \frac{H_y^n(i + 1/2, j, k + 1/2) - H_y^n(i - 1/2, j, k + 1/2)}{\Delta x} - \right.$$

$$\left. \frac{H_x^n(i, j + 1/2, k + 1/2) - H_x^n(i, j - 1/2, k + 1/2)}{\Delta y} \right).$$

These equations can be directly implemented in a computer code.

For stability reasons, a field component cannot propagate more than one cell size in the time step Δt. This means that in general, the stability condition (Courant, Friedrichs, and Lewy 1967)

28

is:

$$\Delta t \leq \frac{\Delta}{c_0 \sqrt{d}}, \tag{3.13}$$

where c_0 is the speed of light, $d = 3$ for three-dimensional problem, and Δ is the minimal distance between the cells.

A common choice for Δt is given by:

$$\Delta t = \frac{\Delta}{2c_0}. \tag{3.14}$$

3.2   Perfectly Matched Layers

One of the greatest challenges of the FDTD method has been the efficient and accurate solution of electromagnetic wave interaction problems in unbounded regions. An Absorbing Boundary Condition (ABC) should be introduced at the outer lattice boundary to simulate the extension of the lattice to infinity (Taflove 1998). An alternative approach to implement an ABC is to terminate the outer boundary of the space lattice in an absorbing material medium. The lossy medium has been used with limited success as an absorbing layer to terminate the outer boundary of the FDTD space lattice. A major difficulty is that this medium is matched to the interior of the lattice only for normally incident waves. Therefore, oblique waves partially reflect back into the computation region and corrupt the solution. As a result, this absorber is not useful for most problems of practical interest.

Since 1994, a new fervor in this area has been created by Berenger's introduction of a highly effective absorbing-material ABC designated the Perfectly Matched Layers (PML) (Berenger 1994).

The innovation of Berenger's PML is that plane waves of arbitrary incidence, polarization, and frequency are matched at the boundary.

In his pioneering work, Berenger derived a novel split-field formulation of Maxwell's equations where each vector field component is split into two orthogonal components. Maxwell's curl equations were also appropriately split, leading to a set of 12 coupled first-order partial differential equations. Then a perfectly matched planar interface is derived by choosing loss parameters consistent with a dispersionless medium.

There are several equivalent formulations of PML. Berenger's original formulation is called the split-field PML because he artificially split the wave solutions into the sum of two new artificial field components. Nowadays a more frequently used formulation is the Uniaxial PML (UPML), which expresses the PML region as the ordinary wave equation with a combination of artificial anisotropic absorbing materials. Both of these formulations were originally derived by laboriously computing the solution for a wave incident on the absorber interface at an arbitrary angle (and polarization, for vector waves), and then solving for the conditions in which the reflection is always zero. It turns out that both the split-field and UPML formulations can be derived in a much more elegant and general way, by viewing them as the result of a complex coordinate stretching. It is a complex-coordinate approach, which is essentially based on the analytic continuation of Maxwell's equations into complex spatial coordinates, where the fields are exponentially decaying.

3.3   Total/Scattered Field Approach

An efficient technique to compute scattered fields in the context of FDTD modeling is the Total-Field/Scattered-Field (TF/SF) incident wave source (Taflove 1998). Fundamentally, the TF/SF technique is an application of the well-known electromagnetic field equivalence principle (Stratton 2007; Harrington 1961; Balanis 2012).

By this principle, the original incident wave of infinite extent and arbitrary propagation di-
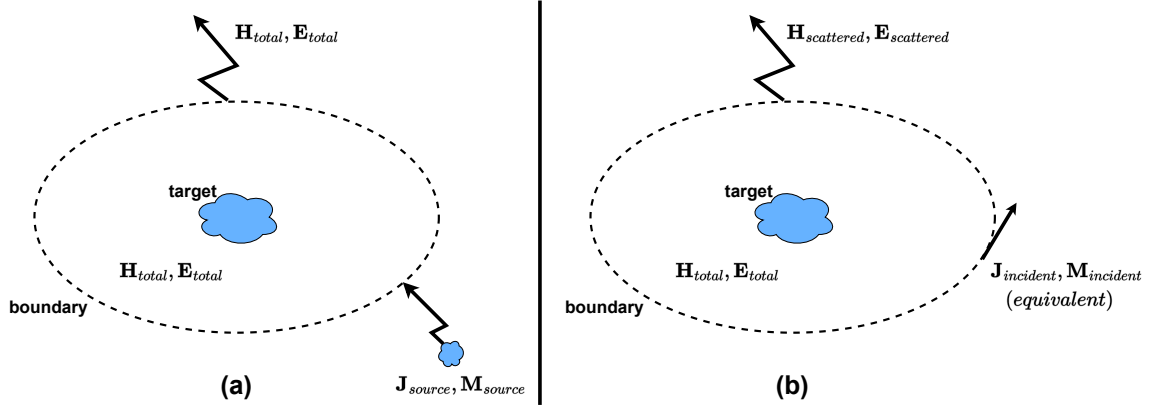
Figure 4. Equivalence Principle for Wave Scattering by a Target

Note: Original problem (a); equivalent problem (b).

rection, polarization, and time waveform is replaced by electric and magnetic current sources, appropriately defined on a finite closed surface containing the object of interest (Taflove, Oskooi, and Johnson 2013).

The reformulated problem confines the incident illumination to a compact total-field region and provides a finite scattered-field region external to the total-field region that is terminated by an ABC to simulate the FDTD grid extending to infinity.

Fig. 4 illustrates the application of the equivalence principle to electromagnetic wave scattering by an arbitrary target located in an unbounded region. Here the incident wave is generated by the electric and magnetic current sources, $\mathbf{J}_{source}$ and $\mathbf{M}_{source}$. In Fig. 4a, the interaction of the incident wave with the target results in the formation of a total electric field $\mathbf{E}_T$ and a total magnetic field $\mathbf{H}_T$ that fills all space. Each of these fields can be viewed as a sum of an incident component and a scattered component, i.e., $\mathbf{E}_T = \mathbf{E}_{inc} + \mathbf{E}_S$ and $\mathbf{H}_T = \mathbf{H}_{inc} + \mathbf{H}_S$.

Using the equivalence principle, the reformulated problem shown in Fig. 4b separates space into two regions: an interior region where total fields exist, and an exterior region where only scattered fields exist. Here the original incident field is generated only within the total field region by equivalent electric and magnetic current sources, $\mathbf{J}_{inc}$ and $\mathbf{M}_{inc}$, existing on the TF/SF boundary,

$\partial\Omega$. TF/SF approach provides several advantages that enhance the computational power and dynamic range of the FDTD method (fewer restrictions for the incident field, presence of two regions simplifies the implementation of ABC, easy far-field detection, etc.).

3.4   MPI

Message Passing Interface (MPI) is a specification for developers and users of message passing libraries. By itself, it is not a library, but the specification of what such a library should be.

MPI primarily addresses the message-passing parallel programming model: data is moved from the address space of one process to that of another process through cooperative operations on each process (Pacheco 1997).
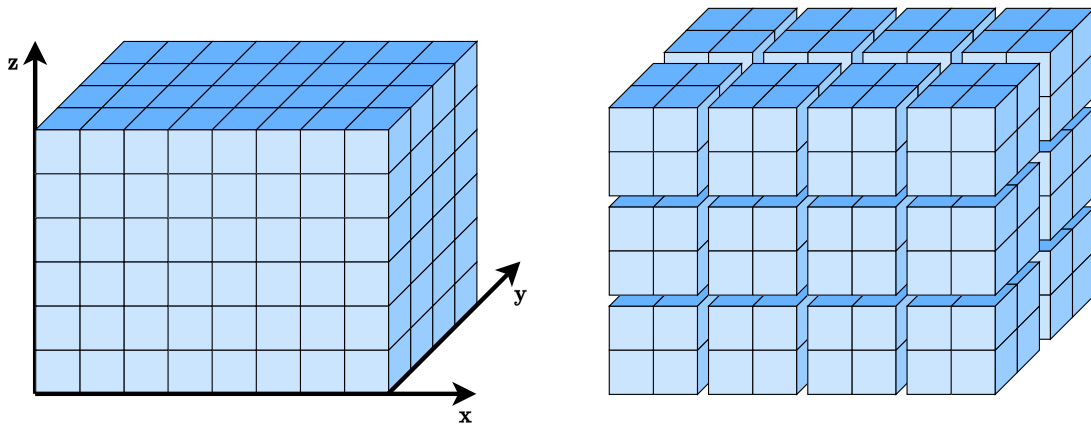

Figure 5. 3D Domain Decomposition Using a 4 × 2 × 3 Grid

Simply, the goal of MPI is to provide a widely used standard for writing message passing programs.

The approach consists of the following steps:

1. Break up the lattice into boxes in accordance with how many processes can be used;

2. Assign boxes to MPI processes one-to-one (each process updates only a single box);

3. Add subroutine calls to places where data from different boxes is needed (each process should have a 'map' of its neighbors).

In the present thesis, the codes are parallelized using the domain decomposition method and MPI. In the case of 2D structures, all simulations are performed at the local computer cluster. A typical number of computing cores used for a single run is 64 with an average execution time of 10-20 minutes. As for the 3D structures, for convergence test runs a local computer cluster was utilized. To obtain the results, the following high performance computing services were used: Agave supercomputer (Arizona State University) and U.S. Air Force research laboratory Department of Defense supercomputing resource center. Typical execution time of the codes varied between 10 - 20 minutes for linear regime and 80 - 90 minutes to obtain nonlinear results. A typical number of computing cores used for a single production run varied between $12 \times 12 \times 8 = 1152$ and $12 \times 12 \times 16 = 2304$.

The numerical convergence in both linear and nonlinear regimes is achieved for a spatial resolution from 1.0 nm to 1.5 nm and a time step from 2.0 as to 2.5 as.

To probe the system under consideration, the TF/SF approach is employed. The open boundaries are terminated via convolutional PML. Linear spectra are simulated using the short pulse method, which allows one to obtain reflection/transmission spectra in a single FDTD run. The nonlinear power spectra are simulated using 100 fs and 200 fs incident pulse.

Chapter 4

SECOND HARMONIC GENERATION

Discovery of the Second Harmonic Generation (SHG) process (Franken et al. 1961) is often considered as the birth of nonlinear optics. This process is very important because of the various applications: nonlinear microscopy, shifting the output frequency of lasers, investigating the surface properties of various structures and materials.

(a) (b)
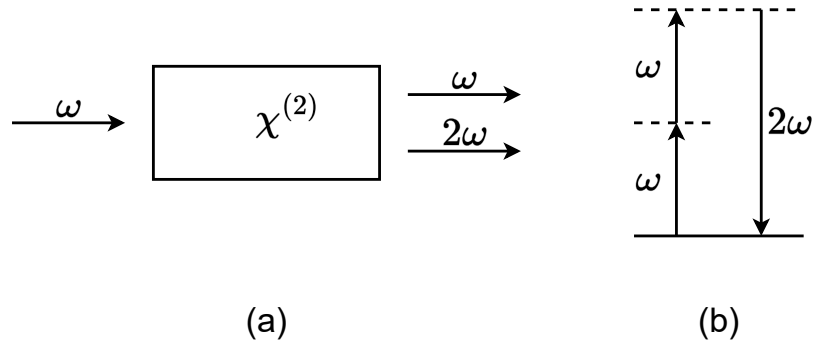
Figure 6. Concept of SHG

Note: Process of SHG (a); energy level diagram (b).

The basic process of SHG is illustrated in Fig. 6. If an external electric field at a frequency ω is applied to a media, then the output radiation will be at frequency of ω as well as 2ω. The transfer of energy from the incident field to the output radiation can be imagined in terms of the energy level diagram (see Fig. 6). Two photons are lost to the input beam and one photon at frequency 2ω is created.

The polarization can be expanded in terms of the applied electric field, i.e.:

$$\mathbf{P}(t) = \epsilon_0 \left(\chi^{(1)} \mathbf{E}(t) + \chi^{(2)} \mathbf{E}^2(t) + \chi^{(3)} \mathbf{E}^3(t) + ... \right), \tag{4.1}$$

where the coefficients $\chi^{(n)}$ are the nth order susceptibilities of the medium.

The following chapter is dedicated to the SH investigation. It is shown that the second-order optical response can be significantly changed under the different polarization of the incident pulse, the shape of the medium, etc. Also, a comparison of the simulated data and the experimental results, quantitatively and qualitatively, is presented.

4.1 High Yield Synthesis and Quadratic Nonlinearities of Gold Nanoprisms in Solution: the Role of Corner Sharpness

Strong harmonic emission of the metallic nanoprisms has been already discussed (Salomon et al. 2014). But there is a lack of data on the values of hyperpolarizabilities β for gold nanoprisms. And to the best of my knowledge, there is no detailed investigation of the dependence of β on the particle surface area or corner sharpness. In the present chapter, the gold nanoprisms have been investigated. By varying their parameters (the radii curvature, side size), the influences on the hyperpolarizability is analyzed. Also, the comparison of the experimental data and numerical results is provided. It has been shown that by utilizing the hydrodynamic Drude model only, a good agreement between experiments and calculations is achieved not only qualitatively, but also quantitatively.

4.1.1 Analytical Derivation of the Hyperpolarizability

A finite structure of the nanosprisms is considered. To account for its nonlinear response, the hydrodynamic model (2.31) is used. The electromagnetic response of the plasmonic system is accounted for by Maxwell's equations (2.1). Those equations are discretized in space and time following the FDTD approach.

To describe gold, the following parameters are used: the equilibrium number density of con-

35

duction electrons $n_0 = 5.9 \times 10^{28}$ m^{-3}, Fermi energy $E_F = 5.53$ eV, effective electron mass $m^* = 1.64 \times m_e$, the phenomenological decay constant $\gamma_e = 0.18$ eV.

Starting off with the analytical investigation, the proposed approach includes the calculations of the scattering cross-section defined as:

$$C_{sca} = \frac{1}{I_{inc}} \oiint_A \mathbf{S}_{sca} \times d\mathbf{A}, \qquad (4.2)$$

where $I_{inc} = |\mathbf{S}_{inc}| = |[\mathbf{E}_{inc} \times \mathbf{H}^*_{inc}]|$ is the incident irradiance. It corresponds to the outgoing electromagnetic energy flux integrated over a Gaussian surface. The Poynting vector $\mathbf{S}_{sca}$ is the scattered electromagnetic field. In order to treat the nanoprism as a point dipole, it is assured that the Gaussian surface is in the far-field zone. After that, the linear response can be defined as:

$$p(\omega) = \epsilon_0 \epsilon_m \alpha(\omega) E_0(\omega), \qquad (4.3)$$

where ϵ_m is the relative permittivity of the media, in which the nanostructure is embedded, α is the linear polarizability, and E_0 is the peak amplitude of the pump.

Combining (4.2) with (4.3) and using the analytical solution for a point dipole (Greiner 2012), the scattering cross-section becomes:

$$C_{sca}(\omega) = \frac{\omega^4}{6\pi c^4} |\alpha(\omega)|^2. \qquad (4.4)$$

Then the absolute value of the polarizability can be extracted directly from the numerical integration of Maxwell's equations coupled to the equations describing the dynamics of conduction electrons in the metal interface.

One can consider a dipole moment as a summation of harmonic frequencies of the incident field, i.e.:

$$p = p_1(\omega)e^{i\omega t} + p_2(2\omega)e^{2i\omega t} + p_3(3\omega)e^{3i\omega t} + ..., \qquad (4.5)$$

where $p_1(\omega)e^{i\omega t}$ is the linear term that directly corresponds to (4.3).

36

The second- and third-order terms could be derived in the form similar to (4.3):

$$p_2(2\omega) = \epsilon_0 \epsilon_m \frac{1}{2} \beta(2\omega) : E_0(\omega)E_0(\omega),$$

$$p_3(3\omega) = \epsilon_0 \epsilon_m \frac{1}{3} \gamma(3\omega) : E_0(\omega)E_0(\omega)E_0(\omega),$$

(4.6)

where β and γ are the first and second hyperpolarizabilities, respectively.

The scattering cross-section calculated at the SH of the pump is:

$$C_{sca}(2\omega) = \frac{2\omega^4}{3\pi c^4} |\beta(2\omega)|^2 E_0^2.$$

(4.7)

Direct calculation of the scattering cross-section at the SH and subsequent comparison with equation (4.7) allow extracting hyperpolarizabilities directly.

4.1.2 Experimental and Numerical Analysis of Gold Nanoprisms

(a)   (b)
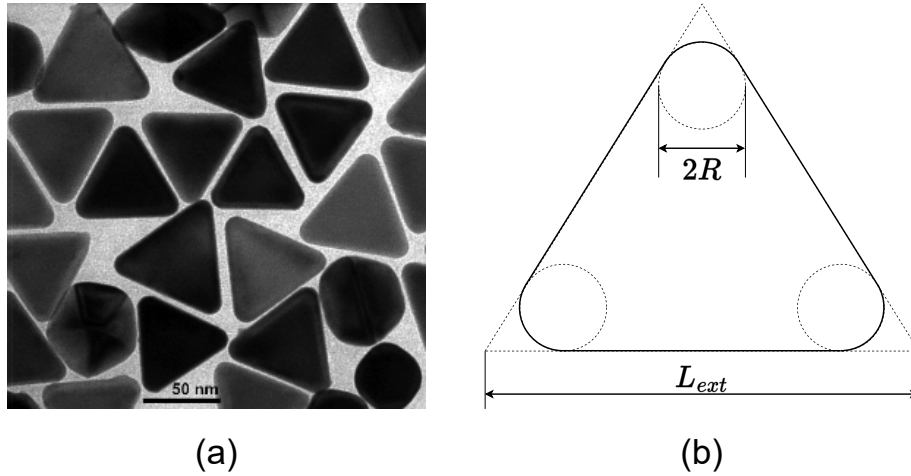
Figure 7. Initial Setup of the Gold Nanoprism

Note: TEM image (a); numerical representation (b).

Fig. 7 presents pictures of the nanoprisms in both experimental and computational setups. The size and shape of particles were determined by Transmission Electron Microscopy (TEM)

imaging (see Fig. 7a). The average thickness of the nanoprisms is 25 nm. This completely matches the simulation data.

In order to investigate the structures with different edge lengths and corner curvature radii, the relevant criterion for 'sharpness' is required for a quantitative analysis. A simple definition of sharpness with curvature radius is not enough. The relative effect of triangle tips rounding on their optical response, referred to as a 'snipping effect' (Shuford, Ratner, and Schatz 2005), ought to be more pronounced for small particles, whereas for large ones sharpness effects would be diluted with respect to other contributions, such as from the bulk.

Thus, a more sophisticated term to describe the sharpness of the nanoprisms should be introduced. It is called 'Sharpness Factor' (SF) and is defined as:

$$SF = \frac{L_{ext} - 2R}{L_{ext}}, \tag{4.8}$$

where L_{ext} is the external nanoprism side length and R is the triangle corner curvature radius.

Figure 8. Experimental (orange) and Calculated (blue) β Values as a Function of the Total Surface Area of the Nanoprisms

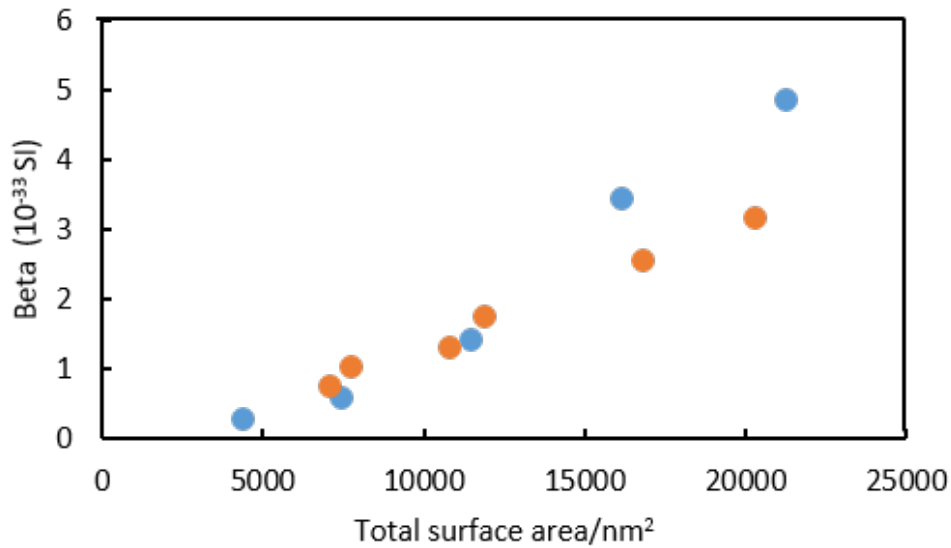Once the SF is identified, it is beneficial to evaluate the dependence of β on this term. Using the parameters sketched at Fig. 7b, one can easily derive the prism surface area A:

$$A = 3\left[\frac{L_{ext}^2}{4tan\frac{\pi}{3}} + \left(\frac{\pi}{3} - \sqrt{3}\right)R^2\right].\qquad(4.9)$$

The dependence of β on A is shown at Fig. 8. Dots show the values of β collected experimentally (orange) and numerically (blue) for different values of A. First, one can note that the experimental data exhibit similar dependence as the simulated ones. Second, the presented results are in satisfactory agreement. Even though there is a significant mismatch at larger A, a good agreement is archived for smaller A. Especially when one considers experimental errors on R and L_{ext} values inferred from TEM images and also difficulties to measure β. The mismatch on bigger A can be explained by the difficulties to stay in the far-field zone while the size of the nanoprism is increased. But it is numerically challenging since the expansion in the computation domain brings an increase of the execution time: time grows as $2N$, where N is the total amount of the grid points.

Since SF and A depend on two parameters R and L_{ext}, it is useful to fix one of them and observe how β is changing by tuning another one. The next set of graphs (see Fig. 9) has R fixed at 4.4 nm, 10 nm, 15 nm, and 25 nm and shows the dependence of β on A (slopes s are expressed in 10^{-36} nm^{-2}). There is a clear linear fit for all cases. Values of β noticeably decrease when R is increased. It confirms the strong influence of the corner curvature radius R on the nonlinear optical response of nanoprisms.

Fig. 10 displays the SF dependence of hyperpolarizability β on various values of R (slopes s are expressed in 10^{-36} nm^{-2}). Those plots confirm the strong influence of triangle corner radii on hyperpolarizability values. The slope of these plots decreases regularly and very rapidly when increasing R.

The linear dependence for SF is valid only when R is fixed. A narrow dispersion of curvature radii restricts the possibility to account for β dependence with SF.
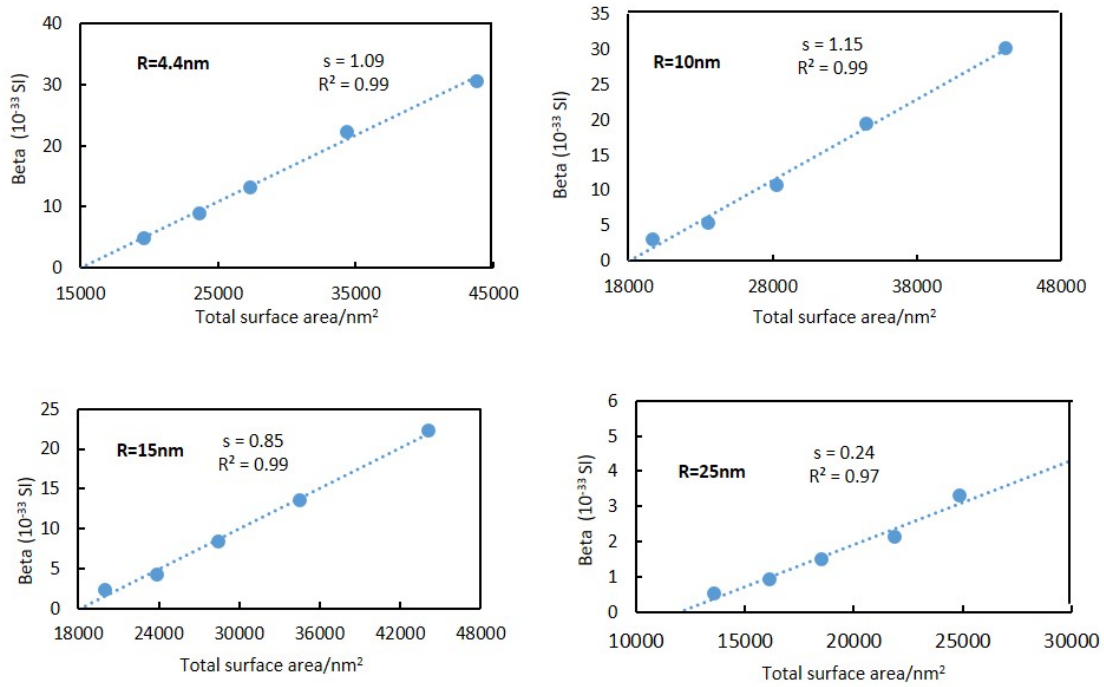
Figure 9. Total Surface Area Dependence of Calculated β Values for Different Curvature Radii

To sum up, systematic calculations were performed on gold nanoprisms with various edge lengths and corner radii. It has been shown that the influence of corner sharpness dominates over centrosymmetry breaking. These results shed new light on the SH properties of the structures with sharp corners. More investigation of this matter might open a new way to build new metal interfaces with the high nonlinear response coming from the particular geometrical setup, i.e. sharpness of the edges, etc.
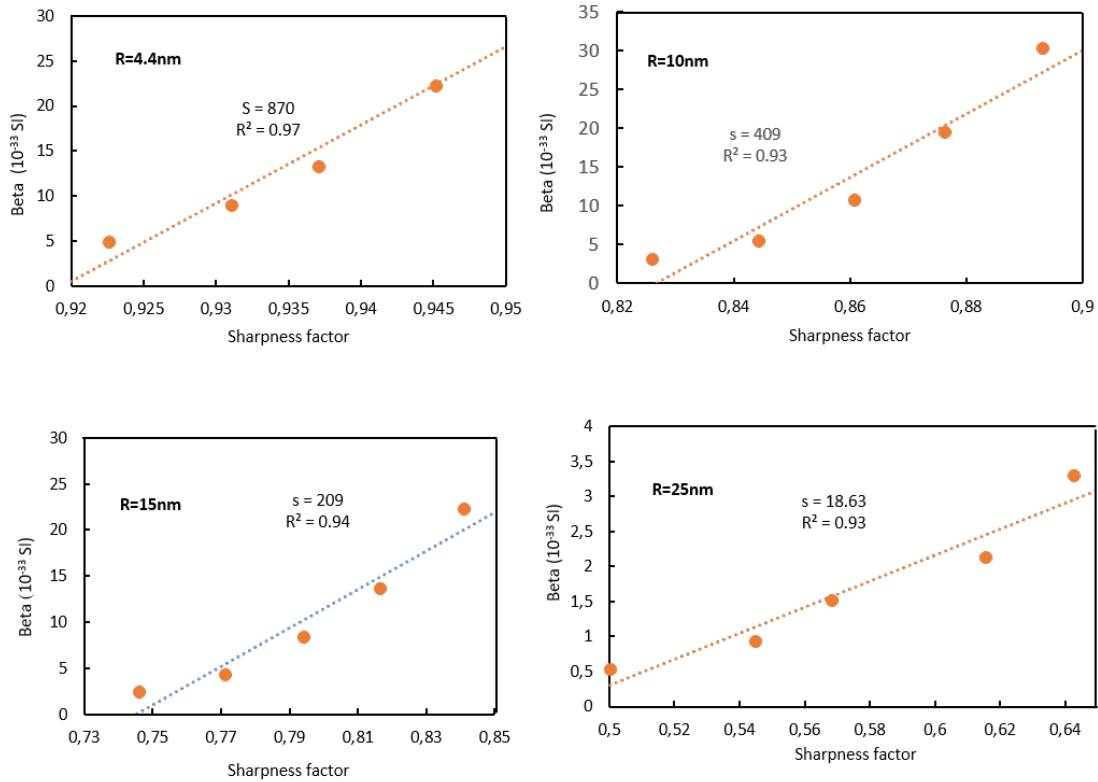
Figure 10. Sharpness Factor Dependence of Calculated β Values for Different Curvature Radii

4.2 Wavelength and Polarization Dependence of Second Harmonic Generation from Gold Nanocrescent Arrays

This section provides theoretical and experimental analysis of SH response from the gold (Au) nanocrescents. To fabricate Au nanocrescents (NCs), nanosphere template lithography was used (Cooper et al. 2014; Bukasov and Shumaker-Parry 2007). The Scanning Electron Microscope (SEM) images of the fabricated samples are provided in Fig. 11a, b. The difference between them is the size of the nanocrescents. The first one (see Fig. 11a) has an average tip-to-tip length L = 220 nm and an average width w = 85 nm. This sample is labeled as NC1. The

second nanocrescent NC2 (see Fig. 11b) is almost two times longer, but the width is almost the same, i.e., $L = 430$ nm and an average width $w = 90$ nm.
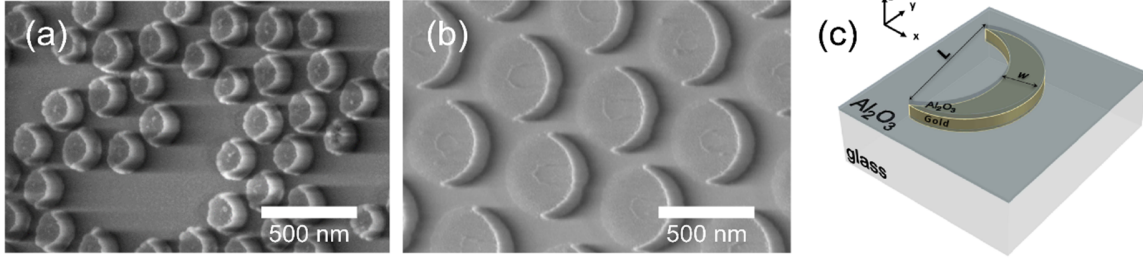
Figure 11. Initial Setup of NCs

Note: SEM images of NC1 (a) and NC2 (b); simulated unit cell (c).

From the computational side, a periodic array of Au NCs is considered with two different sets of parameters for L and w that match completely with the experimental setups, i.e.:

- NC1$'$: $L = 220$ nm, $w = 85$ nm;
- NC2$'$: $L = 430$ nm, $w = 90$ nm;

where apostrophe $'$ stands for computational results. The schematic computational cell is depicted in Fig. 11c.

The described structures are placed on top of a semi-infinite nondispersive dielectric slab with refractive index $n = 1.456$. The input side of the structure is covered by a thin layer of Al_2O_3 with refractive index $n = 1.765$. To simulate the dynamics of the light-matter interaction, Maxwell's equations (2.1) and the hydrodynamic model to describe the motion of the electrons in the metal interface (2.31) are used. Equations (2.1) and (2.31) are coupled and propagated in space and time. The following parameters are used to describe gold: the equilibrium number density of conduction electrons $n_0 = 5.9 \times 10^{28}$ m^{-3}, the plasma frequency $\Omega_p = \sqrt{\frac{n_0 e^2}{\varepsilon_0 m^*}} = 7.71$ eV, and the phenomenological decay constant $\gamma = 8.23 \times 10^{-2}$ eV.

In the simulations, the short pulse method is used to obtain the spectrum of the considered system. Fig. 12 summarizes the linear optical response, absorbance, from NC1 (see Fig. 12a, c) and NC2 (see Fig. 12b, d). The top row depicts the experimental data, the bottom row presents the simulated results. Different colors correspond to different polarization of the incident pulse:

- Blue line – incident light is polarized along Short Axis (SA) of NCs or 0°;
- Red line – incident light is polarized along Long Axis (LA) of NCs (perpendicular to SA) or 90°;
- Black line – incident light is polarized in between SA and LA or 45°.

The black dashed line in Fig. 12a shows the excitation pulse spectrum used in the SH spectroscopy measurements when the near-infrared output is tuned to 1300 nm.
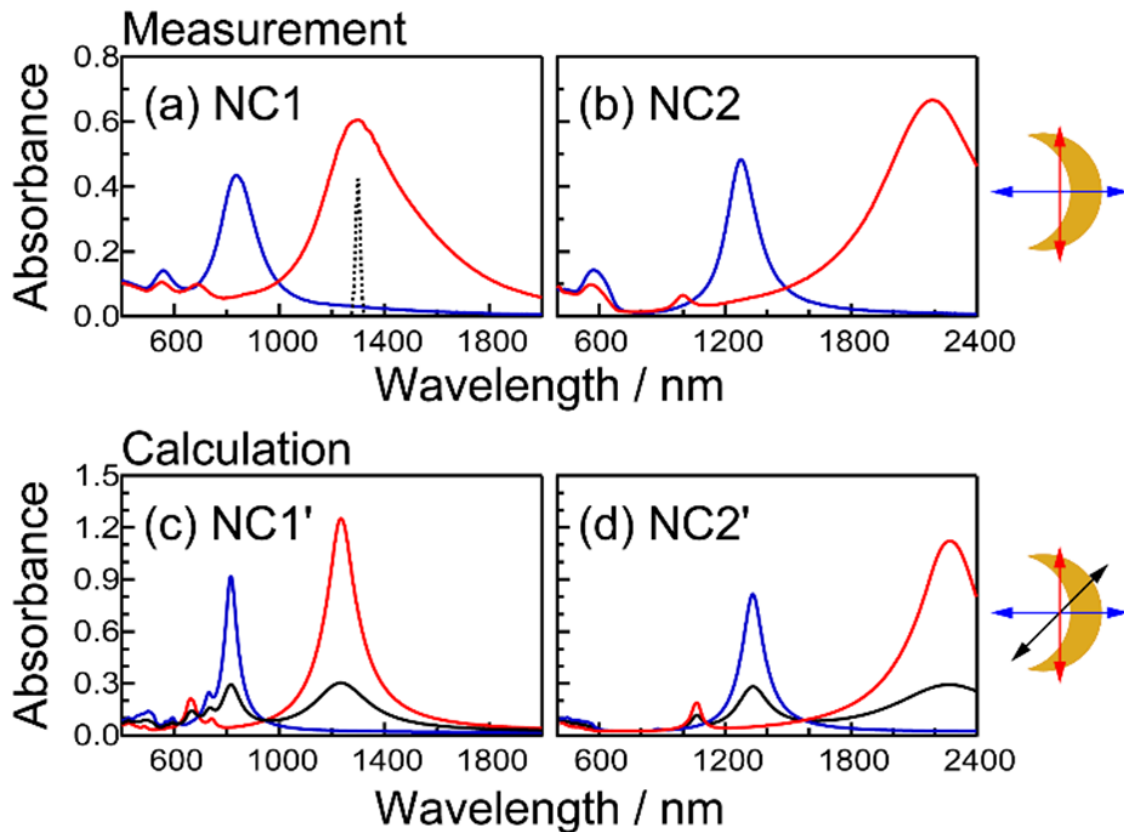
Figure 12. Experimental and Numerical Linear Absorbances for NC1 and NC2

Looking at Fig. 12, one can note that the responses under different polarizations change a lot. It means that the wavelength and polarization of the incident light play an important role in selectively exciting a specific NC plasmon resonance band. When the incident light is polarized along LA, there are two peaks for NC1 (at 1300 and 684 nm) due to the dipole and quadrupole resonances. In the case of NC2, the similar resonances are at 2190 and 1001 nm. For the polarization along SA, the dipole band is located at 840 nm for NC1 and at 1277 nm for NC2. Peaks at around 550-560 nm are insensitive to polarization and are assigned to out-of-plane dipole modes in the previous study (Shumaker-Parry, Rochholz, and Kreiter 2005). There is a clear redshift for NC2 resonances since it is larger than NC1.

Table 1. Comparison of Resonances for NC1

| | Dipole | | Quadrupole |
	LA, nm	SA, nm	LA, nm
Simulations	1300	840	684
Experiment	1237	815	661

Table 2. Comparison of Resonances for NC2

| | Dipole | | Quadrupole |
	LA, nm	SA, nm	LA, nm
Simulations	2190	1277	1001
Experiment	2270	1333	1065

To compare the experimental and computational results, tables (1) and (2) are provided. The agreement between the experimental results and the simulations is pretty remarkable. Small deviations might come from a small discrepancy in the initial parameters.

4.2.1 Nonlinear Regime

The surface symmetry of the NCs is C_{1h} – a symmetry with one mirror plane and without any rotational axis. Under the electric dipole approximation, the nonvanishing second-order nonlinear susceptibility elements are $\chi_{xxx}^{(2)}$, $\chi_{xyy}^{(2)}$, and $\chi_{yxy}^{(2)} = \chi_{yyx}^{(2)}$ (Lancaster and Shumaker-Parry 2016). The induced second-order nonlinear polarization $P_i^{(2)}(2\omega)$ along i-axis (i = x, y) is described as:

$$P_x^{(2)}(2\omega) \propto \chi_{xxx}^{(2)} cos^2\theta + \chi_{xyy}^{(2)} sin^2\theta,$$
$$P_y^{(2)}(2\omega) \propto \chi_{yxy}^{(2)} sin\theta cos\theta, \tag{4.10}$$

where θ is the angle between x-axis (SA of NCs) and the incident light polarization. This set of equations doesn't fully describe nonlinear effects in the system. Previous studies analyzed the incident polarization angle dependence of SH responses (Valev et al. 2009; Zdanowicz et al. 2011) on metallic nanostructures by the equation provided below:

$$P_i^{(2)}(2\omega) \propto \xi_{ixx}^{(2)} cos^2\theta + \xi_{ixy}^{(2)} sin\theta cos\theta + \xi_{iyy}^{(2)} sin^2\theta, \tag{4.11}$$

for i = x, y.

Here additional terms are added that are forbidden under the electric dipole approximation. They are needed to include nonlinear polarization effects induced by quadrupole and magnetic dipole interactions.

Fig. 13a, b show the polarization dependence of SH response on NC1 and NC2, respectively. The plots have been normalized to the maximal intensity. The polarization direction of the incident pulse is shown by the angle of those polar diagrams. For instance, the polar angle of 0° (180°) corresponds to the polarization along SA of the NCs, while the polar angle of 90° (270°) indicates the polarization along LA. The measured value is the SH amplitude along SA (top row) and along LA (bottom row). The pumping wavelengths of the incident light are at 1250, 1300, 1380, and 1550 nm for NC1 since they cover LA dipole resonance band for NC1. A similar idea

is used for Fig. 13b. The values of the pumping wavelengths of 1280 nm, 1400 nm, and 1540 nm represent the region of SA resonance for NC2. Blue arrows indicate the polarization direction of detected SH signals. Black dots represent experimental data acquired with the polarization angle varying from 0° to 360° with a step of 10°. Fitting results using equation (4.11) are overlaid in the polar plots as red solid lines. It is clear that the SH signal strongly depends on the pumping frequency of the incident pulse and its polarization.
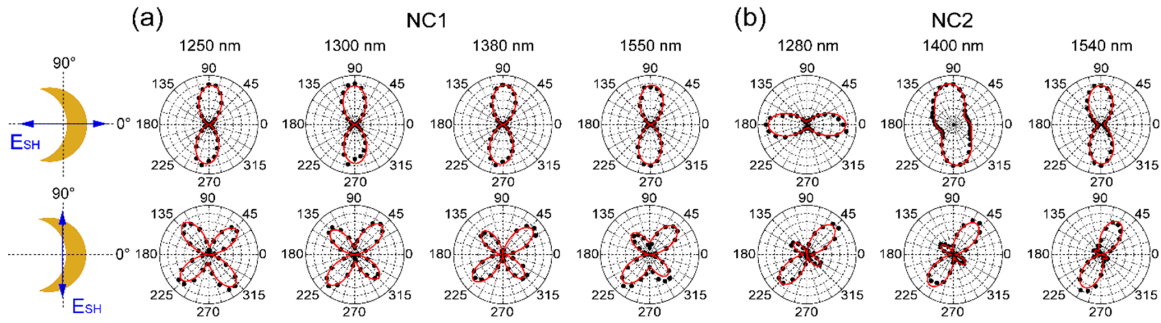
Figure 13. Incident Polarization Angle Dependence of SH Signals of NCs (experimental data)
Note: Measured for NC1 (a) and NC2 (b).

The two-lobe pattern presents on all SH intensities along SA of NC1 (Fig. 13a, top). When the incident polarization is along SA, the intensity is the weakest. Moving towards the polarization along LA, the intensity is increasing. So, when the polarization is along LA, it is two orders bigger than it is for SA. The four-lobe patterns are seen when the polarization is traced along 90° (Fig. 13a, bottom). Their presence and asymmetry suggest that the used macroscopic formalism can't adequately describe the SH response of the plasmonic NC emitters. The asymmetry becomes more noticeable for NC2 (Fig. 13b). A two-lobe pattern is oriented along SA at the incident wavelength of 1280 nm, indicating that the SH intensity became strongest (weakest) for the horizontally (vertically) polarized excitation light. There are two clean lobes at 1280 and 1540 nm, and one more at 1400 nm, significantly distorted. Noticeable asymmetry problems appear for the SH polarized along LA. Amplitudes of the diagonal and antidiagonal lobes are different

(Fig. 13b, bottom). The ratio of antidiagonal to diagonal lobe size decreases with increasing the excitation wavelength. Also, the orientation of the larger two-lobe changes from 45° at 1280 nm to 60° at 1540 nm.

To have a better fit for the observed polarization, (4.11) could be used over (4.10). Resultant fitting coefficients $\xi_{ijk}^{(2)}$ for the different polarization components are shown in Fig. 13. To reproduce the incident polarization angle dependence of SH signals in Fig. 13, fitting coefficients $\xi_{ijk}^{(2)}$ from equation (4.11) are used. The polarization direction of the detected SH signals is along SA (top) or LA (bottom). Polarization components, ijk, are indicated by the labels. Polarization components that are allowed under the dipole approximation for C_{1h} symmetry are marked with rectangular boxes.
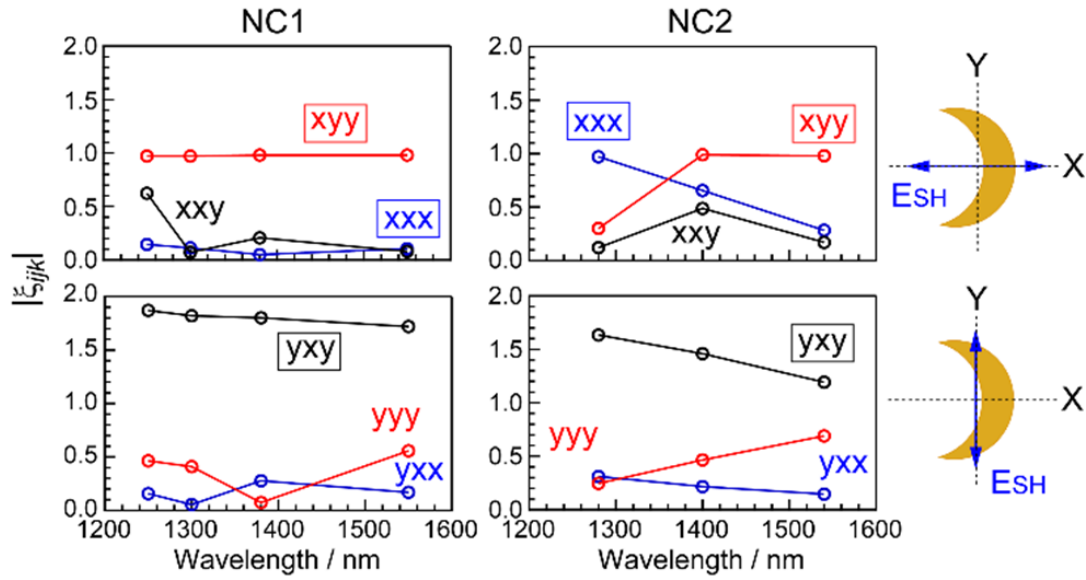

Figure 14. Fitting Coefficients $\xi_{ijk}^{(2)}$ from Equation (4.11)

The main impact for the SH polarized along SA of NC1 comes from the *xyy* term with tiny contributions from *xxx* and *xxy*. The same behavior is for the SH intensity along SA of NC2, only at 1540 nm. The contribution of *xxx* increases with decreasing the wavelength, and at 1280

nm it almost exclusively dominates the observed SH response. The four-lobe patterns, acquired for the SH intensity along LA, are mainly caused by the dipole-allowed *yxy* component. The other two dipole forbidden terms, *yyy* and *yxx*, distort the symmetry of the four-lobe pattern, and their contributions depend on the incident light wavelength. The fitting results suggest that dipole allowed polarization tensors are the main contributors to the SH response for both samples. However, dipole forbidden components for C_{1h} symmetry are also important, especially for the SH intensity along LA. The observed pattern for NC2 at 1540 nm (Fig. 13b) may be a manifestation of this transition between a four-lobe and two-lobe pattern, and the SH intensity is strongest at 60°.

Another possible reason for the asymmetric four-lobe patterns may be related to a marginally distorted NC shape as discussed below with numerical results.
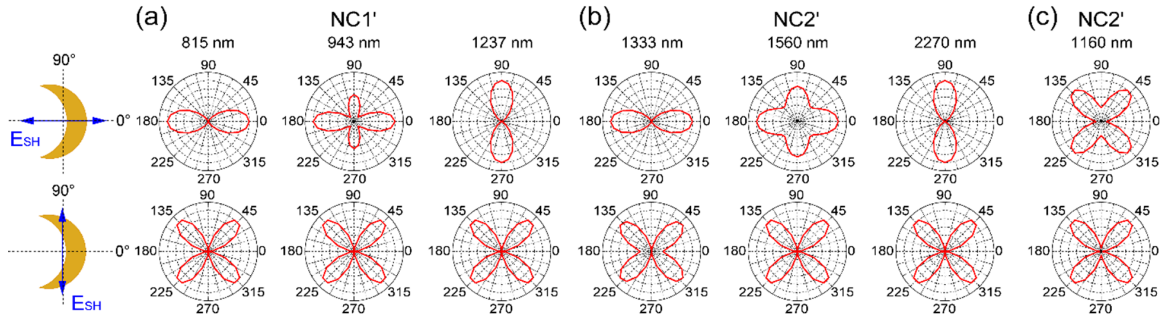
Figure 15. Incident Polarization Angle Dependence of SH Signals of NCs (simulations)

Note: Measured for NC1 (a) and NC2 (b).

Several additional simulations are performed for both NC1′ and NC2′ at different pump wavelengths. The results are shown in Fig. 15a, b, where the characteristic wavelengths are examined: the peak wavelengths of SA/LA mode and the wavelength at which linear absorbance calculated for the incident polarization along SA and LA intersect (Fig. 12c, d). Firstly, the SH signal polarized along LA has four lobes as in the experiments. Secondly, as expected, SA polarized signal is oriented either along SA or LA, depending on which plasmonic mode is dom-

inant at a given pump wavelength. These results reproduce the expected angular properties of SH as obtained from the second-order nonlinear polarization in equation (4.10). Thirdly, the four-lobe pattern oriented along SA and LA is seen for both NC1′ and NC2′ at wavelengths for which both plasmonic modes are being pumped (943 nm for NC1′ and 1560 nm for NC2′). This shows which component of the corresponding second-order susceptibility tensor is larger. Although the model qualitatively describes angular properties of the observed results, one important piece is still missing, namely, the experimental angular diagrams show clear asymmetry of LA polarized SH signal (Fig. 13).

4.2.2 Effect of Broken Symmetry on Second Harmonic

In using nanosphere template lithography to fabricate an NC array, not every structure is perfectly symmetric. A distorted structure breaks the symmetry, which makes the incident polarization angle dependence of SH not theoretically reproduced by equation (4.10). Also, the fitted coefficients of (4.11) would have no clear physical meaning in that case because their relationships with the structural distortion cannot be straightforwardly predicted. The advantage of the used model is that it allows to further investigate how the SH response is sensitive to the symmetry of NCs.

Two possible scenarios are considered that may alter the symmetric angular patterns seen in Fig. 15 to become asymmetric. Schematic setups that have been investigated are shown in Fig. 17a, b. Two ways how mirror symmetry could be broken are considered. Firstly, the NC is rotated counterclockwise by a small angle θ and the surface of the NC is altered by adding extra pixels. In Fig. 17a, blue and red colors correspond to pixels added to the upper and lower parts of the particle in a non-symmetric fashion (each pixel does not have its mirror image on the other side of the dashed line). It is important to emphasize that the described extra-pixelization may alter
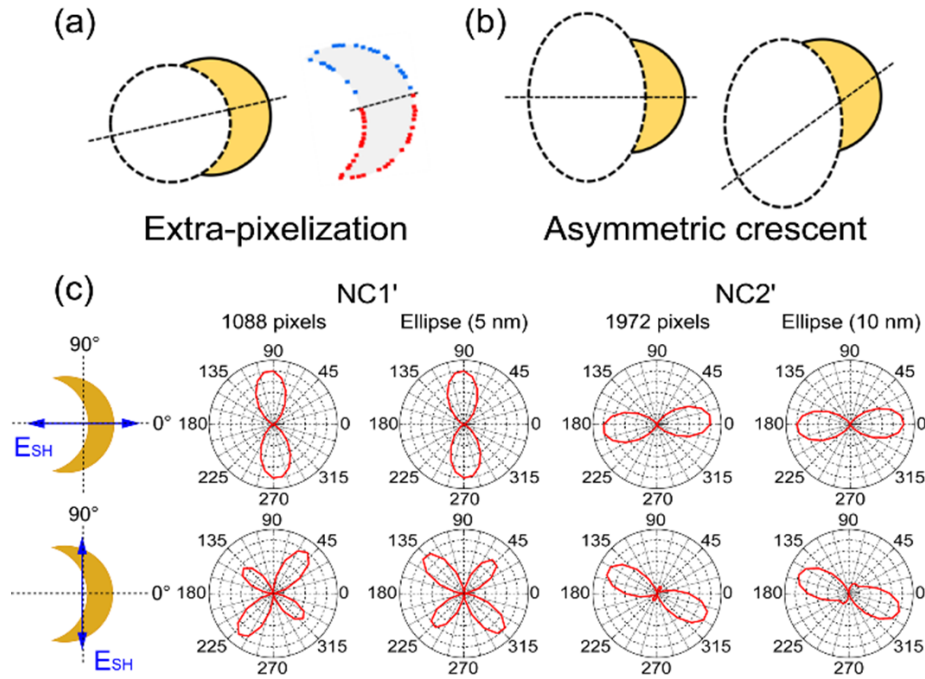
Figure 16. Broken Symmetry of NCs

Note: Schematic setup of extra-pixelization (a); schematic setup of asymmetrization (b); incident polarization angle dependence of SH signals (c).

the volume of the particle if the total number of pixels is large, which in turn affects plasmonic properties. On the other hand, it should be ensured that numerical convergence is achieved, i.e., when adding a few pixels, one should not observe any changes in the SHG signal. Thus, a delicate balance needs to be found, in which, on one hand, the volume of the particle does not significantly depart from the volume that the symmetric particle has, and also the surface is altered just enough to observe breaking of the mirror symmetry. After extensive numerical tests, it was found that the angular properties of SHG noticeably change for the total number of extra-pixels exceeding 1000 for the spatial resolution of 1.5 nm.

Secondly, in order to break the mirror symmetry of the crescent, an ellipse superimposed on a circle (rather than a circle on a circle) is used, as depicted in Fig. 16b. In this case, when the ellipse

is shifted, the resulting crescent does not longer maintain mirror symmetry. When the ellipse is moved down, the crescent becomes thicker at the top and thinner below the dashed line.

The results of both approaches that break the mirror symmetry are summarized in Fig. 16c. The obtained angular diagrams qualitatively show similar patterns to the ones seen experimentally with highly non-symmetric LA polarized SH signals (see Fig. 13b). The total number of extra pixels added to NC1$'$ and NC2$'$ in Fig. 16c is 1088 and 1972, correspondingly. There are two important observations:

1. The SA polarized signal rotates exactly by θ although maintains symmetric two-lobe patterns;

2. The LA polarized signal is significantly altered by the symmetry breaking.

The observed asymmetry in LA polarized SH signals for NC1$'$ shows another feature – two smaller lobes become shorter when the upper part of the non-symmetric crescent has less extra-pixels, compared to the lower part. Also, extra-pixelization that alters the surface of the nanocrescent making it non-mirror symmetric can also explain which of the four lobes in LA SH become shorter/longer. For the calculations NC1$'$ has total of 1088 extra pixels (731 pixels at the outer surface and 357 pixels at the inner surface 357), as shown in Fig. 16c. However, when the symmetry is broken using the ellipse-on-circle procedure, the four-lobe pattern exhibits completely opposite behavior. This occurs because the resulting NC has a thicker upper part. Even more noticeable changes occur for the NC2$'$ geometry, where the symmetry breaking influences the angular properties of SHG while pumping SA plasmonic mode. The four-lobe pattern exhibits remarkable transformations with two lobes being nearly completely gone.

4.2.3 Wavelength Dependence of Second Harmonic Response

Fig. 17 shows measured and calculated excitation wavelength dependence of SH signals of Au NC array. Open circles and squares in Fig. 17a show integrated spectral intensity of NC1 and NC2, respectively, normalized with that of z-cut quartz. The polarization direction of the excitation pulse and the SH signal is indicated by a red and a blue arrow. Blue and red lines represent the absorbance spectra measured with the incident light polarized along LA and SA of NCs, respectively. In Fig. 17b, the same SH data set is plotted against one-half of the incident wavelength together with the absorbance spectra. The top panel of Fig. 17c shows results of NC1′ calculated with the pump polarized along LA and SH signal polarized along SA (blue circles). In the same panel linear absorbance is plotted, where the red line indicates absorbance obtained when the excitation is polarized along LA, and the blue line with the incident field polarized along SA. The bottom panel of Fig. 17c shows the data for NC2′ obtained with the pump polarized along SA. Both polarizations of SHG are plotted (SA is shown as blue squares, and LA is shown as red squares after multiplying by 10). In Fig. 17d, the same data set is plotted against one-half of the incident wavelength together with the calculated absorbance spectra.

The wavelength dependence of the SH light intensity does not follow the spectral shapes of the dipole localized SPRs resonances of Au NC. For NC1, the SH intensity exhibits a dip at around 1275 nm, and the maximum response occurs at ~ 1375 nm. For NC2, the SH intensity monotonically increases with decreasing the incident wavelength with a small bump at 1425 nm.

To elucidate the effects of higher-order plasmon resonances on the SH enhancement, it is useful to compare the excitation wavelength dependence of SH on plasmon band shapes at half of the incident wavelength. Fig. 17b shows the SH intensities together with the absorbance spectra in the wavelength range from 400 to 1000 nm. For NC1, the dependence is quite different from the absorbance spectrum observed with the light polarized along SA (blue curve) in this
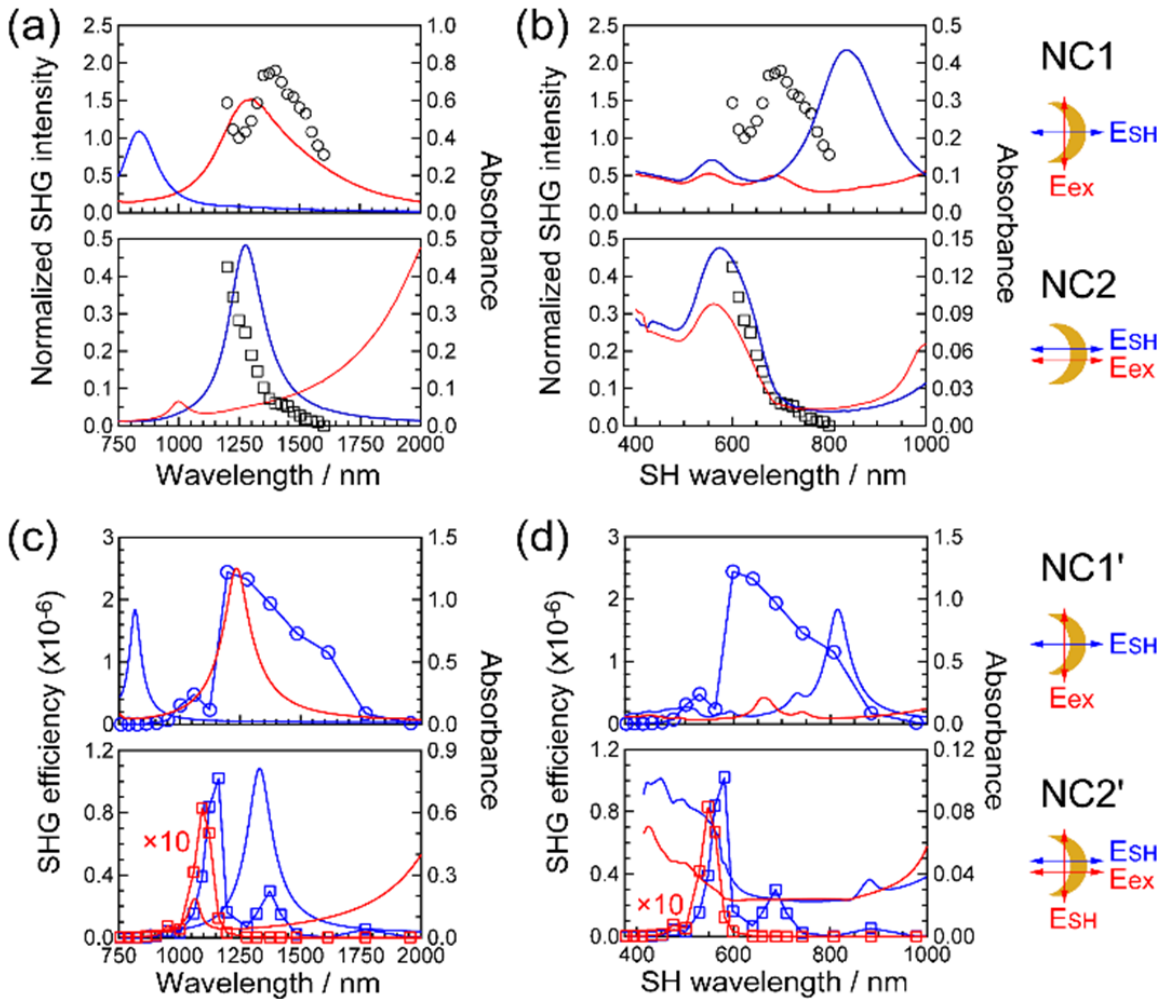
Figure 17. Experimental and Calculated Excitation Wavelength Dependence of SH Signals of of NCs

wavelength range, but it shows a similar trace to the 'merged' shape of LA dipolar band (red curve in Fig. 16a) and the dipole and multipole band (blue curve in Fig. 16b). Fig. 17c exhibits the calculated SHG efficiency of NC1′ and NC2′ as a function of the pump wavelength. Blue circles (top) show the result for SA polarized SH signal when the NC1′ nanocrescent is pumped along its LA. Here SHG efficiency and linear absorbance (blue and red lines) are plotted as functions of the incident wavelength. The SH response peaks at LA plasmon mode at 1237 nm (Fig. 17c), indicating that the dipole plasmon is a major reason for enhancing SH efficiency. At the same

time, the SH response is broad and intense in the wavelength range > 1237 nm. It appears that both SA dipolar band (blue in Fig. 17d) and LA quadrupolar/multipolar bands (red in Fig. 17d) can contribute to enhancing SH response in this range. More interesting results are obtained for NC2′ (bottom). The system is excited along SA direction and the SH efficiency along the same axis is plotted (blue squares). Additionally, the linear absorbance calculated for SA and LA polarized incident pump is overlapped in the same panel. Firstly, one can notice that SA polarized SH has one extremum near the peak wavelength of the corresponding dipole plasmon resonance. Secondly, one can see that the efficiency curve has a remarkably strong extremum at ~ 1160 nm. Although it is near the peak of LA quadrupole resonance (1065 nm), one does not expect LA quadrupole band to contribute to the enhancement because the incident light is polarized along SA. Further observation shows that this SH peak is at the edge of a broad multipole resonance, as shown in Fig. 17d. The shape of the SH trace is similar to the merged shape of SA dipolar band (blue curve in Fig. 17c) and the broad multipole band (blue curve in Fig. 17d).

The results of the numerical calculation indicate that the SHG efficiency is affected not only by the field enhancement at the fundamental wavelength, but also at the SH wavelength. Depending on the size of the nanocrescent and the excitation wavelength, different localized SPRs will couple with the induced SH field and render additional enhancement of signal intensity. For example, in the case of NC2′, the highest SHG efficiency is obtained at ~ 1160 nm, which is about 170 nm off from the peak of SA dipole resonance. To further demonstrate that the multipole plasmon enhances the SHG at 1160 nm, the simulations for NC2′ were performed by pumping the nanocrescent at 1160 nm and varying the in-plane incident field polarization. The results are shown in Fig. 15c where a four-lobe pattern is observed for SA polarized SHG. This pattern indicates that $P_x^{(2)}(\omega) \sim \xi_{xxy}^{(2)} sin\theta cos\theta$ and $\xi_{xxy}^{(2)}$ is non-zero at this wavelength. This tensor element is dipole forbidden. Hence, the multipole localized SPR at the SH wavelength has enhanced the induced field. The calculated multipole localized SPR for NC2′ has a very broad line shape below

600 nm. However, the field enhancement by SA dipole resonance is much weaker for the fundamental light below 1000 nm, so the SHG efficiency would not monotonically increase at shorter wavelengths. To further illustrate the effects of higher-order localized SPR, the SH efficiency of NC2′ was calculated along LA (red squares in Fig. 17c, d). The efficiency of LA polarized SH is about 10 times lower than that of SA polarized SH because LA multipole is much weaker than SA multipole resonance. The peak of LA polarized SH is red-shifted from that of SA polarized SH toward LA quadrupole band at 1065 nm, suggesting the contribution of LA quadrupole band to SHG.

Summarizing the results, experimental and theoretical measurements of the wavelength and polarization dependent SH responses of two different Au NCs were conducted. It is shown that the incident polarization angle dependence of SH signals is strongly sensitive to nanoscale variations in the NC's shape.

4.3   Fano Resonances
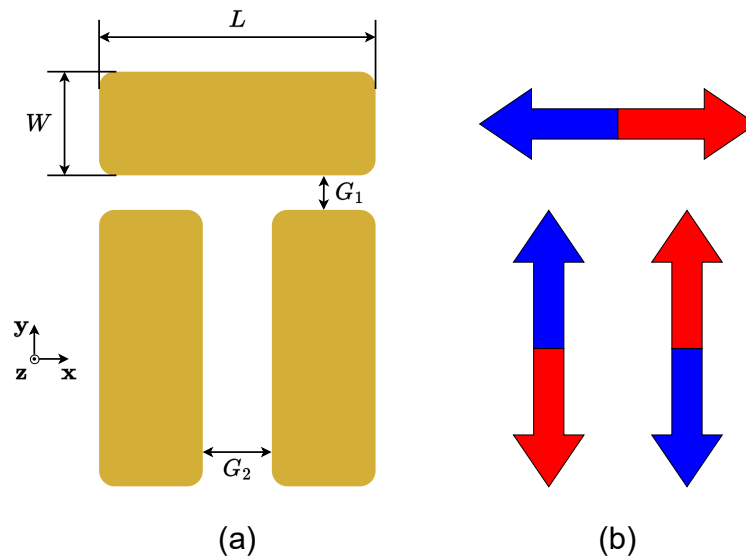
Figure 18. Schematic Setup of a Nanodolmen Structure

Another system to investigate the behavior of SH is a nanodolmen. It consists of three gold nanorods positioned in the way it is shown at Fig. 18a. G_1 represents the distance between the top nanorod and two bottom ones. G_2 shows how two bottom parallel nanorods are far away from each other. The light polarized along x-axis and under normal incidence excites the longitudinal mode of the horizontal nanorod (see Fig. 18b). It is also called 'bright' mode since it was excited directly from the incident pulse. On the opposite side, the bottom two nanorods exhibit a dark mode since they have oscillations of the conduction electrons out-of-phase. The geometry matters a lot since the strengths of the coupling change if G_1 and G_2 are shifted. The following parameters are used to simulate gold: the equilibrium number density of conduction electrons $n_0 = 5.9 \times 10^{28}$ m^{-3}, Fermi energy $E_F = 5.53$ eV, effective electron mass $m^* = 1.66 \times m_e$, and the phenomenological decay constant $\gamma = 0.181$ eV.

Here the SH is under investigation one more time. Also, the influence of Fano-type modes generated by the nanodolmens on the SH is discussed. The resonances are called 'Fano resonances' because of their non-symmetric shape arising from scattering.

Figure 19. Linear Optical Properties of a Periodic Array of Nanodolmens

Note: Linear absorption spectra for different values of G_1 (a); absorption spectra for different values of G_2 (b).

56

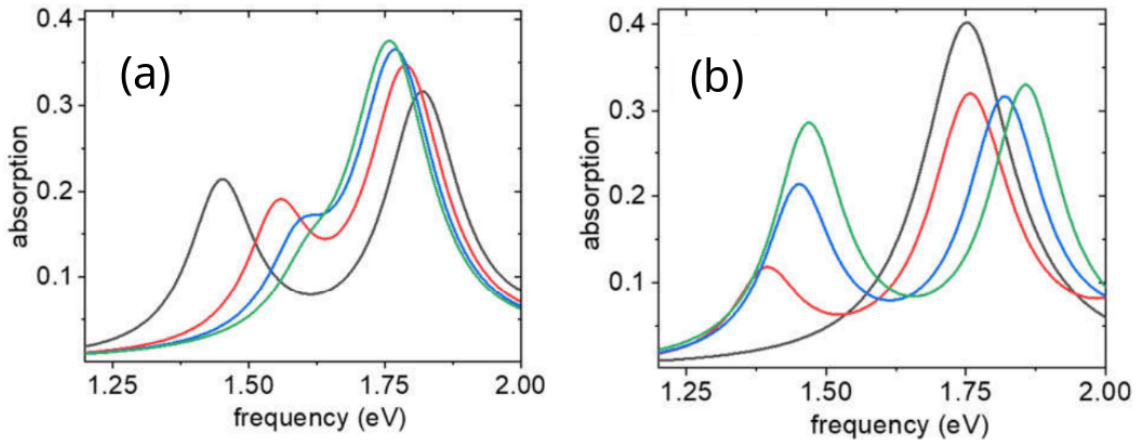Fig. 19a shows linear absorption spectra when varying gap G_1: 15 nm (black line), 30 nm (red line), 45 nm (blue line), and 60 nm (green line). Parameter G_2 is fixed at 30 nm. Fig. 19b depicts absorption spectra for different G_2: only horizontal nanorod is considered (black line), 15 nm (red line), 30 nm (blue line), and 60 nm (green line). G_1 is fixed at 15 nm. The rest of the parameters for Fig. 19a, b are: periodicity is 405 nm, $W = 40$ nm, $L = 110$ nm, and thickness of each nanorod is 60 nm.

Standalone nanorod has a resonance around 1.75 eV (see black line, Fig. 19b). And with two parallel nanorods, two peaks in the spectrum appear. The investigation of the linear regime is based on the adjustment of the parameters G_1 and G_2 and the observation of how it changes the coupling of the bright and the dark mode. Looking closer at Fig. 19a, one can see that changes in G_1 values show how the near-field coupling weakens at larger values of G_1. When $G_1 = 15$ nm (black line) and $G_1 = 30$ nm (red line), there is a clear splitting. But the bigger the distance between the nanorods, the smaller the coupling (drops by over 60%). The changes are even more dramatic for $G_1 = 45$ nm (blue line) and $G_1 = 60$ nm (green line). The second peak is barely pronounced on the blue line and disappears for the green line completely. A similar investigation is conducted when parameter G_2 is varying and G_1 is fixed. Here G_2 controls the frequency of the dark mode and its linewidth. Contrary to increasing G_1, higher values of the gap between two parallel wires increase the splitting between the observed modes and enhance the signal at the low frequency normal mode.

4.3.1   Nonlinear Regime

To investigate the nonlinear response, the system is pumped with a high intense pulse (amplitude is 0.05 V/nm and the duration is 500 fs). The outgoing electromagnetic flux is detected at the doubled pumped frequency (SH). From it, the second-order susceptibility can be calculated

(more details regarding the calculations are available in 4.1.1):

$$\chi^{(2)} = \frac{\beta}{2V},$$

(4.12)

where V is the volume of the nanodolmen and β is the hyperpolarizability per unit cell.
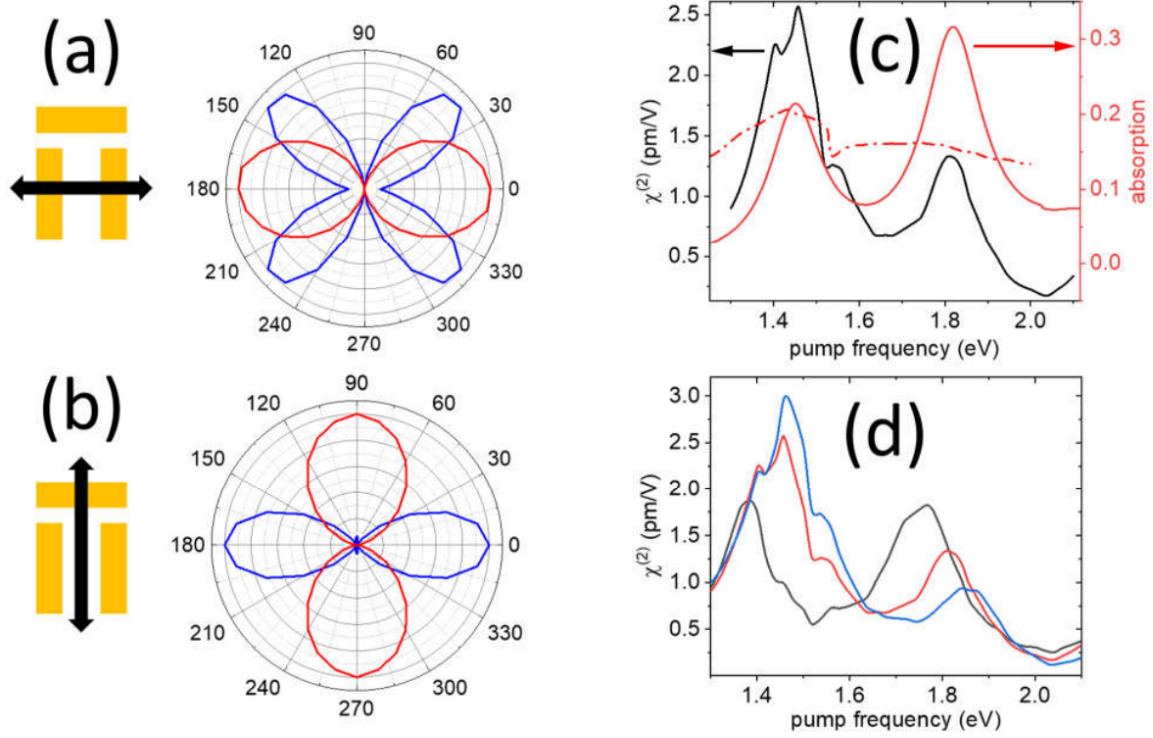
Figure 20. SHG of Nanodolmens

Note: Angular diagrams of SH signal polarized horizontally (a) and vertically (b) at the pumped frequency of 1.45 eV (blue lines) and at 1.82 eV (red lines); second-order susceptibility (black line), linear absorption (solid red line), and absorption plotted at half the frequency (dash-dotted red line) (c); second-order susceptibility for different values of G_2 (d).

First, the angular distributions of the SH signal are investigated. As it was done for the previous case (for NCs), horizontal and vertical components of the macroscopic polarization are separated and results are presented at Fig. 20a, b. Simulations are performed for the nanodolmen with G_1 = 15 nm and G_2 = 30 nm with the other parameters, as it is indicated in Fig. 18. Blue lines show results obtained at the pumped frequency of 1.45 eV. It corresponds to the antisymmetric normal mode. Red lines show data for the driving frequency 1.82 eV, which is the

symmetric normal mode. The angle on the polar diagrams indicates the polarization of the incident pulse: $0°$ corresponds to the pump polarized along the upper nanorod or along x-axis. If the system is pumped at 1.45 eV, the following behavior is expected from the SH:

$$P_x^{(2)} \sim \chi_{xxy}^{(2)} sin(2\theta),$$
$$P_y^{(2)} \sim \chi_{yxx}^{(2)} cos^2(\theta),$$

(4.13)

where the off-diagonal elements $\chi_{xxy}^{(2)}$ and $\chi_{yxx}^{(2)}$ impact the SHG the most. In other words, the dark mode contributes a lot at the chosen frequency since it mixes the x and y polarizations.

If the system is pumped at 1.82 eV, the following dependencies are expected:

$$P_x^{(2)} \sim \chi_{xxx}^{(2)} cos^2(\theta),$$
$$P_y^{(2)} \sim \chi_{yxx}^{(2)} sin^2(\theta).$$

(4.14)

In this case, the diagonal elements dominate more in the SH signal.

Moving on to the next set of pictures at Fig. 20. Here the second-order susceptibility is under the scope. Fig. 20c compares the second-order susceptibility (black line) with a linear absorption (red line). The same absorption is plotted by the dash-dotted line, but at half the frequency, to explore two-photon processes due to the high frequency modes. Firstly, the shift between peaks of the second-order susceptibility and the linear response is noticeable: 1.82 eV for $\chi^{(2)}$ and 1.75 eV for the absorption. Secondly, resonances at 1.4 eV and 1.53 eV exhibited by $\chi^{(2)}$ are due to the SH contributions from the high energy quadrupole mode and Wood's anomaly corresponding to the periodicity of the nanodolmen array. The period used in the simulations is 405 nm or frequency-wise it is 2 × 1.53 eV.

To see the change in $\chi^{(2)}$ behavior under different strength of coupling of the bright and dark modes, parameter G_2 is varied (see Fig. 20d). There are three distances between the vertical nanorods considered: G_2 = 15 nm (black line), G_2 = 30 nm (red line), and G_2 = 60 nm (blue line). The closer the nanorods are, the more increase of the intensity for the lower frequency and

the more suppression for the higher frequency. It can be explained by lower dissipation at the lower frequencies. Also, the local field enhancement for such a mode can reach several orders of magnitude, which in turn leads to more efficient SHG (Gallinet and Martin 2011).

4.3.2 Analytical Model of Two Coupled Nonlinear Oscillators

It is also useful to have a straight analogy between the second-order nonlinear response from a Fano type nonlinear plasmonic system and two coupled oscillators.
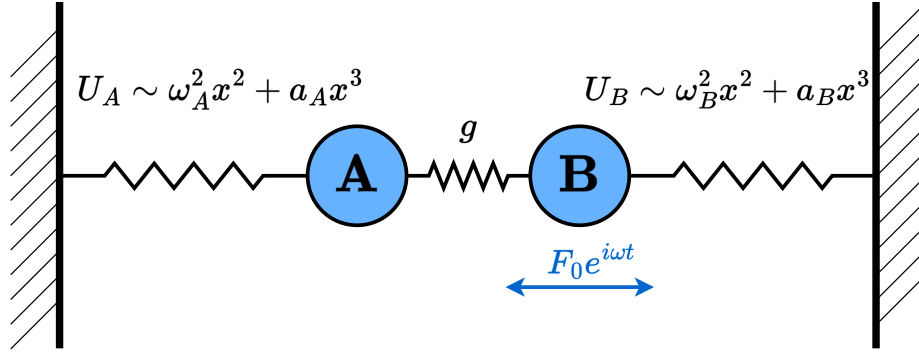
Figure 21. Two Coupled Nonlinear Oscillators

The toy model is sketched in Fig. 21. Each oscillator has a second-order nonlinearity. Also, oscillator A is coupled to B which is directly driven by the external force F_0. Both oscillators have a third-order nonlinearity in potential energy $U_{A,B}$ (i.e., the second-order in the corresponding restoring force). The equations of motion can be written as:

$$\ddot{x}_A + \gamma_A \dot{x}_A + \omega_A^2 x_A + \alpha_A x_A^2 + g^2 x_B = 0,$$

$$\ddot{x}_B + \gamma_B \dot{x}_B + \omega_B^2 x_B + \alpha_B x_B^2 + g^2 x_A = F_0 e^{i\omega t},$$

(4.15)

where g is the coupling coefficient that indicates the strength of coupling between A and B oscillators, $\alpha_{A,B}$ are the parameters that characterize the strength of nonlinearity. Here oscillator A is the dark mode (with a higher frequency and lower damping rate) and oscillator B is the bright mode corresponding to the longitudinal plasmon mode of the top nanorod.

Using the solution of equations (4.15) in the form of a perturbation series $x_{A,B} = \sum_n x_{A,B}^{(n)}$ and equating the same perturbation orders, one can obtain a set of coupled differential equations:

$$\ddot{x}_A^{(1)} + \gamma_A \dot{x}_A^{(1)} + \omega^2 x_A^{(1)} + g^2 x_B^{(1)} = 0,$$

$$\ddot{x}_B^{(1)} + \gamma_B \dot{x}_B^{(1)} + \omega^2 x_B^{(1)} + g^2 x_A^{(1)} = F_0 e^{i\omega t},$$

$$\ddot{x}_A^{(1)} + \gamma_A \dot{x}_A^{(1)} + \omega^2 x_A^{(1)} + \alpha_A (x_A^{(1)})^2 + g^2 x_B^{(1)} = 0, \qquad (4.16)$$

$$\ddot{x}_B^{(1)} + \gamma_B \dot{x}_B^{(1)} + \omega^2 x_B^{(1)} + \alpha_B (x_B^{(1)})^2 + g^2 x_A^{(1)} = 0,$$

...

Solution of equations (4.16) corresponding to the linear case (i.e., at the fundamental frequency of the driven force) can be obtained by substituting $x^{(1)} \rightarrow x^{(1)} e^{i\omega t}$ and equating terms with $e^{i\omega t}$:

$$x_A^{(1)} = \frac{g^2}{g^4 - D_A(\omega) D_B(\omega)} F_0,$$

$$x_B^{(1)} = -\frac{D_A(\omega)}{g^4 - D_A(\omega) D_B(\omega)} F_0, \qquad (4.17)$$

where $D_A(\omega) = \omega_A^2 - \omega^2 + i\gamma_A \omega$ and $D_B(\omega) = \omega_B^2 - \omega^2 + i\gamma_B \omega$. The assumption $\gamma_B \gg \gamma_A$ that is the driven oscillator B has a higher rate of dissipation than oscillator A, gives rise to the Fano-like resonances. It can be explained by the interference between the direct excitation of oscillator B being the driving force and the excitation of oscillator B via coupling through oscillator A.

Fig. 22a shows $\left| x_B^{(1)} \right|^2$ as a function of the pumping frequency for different coupling coefficients: $g = 0.3$ eV (black line), $g = 0.5$ eV (red line), and $g = 0.7$ eV (blue line). The higher the values of g, the more shape of the Fano-like resonances is pronounced. When $g > \gamma_A$, two normal modes (arising from the symmetric and antisymmetric combinations of $x_A^{(1)}$ and $x_B^{(1)}$) are formed at the following frequency:

$$\Omega_\pm = \left(\frac{\omega_A^2 + \omega_B^2 + \gamma_A \gamma_B}{2} \mp \frac{1}{2}\sqrt{4g^4 + (\omega_A^2 - \omega_B^2)^2 + 2\gamma_A\gamma_B(\omega_A^2 + \omega_B^2) + \gamma_A^2\gamma_B^2} \right)^{1/2}. \qquad (4.18)$$
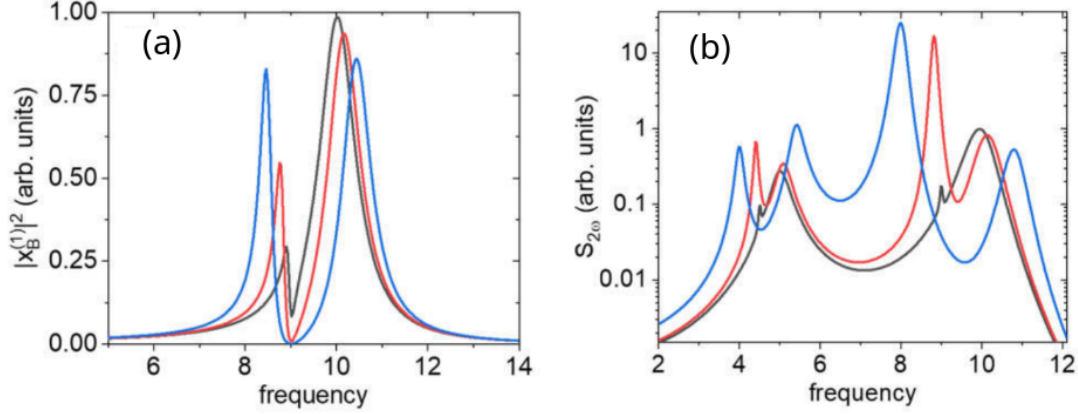
Figure 22. Analytical Solution for Two Coupled Oscillators

Note: First-order signal by oscillator B (a); second-order signal for different values of the coupling strength g (b).

The second-order displacement oscillates at the SH of the driving force. Substituting $x^{(2)} \rightarrow$ $x^{(2)} e^{i\omega t}$ and inserting (4.17) into (4.16) give:

$$x_A^{(2)}(2\omega) = \frac{\alpha_A g^4 D_B(2\omega) - \alpha_B g^2 D_A^2(\omega)}{\left(g^4 - D_A(\omega)D_B(\omega)\right)^2 \left(g^4 - D_A(2\omega)D_B(2\omega)\right)} F_0^2,$$
$$x_B^{(2)}(2\omega) = \frac{\alpha_B D_A^2(\omega)D_A(2\omega) - g^6 \alpha_A}{\left(g^4 - D_A(\omega)D_B(\omega)\right)^2 \left(g^4 - D_A(2\omega)D_B(2\omega)\right)} F_0^2.$$

(4.19)

Second-order solution (4.19) has two distinct contributions from one-, $D(\omega)$, and two-photon, $D(2\omega)$, emission.

In other words, the emission signal from the coupled oscillators A and B can be written as:

$$S_{2\omega} \sim \left| x_A^{(2)}(2\omega) \right|^2 + \left| x_B^{(2)}(2\omega) \right|^2,$$

(4.20)

since the prime interest is to investigate the SH.

Fig. 22b shows the dependence of the second-order signal $S_{2\omega}$ on the pump frequency for three different values of the coupling coefficient: $g = 0.3$ eV (black line), $g = 0.5$ eV (red line), and $g = 0.7$ eV (blue line). It is interesting to note that each peak in case $g = 0$ splits into two peaks. The antisymmetric mode Ω_- results in a significant enhancement of the SH response,

while the contribution to $S_{2\omega}$ by the symmetric mode Ω_+ becomes weaker with an increased coupling. Since oscillator A has considerably lower losses compared to B, it can store higher amounts of energy, which in turn leads to stronger emission.

The proposed analytical model of coupled nonlinear oscillators predicts a noticeable enhancement of the second-order response at the frequency of the antisymmetric mode and the suppression of the signal by the symmetric mode. The primary source of the enhancement and suppression is the sub/superradiant nature of the normal modes of coupled oscillators.

Summarizing the computational results, the conducted simulations are also in close agreement with the main prediction – the SHG process driven at the frequency corresponding to a narrow resonant mode with a Fano-like profile leads to the strong enhancement of the nonlinear response. The behavior of the SH signal generated by an individual nanodolmen is also analyzed. It is shown that the angular properties of the SH are very sensitive to changes in the initial geometrical parameters. The nonlinear signal enhancement due to local field enhancement is less pronounceable, but it is still observed.

Chapter 5

STUDIES OF THE STRONG COUPLING

Two examples of strong coupling between two nonlinear interfaces are discussed here. The first work is done for 2D materials, where the silver wires are coupled to WS_2. The second work focuses on the triangular nanoholes that are coupled to molecules. The noticeable Rabi splitting is shown for both cases and the nature of the observed phenomenon is discussed.

5.1 Harmonic Generation by Metal Nanostructures Strongly Coupled to Few-Layer Thin Transition Metal Dichalcogenides

Transition Metal Dichalcogenides (TMDs) are 2D materials. They have been investigated for nonlinear optical applications, including broadband optical devices, nonlinear frequency conversion processes, mid-infrared photonics, and THz sources and detectors (Autere et al. 2018). Tungsten disulfide (WS_2) is chosen here as a model compound for a few-layer 2D-material. The nonlinear optical response of WS_2 with both second- and third-order susceptibilities coupled to a periodic plasmonic grating is shown to have a significant effect on the SHG of the metal. To achieve the strong coupling regime, the combination of excitons supported by WS_2 and SPPs supported by 2D periodic plasmonic interfaces is considered. It is shown how the exciton-plasmon strong coupling influences the nonlinear optical responses of hybrid nanomaterials in 2D.

The plasmonic system consists of a flat metal film of thickness d placed on the glass substrate and metal wires of the width R_x and the height R_y on top of the flat metal film (see Fig. 23a). To avoid lightning rod effects due to sharp corners, smooth corners of the wire with the curvature R
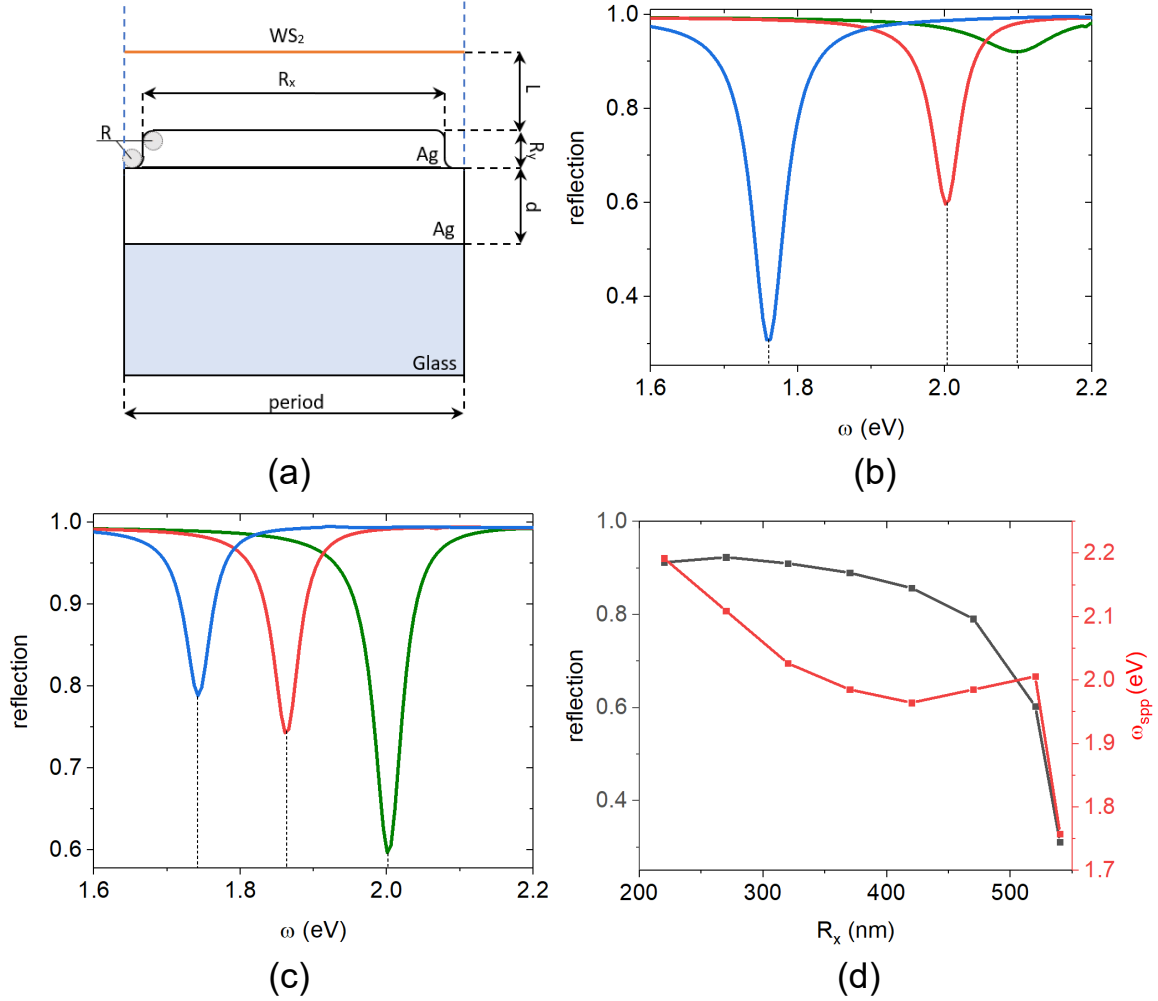
Figure 23. Linear Optics of the Metal Nanostructure

Note: Schematic setup (a); reflection spectra without WS_2 for different values of the R_x (b); reflection spectra without WS_2 for different values of the period (c); reflection coefficient evaluated at the corresponding plasmon frequency (black line) and the value of the plasmon frequency in eV (red line) (d).

are used. The nonlinear material is placed on the input side at a distance L above the metal wire. In all simulations the thickness of the silver film, d, is 100 nm, wire's height, R_y, is 50 nm, and the curvature of the corners, R, is 10 nm.

The electrodynamics of the plasmonic system under consideration is simulated by numerically integrating Maxwell's equations (2.1). To account for the nonlinear optical response of

metal the classical theory based on the nonlinear Drude model (2.31) was adopted and coupled to (2.1). For silver, the following parameters are used: plasma frequency Ω_p = 9.04 eV and the phenomenological decay constant γ = 0.02125 eV.

When investigating the dynamics of plasmons coupled to a thin dispersive material (schematically depicted as WS_2 at Fig.23a), the latter is described by the linear Lorentz dielectric function with experimental parameters corresponding to a few-layer thin WS_2. The nonlinear part of the response is simulated by adding second- and third-order susceptibilities, $\chi^{(2)}$ and $\chi^{(3)}$, correspondingly, and implementing the efficient numerical procedure, allowing to account for both linear dispersion and the nonlinear effects.

Fig. 23 explores the main linear optical properties of the periodic plasmonic grating. Fig. 23b, c show the reflection spectra of the system without WS_2 as a function of the incident photon energy. In Fig. 23b different colors correspond to different values of wire's width R_x keeping other parameters constant. The period is set at 550 nm. The blue line corresponds to R_x = 540 nm, the red line is for R_x = 520 nm, and the green line is for R_x = 270 nm. In Fig. 23c different colors correspond to different values of the period and R_x = 520 nm. The blue line is for the period of 650 nm, the red line corresponds to the period of 600 nm, and the green line is for the period of 550 nm. The SPP mode is seen because the low energy minimum highly dependent on the width of metal wires (Fig. 23b) and the periodicity (Fig. 23c). When the value R_x is close to the period, the reflection reaches nearly 35%, making the coupling of the incident light to the plasmon mode very efficient. One may use R_x as a tuning knob to adjust the position of the mode to the desired frequency, making it very useful when trying to couple it to another optical oscillator, such as a molecular aggregate or a 2D material.

One can see from Fig. 23b that increasing R_x results in the red shift of the plasmon resonance with the reflection going from merely 90% to 35%. For a fixed value of R_x, decreasing the period

leads to a predictable blue shift of the mode, as shown in Fig. 23c. The efficiency of the coupling to the plasmon mode also varies with both the period and wire's width.

Fig. 23d shows the dependence of the reflection (black line) and the corresponding plasmon frequency (red line) on R_x for the period of 550 nm. For the large values of R_x (i.e., small gaps between wires) the plasmon mode becomes highly spatially localized near/inside the gaps between wires. Although the reflection becomes significantly small, such localization is not desirable since the goal is to be able to couple the plasmon mode to a 2D material placed in proximity of the wires. Thus, R_x is kept large enough for the incident field to couple to the plasmon, but small enough, so the plasmon mode spatially extends to about 15-50 nm above wire's surface.

5.1.1   Nonlinear Regime of the Metal Nanostructure

Fig. 24 summarizes the nonlinear response of a bare plasmonic system without 2D material. Here the dependencies of the SH and third harmonic (TH) are explored on various geometrical parameters. The frequency resolved signal obtained from 100 fs intense pulse excitation is shown in Fig. 24a at three incident pump amplitudes: $E_0 = 10^6$ V/m (green line), $E_0 = 10^7$ V/m (red line), and $E_0 = 10^8$ V/m (blue line). The pump frequency is 2 eV, corresponding to the plasmon mode for the period of 550 nm and wire's width $R_x = 520$ nm. The signal is normalized with respect to the pump intensity. The SH is clearly visible at all pump intensities, while TH signal can be seen only at 10^8 V/m.

To check the numerical convergence of the model and to ensure that peaks exhibited in Fig. 24a correspond to harmonics generation, SH and TH signals are integrated over frequencies to account for losses and dispersion and plotted as functions of the pump intensity in Fig. 24b. The slopes of both SH (black line) and TH (red line) are nearly ideal 2 and 3, respectively.

67
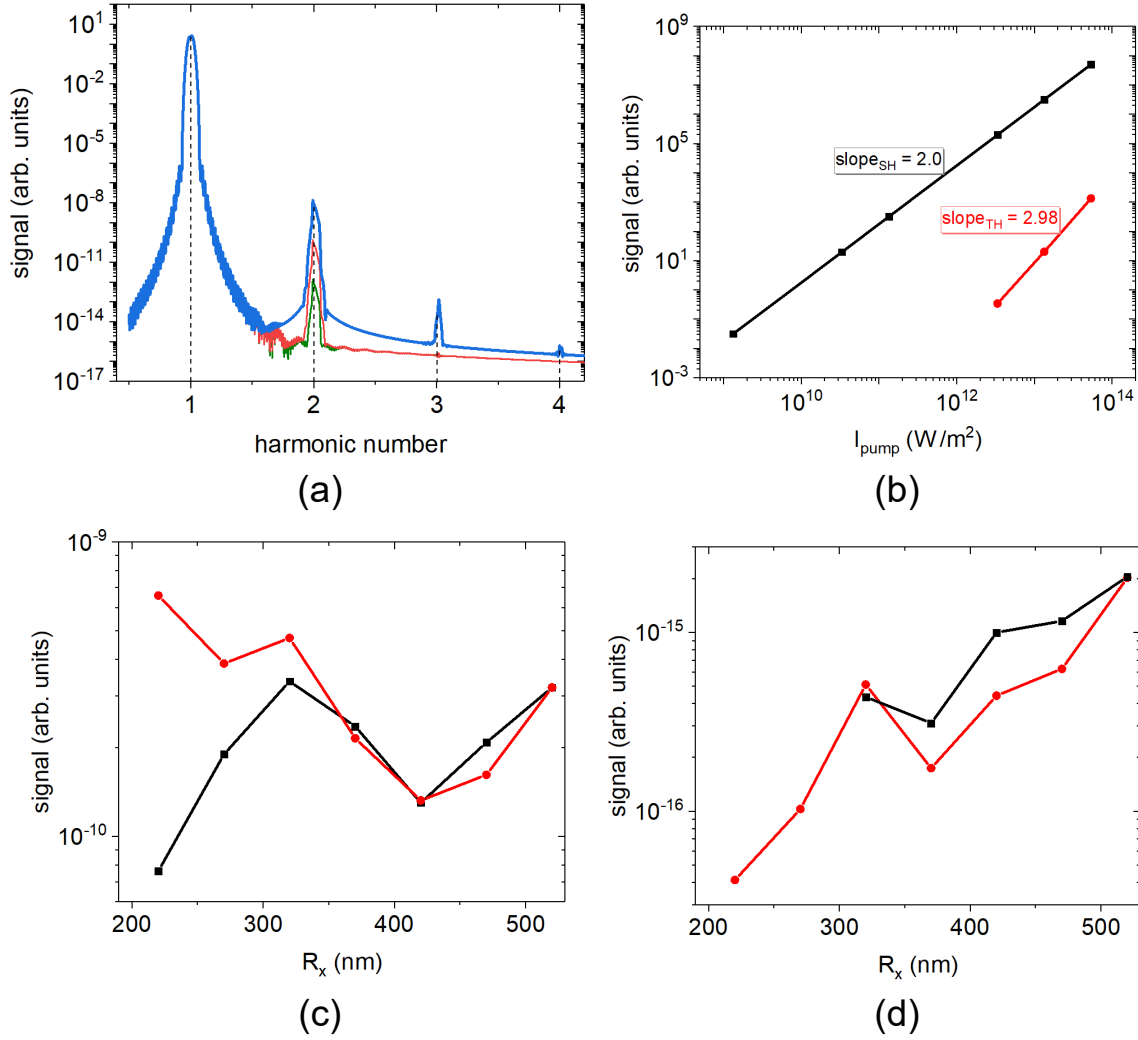
Figure 24. Nonlinear Optics of the Metal Nanostructure

Note: Harmonics spectra for different pump amplitudes (a); SH signal (black line) and TH signal (red line) as functions of the pump intensity (b); SH (c) and TH (d) signals when pumped at the fixed plasmon resonance (black line) and when pumped at the resonant frequency evaluated for each value of R_x (red line).

Next, the influence of structural parameters and the effect of the plasmon resonance on SH (Fig. 24c) and TH (Fig. 24d) signals is explored. Two scenarios are considered:

- When varying R_x, the pump frequency is fixed at 2 eV (black lines);

- When varying R_x, the pump frequency is adjusted to a given geometry (red lines).

It is expected that when pumped at the plasmon resonance, the efficiency of SH and TH generation would be prominently higher due to local electromagnetic field enhancement. However, the results suggest a more complex behavior of the SHG process. As seen from Fig. 24c, the SH signal exhibits two maxima for a fixed pump frequency:

1. The enhancement at R_x = 520 nm, as it corresponds to the resonant conditions;
2. The SH signal for R_x = 320 nm is observed almost as high as in case 1.

When comparing SH signals off (black) and on (red) resonance, both conditions result in nearly the same SH efficiency for values of R_x above 300 nm. The TH signal (Fig. 24d) depends on R_x, as one expects, with the signal nearly monotonically increasing with R_x.

5.1.2   Nonlinear Regime of the Strongly Coupled System

After exploring the high harmonic generation by the plasmonic system, a hybrid construct is considered, combining the plasmonic grating with a few-layer thin 2D material, placing the latter on the input side (see Fig. 23a).

In order to quantitatively explore the nonlinear optical response of such a system, the Lorentz model for the 2D material with parameters describing WS_2 is used. Fig. 25a shows linear reflection spectra of the hybrid system with WS_2 placed 15 nm above the grating for the periods of 530 nm (red line) and of 550 nm (blue line). The strong coupling regime between SPR mode supported by the grating and WS_2 is achieved for the period of 550 nm and R_x = 520 nm. The rest of Fig. 25 discusses the high harmonic generation by the hybrid system with WS_2 modeled as a dispersive material with an instantaneous Kerr nonlinearity. The complete model, which also includes the second-order susceptibility, is presented in Fig. 26. The goal of simulations shown in Fig. 25 is to understand how a dispersive material may affect even harmonics generation (solely produced by metal) in the strong coupling regime.
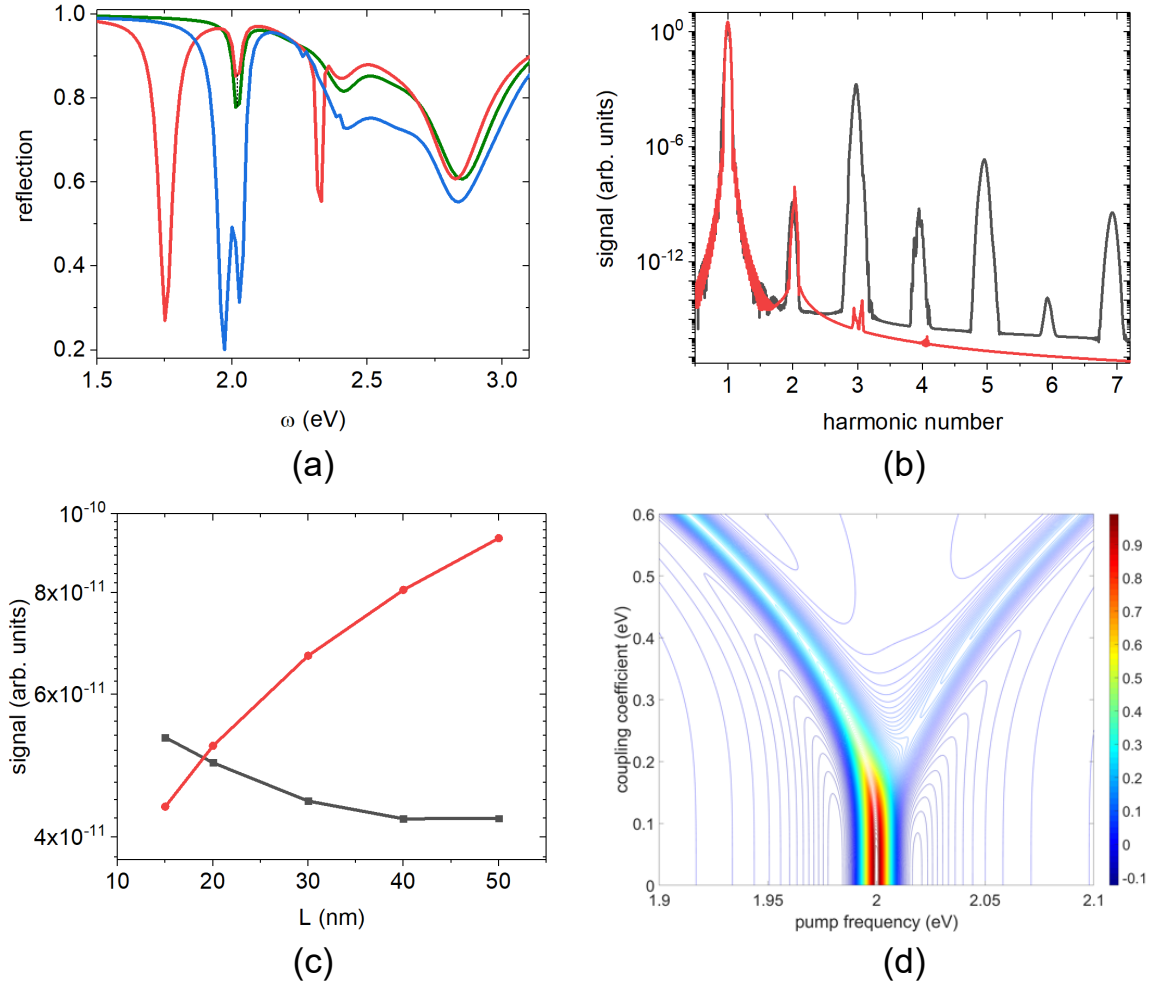
Figure 25. Nonlinear Optics of the Strongly Coupled System

Note: Linear reflection spectra for WS_2 (green line), for WS_2 placed above the grating for the periods of 530 nm (red line) and of 550 nm (blue line) (a); harmonics spectra with (black line) and without (red line) WS_2 (b); SH signal when pumped at 1.97 eV (black line) and at 2.03 eV (red line) (c); normalized real part of the second-order contribution $x_1^{(2)}$ (d).

Fig. 25b shows the harmonics spectra with (black line) and without (red line) WS_2 at the distance of 15 nm above the grating. The pump amplitude is $E_0 = 10^8$ V/m, the pump frequency is 1.97 eV, the period of the grating is 550 nm, and R_x is 520 nm. One can notice two important effects:

1. Odd harmonics are significantly enhanced by WS_2;

2. Even harmonics are greatly affected by the very presence of WS_2, even though the model does not directly include the second-order susceptibility for WS_2.

In order to further elucidate and understand this effect, a simple model of two coupled oscillators with one being externally driven and having a second-order nonlinearity is considered:

$$\ddot{x}_1 + \gamma_1 \dot{x}_1 + \omega_1^2 x_1 + a x_1^2 - g^2 x_2 = F_0,$$
$$\ddot{x}_2 + \gamma_2 \dot{x}_2 + \omega_2^2 x_2 - g^2 x_1 = 0,$$

$$(5.1)$$

where x_1, x_2 correspond to displacements of two oscillators that are coupled through the dipole-dipole coupling proportional to the parameter g^2, the first oscillator is driven by the external force F_0 and has a second-order nonlinearity characterized by the parameter a. To show the analogy with the hybrid system, one can note that the first oscillator represents metal and the second one is the 2D material. When the incident field is small, the second-order nonlinearity in the first equation is significantly smaller compared to other terms. One can apply the Rayleigh-Schrödinger perturbation theory (Boyd 2008) to find the second-order contribution for the process of the SHG:

$$x_1^{(2)} = -\frac{a F_0^2}{\omega_1^2 + i\gamma_1(2\omega) - (2\omega)^2} \left(\frac{\omega_2^2 + i\gamma_2\omega - \omega^2}{g^4 - \left(\omega_1^2 + i\gamma_1\omega - \omega^2\right)\left(\omega_2^2 + i\gamma_2\omega - \omega^2\right)} \right)^2. \quad (5.2)$$

Equation (5.2) shows that SH is significantly influenced by the presence of another dispersive material (even though this material does not have its own second-order nonlinearity), as long as the coupling is strong enough. The corresponding second-order susceptibility, associated with (5.2), peaks at two well-defined frequencies:

$$\omega_\pm^2 = \frac{\omega_1^2 + \omega_2^2}{2} \pm \sqrt{\frac{\left(\omega_1^2 - \omega_2^2\right)^2}{4} + g^4}, \quad (5.3)$$

corresponding to the upper and lower polaritonic states of two coupled oscillators (Novotny 2010).

71
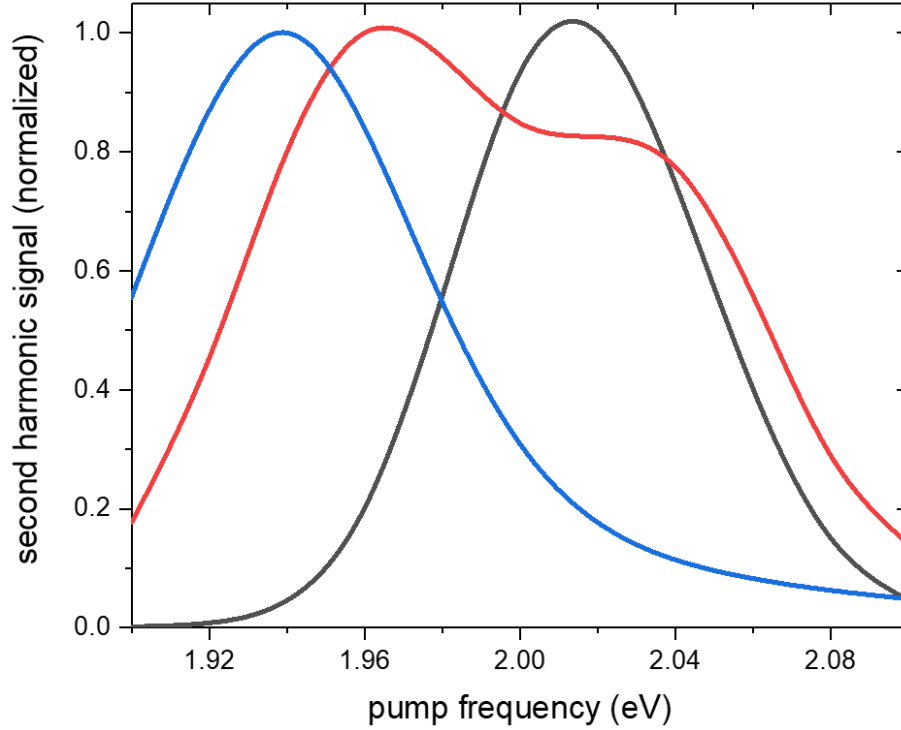
Figure 26. SH Signal for the Plasmonic Grating (black line), the Grating Coupled to 2D Material with Only the Third-Order Nonlinearity (red line), and with Both Second and Third Order Susceptibilities (blue line)

In the numerical model, the system is pumped using the frequency corresponding to either lower or upper polaritonic states. The SH signal for the lower polariton pump drops as a function of the distance L, while the pumping at the upper polariton leads to an increase of the SH signal with the distance between WS_2 and the metal. It can be noted that the SH signal is higher when WS_2 is absent (see Fig. 25b, red vs black lines for the SH).

Fig. 25c shows the SH signal as a function of the distance between the grating and WS_2, L, (see Fig. 24a) when pumped at the lower (black lines) and upper (red lines) polariton energies (1.97 eV and 2.03 eV), respectively. One may expect that both lines in Fig. 25c need to reach an asymptotic value at very large distances L. However, it does not happen in the simulations. It means that WS_2 is not directly coupled to the surface plasmons at large values of L, but it still

influences the electromagnetic field that is driving the plasmonic grating. Since WS_2 is located on the input side, it results in a filtering effect.

The analytical model can be used to explain the difference between different pumping frequencies for the SH signal seen in Fig. 25c. Fig. 25d shows the real part of the second-order contribution $x_1^{(2)}$ for the case when the eigenfrequencies of each oscillator are slightly displaced relative to one another. When the coupling strength increases (i.e., WS_2 is placed closer to the plasmonic array), the hybrid states are clearly visible. The SH signal is significantly non-symmetric, exhibiting higher values at the lower polaritonic brunch since two oscillators have both different damping parameters (as in the case of the real system, where the metal is significantly lossier than the exciton mode of WS_2) and different eigenfrequencies.

Since WS_2 is noncentrosymmetric, it also has a second-order susceptibility, $\chi^{(2)}$, which was shown experimentally to reach remarkably high values due to a large joint density of states (Janisch et al. 2014). Fig. 26 shows the SH signal as a function of the pump frequency, comparing three models:

- Periodic plasmonic grating only;
- Plasmonic grating with WS_2 taking into account only its $\chi^{(3)}$;
- Plasmonic grating coupled to WS_2 with both $\chi^{(2)}$ and $\chi^{(3)}$.

The bare metal generates the SH more efficiently if pumped at the corresponding plasmon frequency, as it was pointed out earlier. When the second-order nonlinearity of WS_2 is included in simulations, the maximum of the SH signal is red-shifted to 1.94 eV, which is not the exciton absorption peak of bare WS_2 (2.01 eV), but rather the lower polariton state of the coupled system. When $\chi^{(2)}$ is neglected, the SH signal has a signature of the strong coupling with two well-seen resonant peaks corresponding to the upper and lower polaritonic modes. It should be noted that the frequency shift observed in the calculations has been experimentally observed for a system comprised of c-Porphyrin and a metal cavity (Chervy et al. 2016).

73

To sum up, self-consistent calculations combining the nonlinear optical response of a periodic plasmonic system coupled to a thin nonlinear material exhibiting instantaneous second and third-order nonlinearities (with parameters corresponding to tungsten disulfide) are presented. It is demonstrated that under strong coupling conditions the SH signal solely generated by the metal is significantly influenced by the dispersion of WS_2, even when the second-order nonlinearity for WS_2 is neglected. A simple analytical model of two coupled oscillators is presented to explain this effect.

5.2 Plasmon Enhanced Second Harmonic Generation by Periodic Arrays of Triangular Nanoholes Strongly Coupled to Quantum Emitters

Optical properties of periodic arrays of nanoholes of a triangular shape with experimentally realizable parameters are discussed below. The electromagnetic radiation is described classically in accordance with Maxwell's equations (2.1). The optical response in spatial regions occupied by metal is considered using classical hydrodynamics describing conduction electrons (2.31). To study the strong coupling between plasmons and molecular assemblies and its consequences on SHG, rate equations that govern the dynamics of the macroscopic polarization in spatial regions with molecules are employed (2.50).

The resulting set of coupled equations (2.1), (2.25), and (2.50) constitutes the basis for considering molecules and plasmonic materials on equal footing and combining their response to external excitation in both linear and nonlinear regimes. In the simulations, the following parameters are used to describe silver: plasma frequency Ω_p = 8.28 eV, effective electron mass m^* = 0.99m_e, and phenomenological decay constant γ = 0.048 eV. In order to describe molecules, the transition frequency and number density are varied and other parameters are fixed: transition dipole μ_{eg} = 10 D, radiationless decay rate of the excited state Γ = 4.1 × 10^{-3} eV, and the pure

dephasing rate $\gamma^* = 5.9 \times 10^{-3}$ eV. The periodic arrays of triangular holes in a thin silver film are schematically depicted in the inset of Fig. 27a.
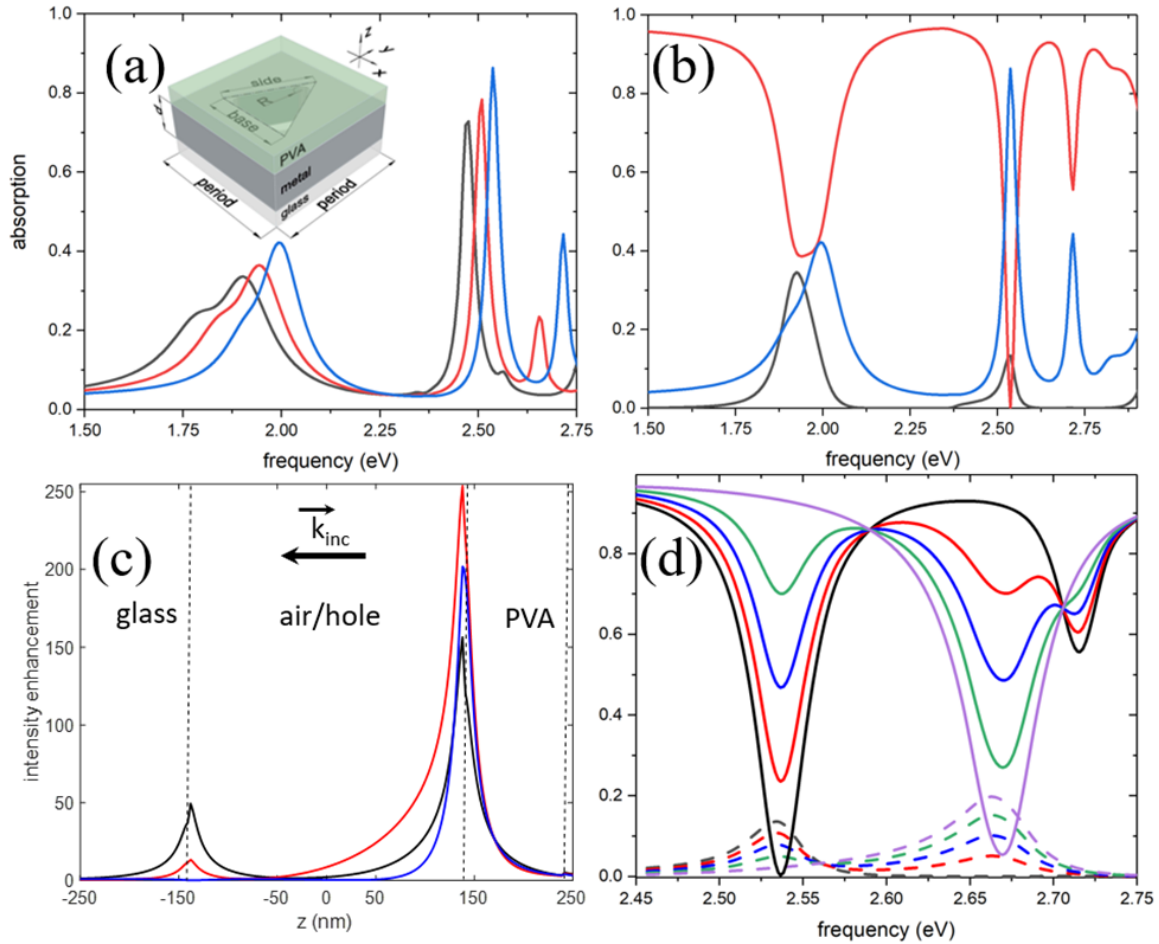
Figure 27. Linear Optics of Triangular Nanoholes

Note: Schematics of a unit cell and linear absorption for different values of R (a); linear transmission (black line), reflection (red line), and absorption (blue line) (b); intensity at different frequencies (c); linear transmission (dashed lines) and reflection (solid lines) at different incident field polarizations (d).

The SHG from circular holes is noticeably lower, compared to the one generated by non-symmetric holes (Barnes, Dereux, and Ebbesen 2003; Salomon, Wang, et al. 2013; Salomon, Zielinski, et al. 2013). 280 nm thick silver metal film is placed on a semi-infinite glass substrate with a refractive index of 1.5 and is covered by a 100 nm thick polyvinyl alcohol (PVA) layer with

the same refractive index (Segal, Haleva, and Salomon 2019). It is also assumed that the areas inside holes are not filled with any dielectric. The square arrays have a periodicity of 346.5 nm. The triangular holes have a side of 220 nm and a base of 200 nm. The system is excited by a plane wave at normal incidence emanating from the air side.

Fig. 27 summarizes the main results on linear optical response. First, the influence of sharp corners of holes on linear absorption is examined, as shown in Fig. 27a. The linear absorption as a function of frequency is presented for three values of the curvature R that define how sharp the corners of the hole are. There, the black line is for $R = 1$ nm, the red line is for $R = 10$ nm, and the blue line is for $R = 20$ nm. The incident field is x-polarized. One can notice a blue shift of all resonant modes. It can be explained by the decrease in the volume of the hole since the curvature R increases. Another feature one can observe is the mode near 1.75 eV, which appears for sharp corners and is hardly noticeable for $R = 20$ nm. The sharp edges lead to knee-type resonances (Sukharev and Seideman 2007; Sukharev et al. 2007). So the observed feature is due to the lightning rod effect. Additionally, the enhancement and blue shift of the high energy mode seen near 2.7 eV are observed.

The linear spectra (transmission, reflection, and absorption) are plotted in Fig. 27b for the incident field polarized along x-axis and $R = 20$ nm is fixed. Three resonant modes are seen at 1.99 eV, 2.54 eV, and 2.71 eV (values are extracted from the absorption spectrum). Two low frequency resonances are in both transmission and reflection spectra. That indicates the plasmonic character of those modes. One can note that the mode at 2.71 eV has nearly 0 transmission. The mode at 2.54 eV is associated with the substantial transmission, but the reflection reaches a very low value of 3×10^{-3}. Spatial distributions of the observed modes are examined to understand their physical nature. The in-plane intensity distributions exhibit complex spatial characters with the energy localized mainly in between the holes at 2.54 eV and 2.71 eV. The electromagnetic intensity calculated at 1.99 eV is predominantly localized at the edges of the holes and inside the

metal. The longitudinal dependence at three frequencies: 1.99 eV (black line), 2.54 eV (red line), and 2.71 eV (blue line) is shown in Fig. 27c. Here the steady-state intensities computed at resonant frequencies corresponding to maxima of the absorption (Fig. 27b) as functions of the longitudinal coordinate, z, are plotted. Two other coordinates are fixed at x = -55 nm and y = 0 nm (measuring from the center of the hole). The initial enhancement is observed for all three modes near the boundary between the PVA and the hole. They are exponentially decreasing when going through the hole to the substrate. Another enhancement is seen on the output side near the substrate.

For the square array of holes at normal incidence, the expression for the resonant wavelength of the Bragg plasmon can be used (Ghaemi et al. 1998):

$$\lambda_{SPP} = \frac{period}{\sqrt{i^2 + j^2}} \sqrt{\frac{\epsilon_{dielectric}\epsilon_{metal}}{\epsilon_{dielectric} + \epsilon_{metal}}}, \tag{5.4}$$

to give a rough estimate for the lowest diffraction order $(i, j) = (1, 0)$ resonant frequency. For the interface with glass/PVA, it is 2.1 eV. To explore this dependence, simulations are performed varying the incident polarization and tracking corresponding resonances, as shown in Fig. 27d. Firstly, the lowest frequency mode at 1.99 eV is merely affected. It exhibits small variations of the resonance shape and its frequency. That happens because of the non-symmetric shape of holes. The simulations are repeated for holes having an equilateral triangular shape. It is observed that the lowest frequency resonance is nearly independent of the incident polarization. Thus, the lowest frequency mode at 1.99 eV (x-polarization) is a Localized Surface Plasmon Resonance (LSPR) associated with the individual hole. Secondly, two other modes are noticeably dependent on the incident polarization (see Fig. 27d). There, linear transmission (dashed lines) and reflection (solid lines) are shown as functions of frequency calculated at different incident field polarizations defined by the angle between the electric field and x-axis: 0° (i.e., x-polarization; black), 30° (red), 45° (blue), 60° (green), 90° (i.e., y-polarization; magenta). Two plasmon resonances at 2.54 eV and 2.67 eV correspond to the first-order Bragg plasmons. They have different

frequencies since the shape of the holes is not symmetric. In summary, as seen in Fig. 27b, the x-polarized incident field leads to excitation of the LSPR mode (1.99 eV), the first-order Bragg plasmon (2.54 eV), and the mode localized inside PVA with no surface plasmon character (2.71 eV), which may be interpreted as a waveguide mode in the PVA layer.

5.2.1   Linear Regime of the Strongly Coupled System

Here the focus is on molecular emitters embedded in the PVA layer and how they interact with either of the three resonant modes discussed above.

Fig. 28 summarizes the results with molecules. The optical absorption calculated for the array without emitters (black) and with emitters resonant at the LSPR frequency of 1.99 eV with the molecular concentration of 2×10^{25} m^{-3} (red) and 4×10^{25} m^{-3} (blue) is shown at Fig. 28a. It is seen that the absorption significantly increases at the resonant frequency with increasing molecular concentration. One can observe the hybrid molecular-plasmon modes due to the strong coupling, which becomes more pronounceable at the molecular concentration of 4×10^{25} m^{-3}.

Fig. 28b shows absorption with molecules resonant at the first-order Bragg plasmon frequency of 2.54 eV and Fig. 28c shows absorption for the molecules resonant at the frequency of 2.71 eV (the corresponding resonant mode is localized inside the PVA layer). The color scheme is the same as in Fig. 28a. The Rabi splitting due to the molecule-plasmon hybridization is significantly higher when the molecules are resonant at 2.54 eV (Bragg plasmon) and 2.71 eV (waveguide mode), as seen in Figs. 28b and 28c, respectively. In both cases, the Rabi splitting reaches 135 meV at the molecular concentration of 4×10^{25} m^{-3}.

The polarization dependence of the absorption at the Bragg plasmon frequency is explored in Fig. 28d with the molecules resonant at 2.54 eV (Bragg mode). The dashed lines correspond
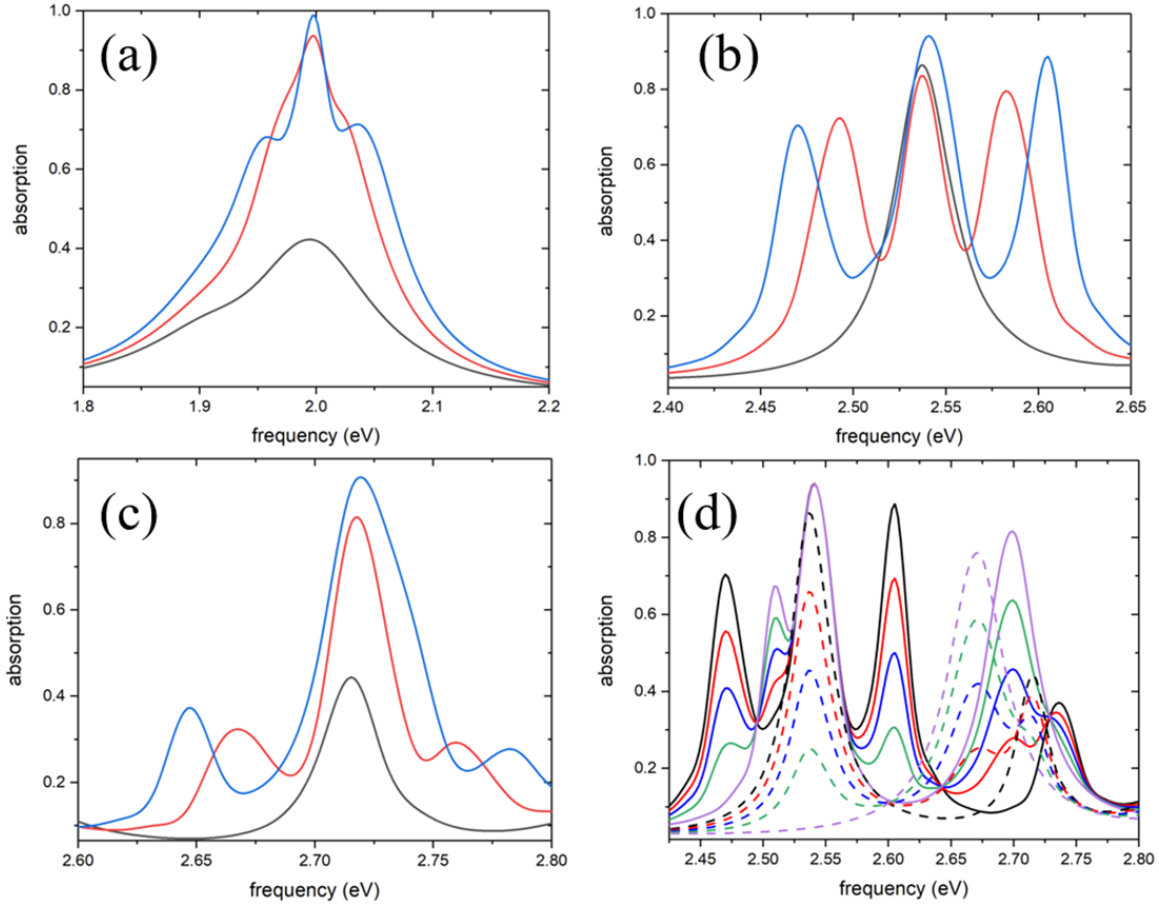
Figure 28. Linear Absorption of Triangular Nanohole Arrays with Two-Level Molecular Emitters

Note: Absorption of the array without emitters (black line) and with emitters resonant at 1.99 eV with the molecular concentration of 2×10^{25} m^{-3} (red line) and 4×10^{25} m^{-3} (blue line) (a); absorption with molecules resonant at 2.54 eV (b), at 2.71 eV (c), the color scheme is the same as at (a); absorption of the array without molecules (dashed lines) and with molecules (solid lines) for different incident field polarization (d).

to the array without molecules, the solid lines show the response of the array with molecules. Different incident field polarizations are defined by the angle between the electric field and x-axis: 0° (i.e., x-polarization; black), 30° (red), 45° (blue), 60° (green), 90° (i.e., y-polarization; magenta). The molecular density is 4×10^{25} m^{-3}. Here the in-plane polarization of the incident field is gradually changed, keeping molecules resonant at 2.54 eV. There are several features discussed

below. Firstly, the central absorption peak near 2.54 eV is blue-shifted for all polarizations if one compares it with the array without molecules. Secondly, there is no change in Rabi splitting for different polarization because the incident polarization does not change the molecular concentration. The absorption for upper/lower polariton modes becomes smaller with the incident polarization rotating from x to y direction since the first-order Bragg plasmon along x has lower frequency compared to its counterpart excited at y-polarization. Thirdly, one can observe the absorption peak at 2.51 eV which becomes more noticeable as the incident polarization turns more toward y. Both x- and y-Bragg plasmons are excited for 30°, 45°, and 60° polarizations. One can notice the polaritonic states associated with the strong coupling between molecules and x-Bragg plasmon. Also, the lower polariton state at 2.51 eV is due to the coupling with y-Bragg plasmon. Since the latter is far from the molecular resonance (2.54 eV), only a small portion of it is hybridized. The upper polariton part of this coupling is buried under the large absorption peak at 2.54 eV. The modes near 2.7 eV are shifted to higher frequencies compared to the case of the array without molecules as it was discussed above.

5.2.2 Nonlinear Regime of the Strongly Coupled System

Now triangular hole arrays response is examined if it is subjected to an intense resonant laser pulse excitation.

Fig. 29a shows the normalized power spectrum of the array without molecules. The transmitted and reflected energies are combined. The black line shows the complete model based on equation (2.31) with all terms included but pressure. The red line shows the results of simulations when the Coulomb term (the third term in (2.31)) and pressure are dropped. The blue line shows results when the convective term and pressure (the last term in (2.31)) are neglected. The excitation pulse has an amplitude of 10^7 V/m, is at the frequency of 1.99 eV, and is polarized
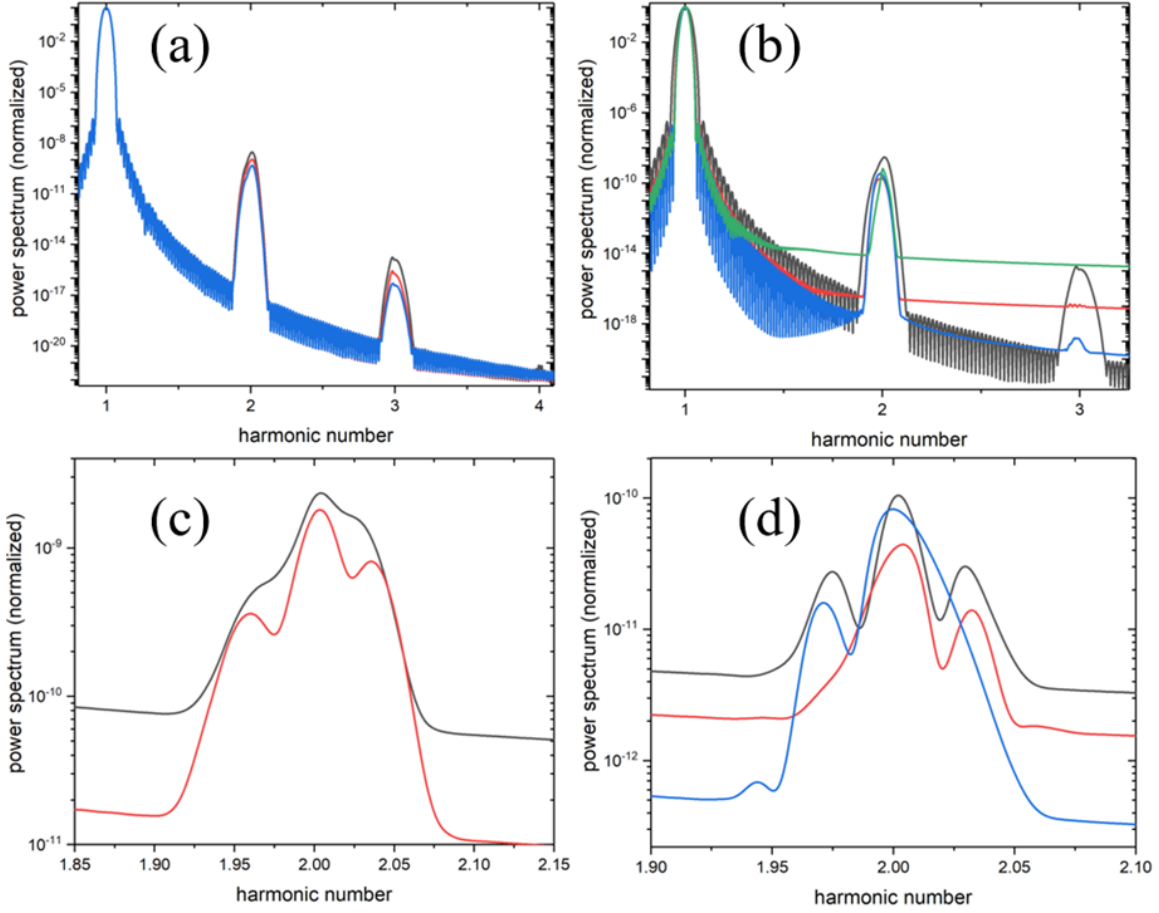
Figure 29. Nonlinear Response of Triangular Nanoholes without and with the Molecular Layer

Note: Power spectra of the array without molecules where all terms of equation (2.31) are included (black line), no Coulomb term and pressure (red line), no convective term and pressure (blue line) (a); power spectra without molecules for different pump frequencies (b); power spectra with molecules with different number densities (b); power spectra with molecules for different pump frequencies (d).

along x. Interesting to note that turning on and off the magnetic part of the Lorentz force, $\dot{\mathbf{P}} \times \mathbf{B}$, has no feasible effect on the spectrum. Contrary, the Coulomb term, $\mathbf{E}\left(\nabla \cdot \dot{\mathbf{P}}\right)$, and the convective term, $\left[\left(\nabla \cdot \dot{\mathbf{P}}\right)\dot{\mathbf{P}} + \left(\dot{\mathbf{P}}\nabla\right)\dot{\mathbf{P}}\right]$, have a noticeable impact on the signal for the SH and the third harmonic. The spectrum where only Lorentz term is kept is not plotted since it shows a small tincture of the SH only. One can conclude that the main contributors to the nonlinear response are terms with spatial derivatives. It is seen that the polarization is governed by the magnetic part

of the Lorentz force and the gradients that depend on the free electron susceptibility and local electric field at the fundamental frequency. As Fig. 28a demonstrates, the gradients play the leading role in nanoscale systems and thus geometry becomes the major contributing factor.

Fig. 29b compares power spectra obtained by pumping the plasmonic array at four different resonant frequencies: 1.99 eV (black line), 2.54 eV (red line), 2.67 eV (blue line; the pump is y-polarized), and 2.71 eV (green line). The pump amplitude is the same as in Fig. 29a. The intensities of the second and third harmonics are significantly enhanced when the array is pumped at the LSPR frequency (1.99 eV). Pumping at either x- or y-Bragg plasmon resonances (2.54 eV and 2.67 eV, correspondingly) also leads to the SHG, but the third harmonic is greatly suppressed. Interestingly, y-Bragg plasmon does show a clear signal at the third harmonic, while x-Bragg plasmon does not. When the array is pumped at the frequency of the guiding mode (2.71 eV), only the SH is observed, which is not surprising since the resonant mode is mainly localized inside the PVA layer with a very small local field enhancement near the metal interface.

Figs. 29c and 29d explore the SHG by triangular hole arrays with molecules uniformly distributed inside the PVA layer. Fig. 29c shows the power spectrum near the SH of the pump. The spectrum is calculated for the array with molecules uniformly distributed inside the PVA layer. The black line shows results for the number density of molecules of 2×10^{25} m^{-3} and the red line is for the density of 4×10^{25} m^{-3}. The molecular transition frequency is set at 1.99 eV. The incident pump is resonant at 1.99 eV, has the amplitude of 10^7 V/m, and is polarized along x. Fig. 29d shows results of simulations similar to that in Fig. 29c but for three different pump frequencies: the black line is for the pump at 2.54 eV (the first-order Bragg plasmon), the red line is for the pump at 2.49 eV (lower polariton), and the blue line is for the pump at 2.58 eV (upper polariton). The pump amplitude and the polarization are the same as in Fig. 29c. Molecular concentration is 2×10^{25} m^{-3}. The molecular transition frequency is 2.54 eV. A simple two-level model for molecular emitters (2.50) is considered, which supports only odd harmonic generation due to

the dipole selection rule. When molecules are not strongly coupled to any resonant modes of the array, the even harmonic generation is solely due to metal. However, when the system enters the strong coupling regime, there are significant changes to the lineshape of the SH, as seen in Fig. 29c. Here the system is pumped at the LSPR frequency with the molecules being resonant to that as well. A tincture of the SH signals produced by the exciton-plasmon states at the concentration of 2×10^{25} m^{-3} is seen in Fig. 29c (black line). When the molecular concentration is increased, three peaks are clearly visible. These correspond to the SH of the lower polariton, the LSRP mode, and the upper polariton. When pumped at 2.54 eV, one can observe three peaks in the SH signals. Two different scenarios are considered. First, if pumped at the frequency of the lower polariton (Fig. 29d, red line), its SH is noticeably enhanced and the SH of the Bragg plasmon is seen as well. Secondly, when the system is driven at the upper polariton frequency in addition to its SH and the corresponding plasmon peak, one can see a small contribution from the lower polariton as well.

5.2.3   Polarization Dependence of the Second Harmonic Generation

Horizontally and vertically polarized SH signals were separately calculated in order to explore angular dependence and the physical nature of the SHG enhanced by the LSPR mode. The measurement of those is performed in the far field zone along a circular detection contour (see the red line at Fig. 30a). The red dashed circle with a radius of 100 nm is placed 588 nm above the PVA layer. It consists of 36 detection points equally spread along the circle with an angular displacement of 10°.

Fig. 30b shows calculated angular diagrams: horizontally, $|E_x(2\omega)|^2$, (black line) and vertically, $|E_y(2\omega)|^2$, (red line) polarized SH signals for the triangular hole arrays without molecules detected along the contour shown in Fig. 30a. The pump pulse has an amplitude of 10^7 V/m
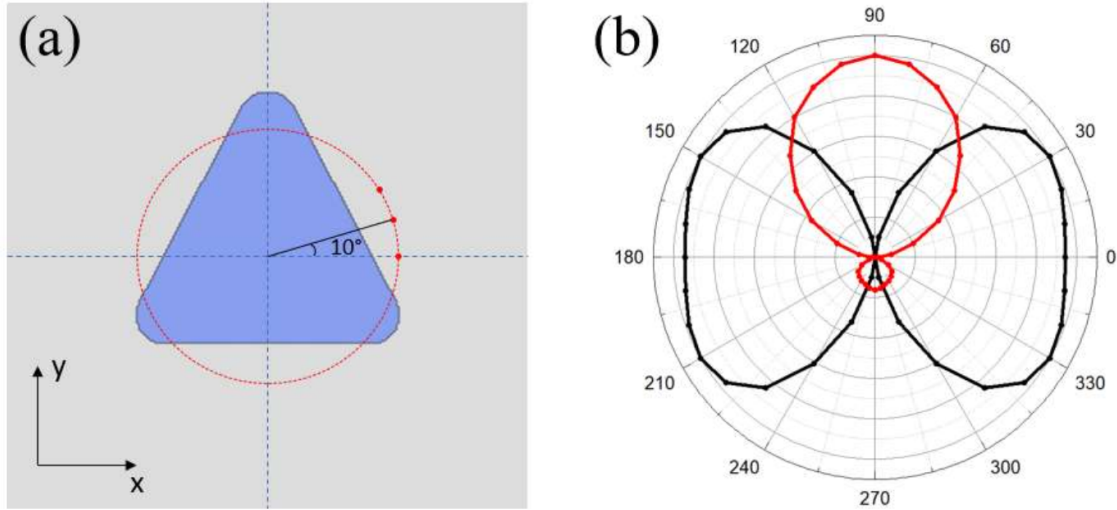
Figure 30. Polarization Dependence of SH of Triangular Nanoholes

Note: Top view of the unit cells of the simulation domain with red detection points indicated (a); $|E_x(2\omega)|^2$ (black line) and $|E_y(2\omega)|^2$ (red line) (b).

with a duration of 100 fs, and is polarized along x. The pump frequency is 1.99 eV. One can note that the horizontally polarized SH signal is left-right symmetric due to the mirror symmetry of the triangular shape. Also, the vertical polarization exhibits highly enhanced directional radiation in the direction of the upper corner of the triangular hole. That indicates that the hole acts as a directional nonlinear antenna.

To conclude, linear and nonlinear responses of periodic arrays of nanoholes of a triangular shape using experimentally realizable parameters were investigated. It is shown how the arrays with and without molecules optically respond when driven by intense resonant laser pulses.

Chapter 6

CONCLUSIONS

The presented thesis summarizes the results of the following publications: (Drobnyh, Pachter, and Sukharev 2019; Drobnyh and Sukharev 2020; Maekawa et al. 2020; Minh Ngo et al. 2022; Sukharev, Drobnyh, and Pachter 2022). The combination of numerical electrodynamics methods and the nonlinear hydrodynamic Drude model for conduction electrons in metals served as a very powerful tool that was utilized to study nonlinear responses generated at plasmonic interfaces.

Generation of the second harmonic radiation was investigated, quantitatively and qualitatively, in periodic arrays of nanoprisms, nanocrescents, and nanodolmens. In particular, the great sensitivity of the second harmonic to the shapes of the nanoparticles, their surface roughness, and incident field polarization was confirmed for all the nanostructures mentioned above. To characterize the second harmonic quantitatively, the values of second-order susceptibility are reported for nanodolmens as a function of the pump frequency. Moreover, the values of hyperpolarizability were extracted from the numerical modeling and then were compared and found in consistent agreement with experimental results.

Exploration of nonlinear plasmonic materials strongly coupled to quantum systems was done in two and three dimensions. It was shown that under the strong coupling condition, the second harmonic signal solely generated by the periodic plasmonic system was significantly influenced by the 2D few-layer material even when the second-order nonlinearity of this 2D material is neglected. In the 3D case, when the plasmonic interface is strongly coupled to molecules, the second harmonic lineshapes were shown to be substantially modified exhibiting three peaks that correspond to the second harmonic signals at a driving frequency and upper and lower polari-

tons. The numerical results were supported by a simple analytical model of a driven anharmonic oscillator coupled to a Lorentz oscillator via dipole-dipole coupling.

To summarize, second harmonic responses from a variety of metal nanostructures have been vigorously investigated in this thesis. The strong coupling regime is discussed, and a theoretical model is applied to explain the numerical findings. A possible extension of this work could be an exploration of higher orders harmonics in exciton-plasmon systems and their interaction with quantum emitters under strong coupling conditions.

REFERENCES

Agranovich, V. M. 2012. *Surface Polaritons.* Elsevier, December 2, 2012. Google Books: wKJpV 8c2ZtQC.

Alagiri, Mani, Perumal Rameshkumar, and Alagarsamy Pandikumar. 2017. "Gold Nanorod-Based Electrochemical Sensing of Small Biomolecules: A Review." *Microchimica Acta* 184, no. 9 (September 1, 2017): 3069–3092. https://doi.org/10.1007/s00604-017-2418-6.

Autere, Anton, Henri Jussila, Yunyun Dai, Yadong Wang, Harri Lipsanen, and Zhipei Sun. 2018. "Nonlinear Optics with 2D Layered Materials." *Advanced Materials* 30 (24): 1705963. https://doi.org/10.1002/adma.201705963.

Balanis, Constantine A. 2012. *Advanced Engineering Electromagnetics, 2nd Edition.* Wiley Global Education, January 10, 2012. Google Books: 2eMbAAAAQBAJ.

Barnes, William L., Alain Dereux, and Thomas W. Ebbesen. 2003. "Surface Plasmon Subwavelength Optics." *Nature* 424, no. 6950 (6950): 824–830. https://doi.org/10.1038/nature01937.

Bengali, Sadiq, and Manish Giri (Hewlett Packard Development Co LP). 2018. Gold sensor. U.S. patent 20180229236A1, filed August 16, 2018. https://patents.google.com/patent/US20180229236A1/en.

Berenger, Jean-Pierre. 1994. "A Perfectly Matched Layer for the Absorption of Electromagnetic Waves." *Journal of Computational Physics* 114, no. 2 (October 1, 1994): 185–200. https://doi.org/10.1006/jcph.1994.1159.

Black, Charles T., Stephen M. Gates, Christopher B. Murray, and Shouheng Sun (International Business Machines Corp). 2000. Magnetic storage medium formed of nanoparticles. U.S. patent 6162532A, filed December 19, 2000. https://patents.google.com/patent/US6162532A/en.

Bohren, Craig F., and Donald R. Huffman. 1983. *Absorption and Scattering of Light by Small Particles.* Wiley, April 15, 1983. Google Books: R5IpAQAAMAAJ.

Boyd, Robert W. 2008. *Nonlinear Optics.* Elsevier, May 13, 2008. Google Books: uoRUi1Yb7ooC.

Bukasov, Rostislav, and Jennifer S. Shumaker-Parry. 2007. "Highly Tunable Infrared Extinction Properties of Gold Nanocrescents." *Nano Letters* 7, no. 5 (May 1, 2007): 1113–1118. https://doi.org/10.1021/nl062317o.

Chervy, Thibault, Jialiang Xu, Yulong Duan, Chunliang Wang, Loïc Mager, Maurice Frerejean, Joris A. W. Münninghoff, et al. 2016. "High-Efficiency Second-Harmonic Generation from Hybrid Light-Matter States." *Nano Letters* 16, no. 12 (December 14, 2016): 7352–7356. https://doi.org/10.1021/acs.nanolett.6b02567.

Cooper, Cindy T., Miguel Rodriguez, Steve Blair, and Jennifer S. Shumaker-Parry. 2014. "Polarization Anisotropy of Multiple Localized Plasmon Resonance Modes in Noble Metal Nanocrescents." *The Journal of Physical Chemistry C* 118, no. 2 (January 16, 2014): 1167–1173. https://doi.org/10.1021/jp4107876.

Courant, R., K. Friedrichs, and H. Lewy. 1967. "On the Partial Difference Equations of Mathematical Physics." *IBM Journal of Research and Development* 11, no. 2 (March): 215–234. https://doi.org/10.1147/rd.112.0215.

Dressel, Martin, George Gruner, and George Grüner. 2002. *Electrodynamics of Solids: Optical Properties of Electrons in Matter.* Cambridge University Press, January 17, 2002. Google Books: mUXTz65FvHQC.

Drobnyh, Elena, Ruth Pachter, and Maxim Sukharev. 2019. "Harmonic Generation by Metal Nanostructures Optically Coupled to Two-Dimensional Transition-Metal Dichalcogenide." *The Journal of Physical Chemistry C* 123, no. 11 (March 21, 2019): 6898–6904. https://doi.org/10.1021/acs.jpcc.9b00257.

Drobnyh, Elena, and Maxim Sukharev. 2020. "Plasmon Enhanced Second Harmonic Generation by Periodic Arrays of Triangular Nanoholes Coupled to Quantum Emitters." *The Journal of Chemical Physics* 152, no. 9 (March 7, 2020): 094706. https://doi.org/10.1063/1.5143238.

Franken, P. A., A. E. Hill, C. W. Peters, and G. Weinreich. 1961. "Generation of Optical Harmonics." *Physical Review Letters* 7, no. 4 (August 15, 1961): 118–119. https://doi.org/10.1103/PhysRevLett.7.118.

Gallinet, Benjamin, and Olivier J. F. Martin. 2011. "Relation between near–Field and Far–Field Properties of Plasmonic Fano Resonances." *Optics Express* 19, no. 22 (October 24, 2011): 22167–22175. https://doi.org/10.1364/OE.19.022167.

Ghaemi, H. F., Tineke Thio, D. E. Grupp, T. W. Ebbesen, and H. J. Lezec. 1998. "Surface Plasmons Enhance Optical Transmission through Subwavelength Holes." *Physical Review B* 58, no. 11 (September 15, 1998): 6779–6782. https://doi.org/10.1103/PhysRevB.58.6779.

Goy, P., J. M. Raimond, M. Gross, and S. Haroche. 1983. "Observation of Cavity-Enhanced Single-Atom Spontaneous Emission." *Physical Review Letters* 50, no. 24 (June 13, 1983): 1903–1906. https://doi.org/10.1103/PhysRevLett.50.1903.

Greiner, Walter. 2012. *Classical Electrodynamics.* Springer Science & Business Media, December 6, 2012. Google Books: acjcBwAAQBAJ.

Griffiths, David J. 2017. *Introduction to Electrodynamics.* Cambridge University Press, June 29, 2017. Google Books: Kh4xDwAAQBAJ.

Haroche, Serge, and Daniel Kleppner. 1989. "Cavity Quantum Electrodynamics." *Physics Today* 42, no. 1 (January): 24–30. https://doi.org/10.1063/1.881201.

Harrington, Roger F. 1961. *Time-Harmonic Electromagnetic Fields.* McGraw-Hill. Google Books: FtpPAAAAMAAJ.

Hümmer, T., F. J. García-Vidal, L. Martín-Moreno, and D. Zueco. 2013. "Weak and Strong Coupling Regimes in Plasmonic QED." *Physical Review B* 87, no. 11 (March 15, 2013): 115419. https://doi.org/10.1103/PhysRevB.87.115419.

Jackson, John David. 2012. *Classical Electrodynamics.* Wiley. Google Books: 8qHCZjJHRUgC.

Jain, Prashant K., Xiaohua Huang, Ivan H. El-Sayed, and Mostafa A. El-Sayed. 2008. "Noble Metals on the Nanoscale: Optical and Photothermal Properties and Some Applications in Imaging, Sensing, Biology, and Medicine." *Accounts of Chemical Research* 41, no. 12 (December 16, 2008): 1578–1586. https://doi.org/10.1021/ar7002804.

Jain, Prashant K., Ivan H. El-Sayed, and Mostafa A. El-Sayed. 2007. "Au Nanoparticles Target Cancer." *Nano Today* 2, no. 1 (February 1, 2007): 18–29. https://doi.org/10.1016/S1748-0132(07)70016-6.

Janisch, Corey, Yuanxi Wang, Ding Ma, Nikhil Mehta, Ana Laura Elías, Néstor Perea-López, Mauricio Terrones, Vincent Crespi, and Zhiwen Liu. 2014. "Extraordinary Second Harmonic Generation in Tungsten Disulfide Monolayers." *Scientific Reports* 4, no. 1 (1 2014): 5530. https://doi.org/10.1038/srep05530.

Kaluzny, Y., P. Goy, M. Gross, J. M. Raimond, and S. Haroche. 1983. "Observation of Self-Induced Rabi Oscillations in Two-Level Atoms Excited Inside a Resonant Cavity: The Ringing Regime of Superradiance." *Physical Review Letters* 51, no. 13 (September 26, 1983): 1175–1178. https://doi.org/10.1103/PhysRevLett.51.1175.

Kittel, Charles. 1956. *Introduction to Solid State Physics.* Wiley. Google Books: jv5QAAAAMAAJ.

Kreibig, Uwe, and Michael Vollmer. 1995. *Optical Properties of Metal Clusters.* Springer, May 30, 1995. Google Books: jYhRAAAAMAAJ.

Lancaster, Cady A., and Jennifer S. Shumaker-Parry. 2016. "Surface Preparation of Gold Nanostructures on Glass by Ultraviolet Ozone and Oxygen Plasma for Thermal Atomic Layer Deposition of Al2O3." *Thin Solid Films* 612 (August 1, 2016): 141–146. https://doi.org/10.1016/j.tsf.2016.05.043.

Landau, L. D., and E. M. Lifshitz. 1982. *Mechanics: Volume 1.* Elsevier, January 29, 1982.

Lee, Kyeong-Seok, and Mostafa A. El-Sayed. 2006. "Gold and Silver Nanoparticles in Sensing and Imaging: Sensitivity of Plasmon Response to Size, Shape, and Metal Composition." *The Journal of Physical Chemistry B* 110, no. 39 (October 1, 2006): 19220–19225. https://doi.org/10.1021/jp062536y.

Maekawa, Hiroaki, Elena Drobnyh, Cady A. Lancaster, Nicolas Large, George C. Schatz, Jennifer S. Shumaker-Parry, Maxim Sukharev, and Nien-Hui Ge. 2020. "Wavelength and Polarization Dependence of Second-Harmonic Responses from Gold Nanocrescent Arrays." *The Journal of Physical Chemistry C* 124, no. 37 (September 17, 2020): 20424–20435. https://doi.org/10.1021/acs.jpcc.0c05548.

Maier, Stefan Alexander. 2007. *Plasmonics: Fundamentals and Applications.* Springer Science & Business Media, May 16, 2007. Google Books: yT2ux7TmDc8C.

Mansuripur, M., A. R. Zakharian, A. Lesuffleur, Sang-Hyun Oh, R. J. Jones, N. C. Lindquist, Hyungsoon Im, A. Kobyakov, and J. V. Moloney. 2009. "Plasmonic Nano-Structures for Optical Data Storage." *Optics Express* 17, no. 16 (August 3, 2009): 14001–14014. https://doi.org/10.1364/OE.17.014001.

Martin-Moreno, Luis. 2009. "Detecting Unseen Light." *Nature Physics* 5, no. 7 (7): 457–458. https://doi.org/10.1038/nphys1314.

Medici, Serenella, Massimiliano Peana, Valeria Marina Nurchi, Joanna I. Lachowicz, Guido Crisponi, and Maria Antonietta Zoroddu. 2015. "Noble Metals in Medicine: Latest Advances." *Coordination Chemistry Reviews* 284 (February 1, 2015): 329–350. https://doi.org/10.1016/j.ccr.2014.08.002.

Minh Ngo, Hoang, Elena Drobnyh, Maxim Sukharev, Quoc Khuong Vo, Joseph Zyss, and Isabelle Ledoux-Rak. 2022. "High Yield Synthesis and Quadratic Nonlinearities of Gold Nanoprisms in Solution: The Role of Corner Sharpness." *Israel Journal of Chemistry,* e202200009. https://doi.org/10.1002/ijch.202200009.

Naik, Gururaj V., Bivas Saha, Jing Liu, Sammy M. Saber, Eric A. Stach, Joseph M. K. Irudayaraj, Timothy D. Sands, Vladimir M. Shalaev, and Alexandra Boltasseva. 2014. "Epitaxial Superlattices with Titanium Nitride as a Plasmonic Component for Optical Hyperbolic Metamaterials." *Proceedings of the National Academy of Sciences of the United States of America*

111, no. 21 (May 27, 2014): 7546–7551. https://doi.org/10.1073/pnas.1319446111. pmid: 24821762.

Novotny, Lukas. 2010. "Strong Coupling, Energy Splitting, and Level Crossings: A Classical Perspective." *American Journal of Physics* 78, no. 11 (November): 1199–1202. https://doi.org/10.1119/1.3471177.

Pacheco, Peter. 1997. *Parallel Programming with MPI.* Morgan Kaufmann. Google Books: GufgfWSHt28C.

Palik, Edward D. 1998. *Handbook of Optical Constants of Solids.* Academic Press. Google Books: nxoqxyoHfbIC.

Pines, David. 1956. "Collective Energy Losses in Solids." *Reviews of Modern Physics* 28, no. 3 (July 1, 1956): 184–198. https://doi.org/10.1103/RevModPhys.28.184.

Powell, C. J., and J. B. Swan. 1959. "Origin of the Characteristic Electron Energy Losses in Aluminum." *Physical Review* 115, no. 4 (August 15, 1959): 869–875. https://doi.org/10.1103/PhysRev.115.869.

Raether, Heinz. 1988. *Surface Plasmons on Smooth and Rough Surfaces and on Gratings.* Springer-Verlag. Google Books: ZLwrAAAAYAAJ.

Rakić, Aleksandar D., Aleksandra B. Djurišić, Jovan M. Elazar, and Marian L. Majewski. 1998. "Optical Properties of Metallic Films for Vertical-Cavity Optoelectronic Devices." *Applied Optics* 37, no. 22 (August 1, 1998): 5271–5283. https://doi.org/10.1364/AO.37.005271.

Rempe, Gerhard, Herbert Walther, and Norbert Klein. 1987. "Observation of Quantum Collapse and Revival in a One-Atom Maser." *Physical Review Letters* 58, no. 4 (January 26, 1987): 353–356. https://doi.org/10.1103/PhysRevLett.58.353.

Ritchie, R. H. 1957. "Plasma Losses by Fast Electrons in Thin Films." *Physical Review* 106, no. 5 (June 1, 1957): 874–881. https://doi.org/10.1103/PhysRev.106.874.

Rodrigues, M. S., D. Costa, R. P. Domingues, M. Apreutesei, P. Pedrosa, N. Martin, V. M. Correlo, et al. 2018. "Optimization of Nanocomposite Au/TiO2 Thin Films towards LSPR Optical-Sensing." *Applied Surface Science,* 10th International Conference on Materials Science & Engineering, 438 (April 30, 2018): 74–83. https://doi.org/10.1016/j.apsusc.2017.09.162.

Salomon, Adi, Yehiam Prior, Michael Fedoruk, Jochen Feldmann, Radoslaw Kolkowski, and Joseph Zyss. 2014. "Plasmonic Coupling between Metallic Nanocavities." *Journal of Optics* 16, no. 11 (November): 114012. https://doi.org/10.1088/2040-8978/16/11/114012.

Salomon, Adi, Shaojun Wang, James A. Hutchison, Cyriaque Genet, and Thomas W. Ebbesen. 2013. "Strong Light-Molecule Coupling on Plasmonic Arrays of Different Symmetry." *ChemPhysChem* 14 (9): 1882–1886. https://doi.org/10.1002/cphc.201200914.

Salomon, Adi, Marcin Zielinski, Radoslaw Kolkowski, Joseph Zyss, and Yehiam Prior. 2013. "Size and Shape Resonances in Second Harmonic Generation from Silver Nanocavities." *The Journal of Physical Chemistry C* 117, no. 43 (October 31, 2013): 22377–22382. https://doi.org/10.1021/jp403010q.

Sarychev, Andrey K., and Vladimir M. Shalaev. 2007. *Electrodynamics of Metamaterials*. World Scientific. Google Books: JE1qDQAAQBAJ.

Sato, Isamu, Taro Oike, and Naoki Hanashima (TDK Corp). 2009. Heat assisted magnetic recording head and heat assisted magnetic recording apparatus for heating a recording region in a magnetic recording medium during magnetic recording. U.S. patent 7538978B2, filed May 26, 2009. https://patents.google.com/patent/US7538978B2/en.

Scalora, M., M. A. Vincenti, D. de Ceglia, V. Roppo, M. Centini, N. Akozbek, and M. J. Bloemer. 2010. "Second- and Third-Harmonic Generation in Metal-Based Structures." *Physical Review A* 82, no. 4 (October 18, 2010): 043828. https://doi.org/10.1103/PhysRevA.82.043828.

Segal, Elad, Emir Haleva, and Adi Salomon. 2019. "Ultrasensitive Plasmonic Sensor for Detecting Sub-PPB Levels of Alachlor." *ACS Applied Nano Materials* 2, no. 3 (March 22, 2019): 1285–1293. https://doi.org/10.1021/acsanm.8b02164.

Shuford, Kevin L., Mark A. Ratner, and George C. Schatz. 2005. "Multipolar Excitation in Triangular Nanoprisms." *The Journal of Chemical Physics* 123, no. 11 (September 15, 2005): 114713. https://doi.org/10.1063/1.2046633.

Shumaker-Parry, J. S., H. Rochholz, and M. Kreiter. 2005. "Fabrication of Crescent-Shaped Optical Antennas." *Advanced Materials* 17 (17): 2131–2134. https://doi.org/10.1002/adma.200500063.

Sipe, J. E., V. C. Y. So, M. Fukui, and G. I. Stegeman. 1980. "Analysis of Second-Harmonic Generation at Metal Surfaces." *Physical Review B* 21, no. 10 (May 15, 1980): 4389–4402. https://doi.org/10.1103/PhysRevB.21.4389.

Stratton, Julius Adams. 2007. *Electromagnetic Theory*. John Wiley & Sons, January 22, 2007. Google Books: zFeWdS2luE4C.

Sukharev, Maxim, Elena Drobnyh, and Ruth Pachter. 2022. "Fano Plasmonics Goes Nonlinear." *The Journal of Chemical Physics* 157, no. 13 (October 7, 2022): 134105. https://doi.org/10.1063/5.0109872.

Sukharev, Maxim, and Abraham Nitzan. 2017. "Optics of Exciton-Plasmon Nanomaterials." *Journal of Physics. Condensed Matter: An Institute of Physics Journal* 29, no. 44 (November 8, 2017): 443003. https://doi.org/10.1088/1361-648X/aa85ef. pmid: 28805193.

Sukharev, Maxim, and Tamar Seideman. 2007. "Coherent Control of Light Propagation via Nanoparticle Arrays." *Journal of Physics B: Atomic, Molecular and Optical Physics* 40, no. 11 (May): S283–S298. https://doi.org/10.1088/0953-4075/40/11/S04.

Sukharev, Maxim, Jiha Sung, Kenneth G. Spears, and Tamar Seideman. 2007. "Optical Properties of Metal Nanoparticles with No Center of Inversion Symmetry: Observation of Volume Plasmons." *Physical Review B* 76, no. 18 (November 13, 2007): 184302. https://doi.org/10.1103/PhysRevB.76.184302.

Taflove, Allen. 1998. *Advances in Computational Electrodynamics: The Finite-difference Time-domain Method.* Artech House. Google Books: Ht0eAQAAIAAJ.

Taflove, Allen, Ardavan Oskooi, and Steven G. Johnson. 2013. *Advances in FDTD Computational Electrodynamics: Photonics and Nanotechnology.* Artech House. Google Books: ynRM33xslM8C.

Taliercio, Thierry, and Paolo Biagioni. 2019. "Semiconductor Infrared Plasmonics." *Nanophotonics* 8, no. 6 (June 1, 2019): 949–990. https://doi.org/10.1515/nanoph-2019-0077.

Tempel, David G., and Alán Aspuru-Guzik. 2011. "Relaxation and Dephasing in Open Quantum Systems Time-Dependent Density Functional Theory: Properties of Exact Functionals from an Exactly-Solvable Model System." *Chemical Physics,* Open Problems and New Solutions in Time Dependent Density Functional Theory, 391, no. 1 (November 24, 2011): 130–142. https://doi.org/10.1016/j.chemphys.2011.03.014.

Thompson, R. J., G. Rempe, and H. J. Kimble. 1992. "Observation of Normal-Mode Splitting for an Atom in an Optical Cavity." *Physical Review Letters* 68, no. 8 (February 24, 1992): 1132–1135. https://doi.org/10.1103/PhysRevLett.68.1132.

Törmä, P., and W. L. Barnes. 2015. "Strong Coupling between Surface Plasmon Polaritons and Emitters: A Review." *Reports on Progress in Physics. Physical Society (Great Britain)* 78, no. 1 (January): 013901. https://doi.org/10.1088/0034-4885/78/1/013901. pmid: 25536670.

Tran, Stephanie, Peter-Joseph DeGiovanni, Brandon Piel, and Prakash Rai. 2017. "Cancer Nanomedicine: A Review of Recent Success in Drug Delivery." *Clinical and Translational*

Medicine 6, no. 1 (December 11, 2017): 44. https://doi.org/10.1186/s40169-017-0175-0. pmid: 29230567.

Valev, V. K., N. Smisdom, A. V. Silhanek, B. De Clercq, W. Gillijns, M. Ameloot, V. V. Moshchalkov, and T. Verbiest. 2009. "Plasmonic Ratchet Wheels: Switching Circular Dichroism by Arranging Chiral Nanostructures." *Nano Letters* 9, no. 11 (November): 3945–3948. https://doi.org/10.1021/nl9021623. pmid: 19863052.

Yamamoto, N., K. Araya, and F. J. García de Abajo. 2001. "Photon Emission from Silver Particles Induced by a High-Energy Electron Beam." *Physical Review B* 64, no. 20 (November 6, 2001): 205419. https://doi.org/10.1103/PhysRevB.64.205419.

Yee, Kane. 1966. "Numerical Solution of Initial Boundary Value Problems Involving Maxwell's Equations in Isotropic Media." *IEEE Transactions on Antennas and Propagation* 14, no. 3 (May): 302–307. https://doi.org/10.1109/TAP.1966.1138693.

Zdanowicz, Mariusz, Sami Kujala, Hannu Husu, and Martti Kauranen. 2011. "Effective Medium Multipolar Tensor Analysis of Second-Harmonic Generation from Metal Nanoparticles." *New Journal of Physics* 13, no. 2 (February): 023025. https://doi.org/10.1088/1367-2630/13/2/023025.

Zhang, Xiaoying. 2015. "Gold Nanoparticles: Recent Advances in the Biomedical Applications." *Cell Biochemistry and Biophysics* 72, no. 3 (July): 771–775. https://doi.org/10.1007/s12013-015-0529-4. pmid: 25663504.

Zou, Jie, Kaizhong Gao, William Albert Challener, Mark Henry Ostrowski, Venkateswara Rao Inturi, Tong Zhao, and Michael Christopher Kautzky (Seagate Technology LLC). 2012. Recording head for heat assisted magnetic recording with diffusion barrier surrounding a near field transducer. U.S. patent 8339740B2, filed December 25, 2012. https://patents.google.com/patent/US8339740B2/en.